2016

Biodegradable Hybrid Tissue Engineering Scaffolds For Reconstruction Of Large Bone Defects

Danial Barati
University of South Carolina

BIODEGRADABLE HYBRID TISSUE ENGINEERING SCAFFOLDS FOR RECONSTRUCTION OF LARGE BONE DEFECTS

By

Danial Barati

Bachelor of Chemical Engineering

University of Tehran, 2009

Master of Science

University of South Carolina, 2013

Submitted in Partial Fulfillment of the Requirements

For the Degree of Doctor of Philosophy in

Chemical Engineering

College of Engineering and Computing

University of South Carolina

2016

Accepted by:

Esmaiel Jabbari , Major Professor

Francis Gadala-Maria, Committee Member

John Lavigne, Committee Member

Michael Gower, Committee Member

John W. Weidner, Committee Member

Lacy Ford, Senior Vice Provost and Dean of Graduate Studies

DEDICATION

I dedicate my dissertation work to my family and many friends. A special feeling of gratitude to my loving parents, and specifically my mom whose words of encouragement and push for tenacity ring in my ears. My sister Elham and my uncle Dr. Behravesh have never left my side and are very special.

ACKNOWLEDGEMENTS

I would like to be deeply grateful to my adviser, Prof. Esmaiel Jabbari for giving me the chance of working in his group and supporting me for 6 years to complete my Master's and Ph.D. programs in university of South Carolina. Also, I thank all my lab members (Dr. Moeinzadeh, Dr. He, Dr. Mercado, Dr. Karimi, Dr. Shariati, Safaa, Nazli, Leily and Samaneh) and undergraduate researchers who help me to complete my projects. I am strongly thankful to all of my friends in US and specifically Iranian friends who never left me alone during these years. Most importantly, none of this would have been possible without the love and patience of my family. My immediate family to whom this dissertation is dedicated to, has been a constant source of love, concern, support and strength all these years. I would like to express my heart-felt gratitude to my family. My extended family has aided and encouraged me throughout this endeavor.

ABSTRACT

Complex skeletal injuries and large bone fractures are still a significant clinical problem in US. Approximately 1.5 million Americans (veterans, their families, and civilians) every year suffer from bone loss due to traumatic skeletal injuries, infection, and resection of primary tumors that require extensive grafting to bridge the gap. The US bone graft market is over $2.2 billion a year. Due to insufficient mechanical stability, lack of vascularity, and inadequate resorption of the graft, patients with traumatic large skeletal injuries undergo multiple costly operations followed by extensive recovery steps to maintain proper bone alignment and length. Current strategies for repairing damaged or diseased bones include autologous or allograft bone transplantations. However, limited availability of autografts and risk of disease transmission associated with allografts have necessitated the search for the development of new bone graft options and strategies.

The overall goal of this project is to develop a much-needed bone-mimetic engineered graft as a substitute for current strategies providing required bone grafts for reconstruction of large bone defects. This project will use the structure of natural cortical bone as a guide to produce an engineered bone graft with balanced strength, osteogenesis, vascularization, and resorption. The outcome of this project will be a biodegradable hybrid scaffold system (similar to natural cortical bone) including a mechanically strong scaffold allowing for mechanical stability of the load-bearing defect site and a soft and highly porous structure such as a hydrogel phase which will allow for efficient cell and

growth factor delivery into the defect implantation site, cell niche establishment and promotion of mineralization. Successful completion of this project will transform bone graft technology for regeneration of complex bone defects from a frozen or freeze-dried allograft to a safe, infection-free, mechanically-stable, osteoinductive, and vasculogenic graft that is ultimately displaced by the patient's own tissue.

TABLE OF CONTENTS

LIST OF TABLES

LIST OF FIGURES

LIST OF ABBREVIATIONS

BMP……...…… Bone Morphogenic Protein

CaP……..Calcium Phosphate

ECFC…… …...Endothelial Colony Forming Cell

ECM…….....…….Extra Cellular Matrix

FGF……Fibroblast Growth Factor

GLU…….Glutamic acid

hMSC……...…….. human Mesenchymal Stem Cell

NF……..Nanofiber

NG……...…….Nanogel

SBF……...……..Simulated Body Fluid

VEGF…….. Vascular Endothelial Growth Factor

CHAPTER 1: BACKGROUND INFORMATION

1. General introduction

Repair and restoration of damaged bone is a major clinical challenge as well as an economic burden. Current strategies for repairing damaged or diseased bones include autologous or allograft bone transplantations. However, limited availability of autografts and risk of disease transmission associated with allografts have necessitated the search for the development of new bone graft options and strategies [1]. Tissue engineering has recently emerged as an alternative strategy for bone defect repair and regeneration. In this strategy, a biodegradable scaffold is often utilized along with osteogenic cells and/or bone inducing factors to mimic the natural structure of the tissue.

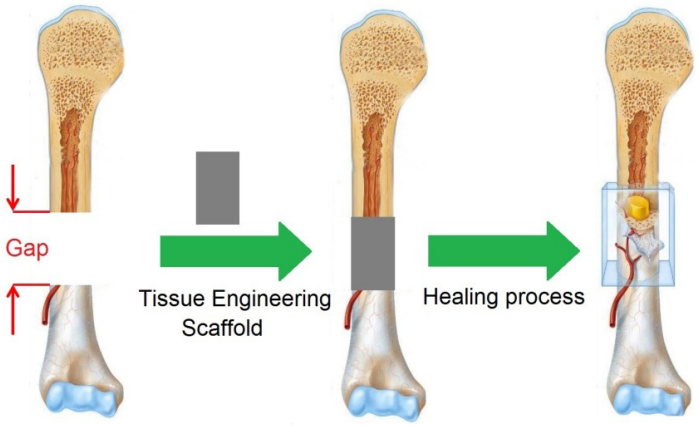

Figure 1.1: Tissue engineering approach for reconstruction of large bone fractures

Bone tissue is composed of an external layer, referred to as cortical or compact bone, and an internal layer, referred to as cancellous or spongy bone [2]. Cortical bone makes up to ~80% of the total bone mass in adults. It is extremely dense, with low porosity (20%) and high mechanical strength (130-190 MPa). Cancellous (spongy) bone accounts for the other 20% of the total bone mass and is highly porous (50%–90%), to allow for better penetration of vasculature, with ~10% of the mechanical strength of cortical bone [3]. Although cortical and cancellous layers are quite different in structure, they both contain a highly vascularized network. The presence of a vascular network is essential to supply nutrients and remove waste products. The main source of blood cells and vascular structures in bone is bone marrow [4]. Bone marrow is a soft, gelatinous and highly vascularized connective tissue within bone cavities and the spaces between the trabeculae of spongy bone. Bone marrow is either red or yellow, depending upon the preponderance of hematopoietic (red) or fatty (yellow) tissue [5].

A scaffold for bone regeneration should satisfy basic scaffold requirements such as biocompatibility, interconnected pore structure for tissue in-growth, and controlled degradation with physiologically-friendly degradation products [6, 7]. In addition, an ideal bone tissue engineering graft should provide suitable weight-bearing mechanical properties and have both excellent proosteogenesis and proangiogenesis to rapidly realize the bone regeneration *in vivo* [8, 9].

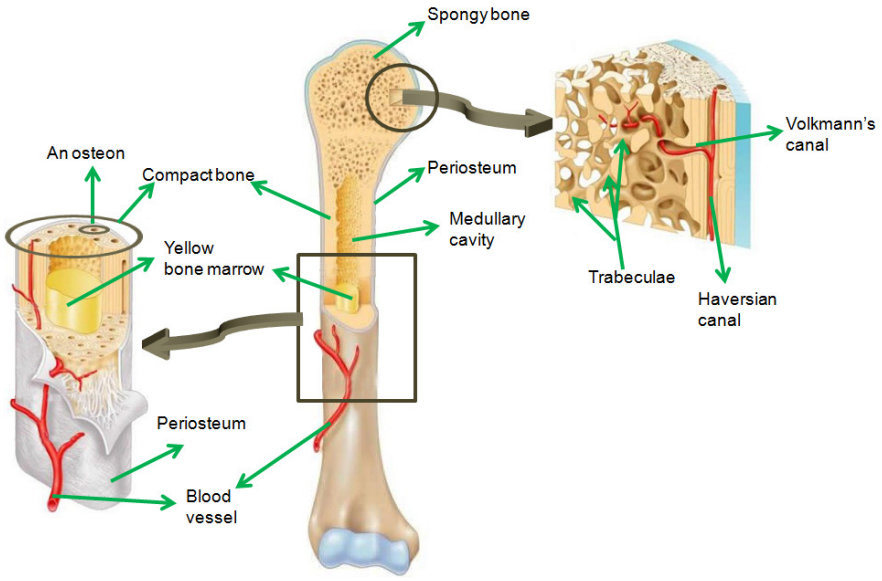

Figure 1.2. Bone anatomy (Copyright [a] 2004 Pearson Education, Inc., publishing as Benjamin Cummings).

In fact, the healing of bone defect is a complex, coordinated temporal process involving a myriad of molecular, cellular, biochemical and mechanical cues, among which angiogenesis, or neovascularization, is a critical factor for regenerative bone tissue, because the existence of a functional vascular network within the defect site can provide sufficient oxygen and nutrients to facilitate growth, differentiation, and tissue functionality, which is of particular importance for bone regeneration [10]. Thereupon, a desirable scaffold which could provide high mechanical stability and promote angiogenesis as well as osteogenesis during the bone regeneration process is worthy of study.

Although great strides have been made, it is difficult for any biomaterial to satisfy all of the listed requirements. To develop better scaffolds for bone regeneration, researchers

have attempted to integrate mechanically strong and porous scaffolds with soft and hydrated scaffolds such as hydrogels. These structures are referred to as hybrid scaffolds [11, 12]. In this approach, the mechanically strong scaffold component would allow for mechanical stability of the load-bearing defect site; whereas, the hydrogel phase will allow for efficient cell delivery into the defect implantation site, cell niche establishment and promotion of mineralization. Hydrogels are polymeric, soft and flexible networks that have the ability to absorb and retain a large volume of water (80%–99%) without dissolving [13]. Hydrogels can be made from natural biodegradable polymers such collagen, chitosan, and gelatin, or synthetic polymers such as polyethylene glycol (PEG) and polyvinyl alcohol [14, 15]. Their remarkable properties, including similarities with the ECM, proper biological performance, hydrophilicity, high permeability to oxygen and nutrients, and inherent cellular interaction capabilities, make them leading candidates for engineered tissue scaffolds [13]. Also, growth factors for the promotion of accelerated bone and vascularization (i.e., BMP, VEGF) may also be covalently tethered to the hydrogel phase to allow for enhanced effects upon implantation. For instance, non-degradable hybrid scaffolds were fabricated by loading a self-assembling peptide into a porous titanium or polyetheretherketone cage to study bone regeneration *in vitro* and *in vivo* [11, 12]. The observed bone regeneration was superior to hybrid grafts since the hydrogel phase offered a native environment for bone forming cells while the porous matrix mechanically supported bone regeneration [12]. In addition, hybrid grafts offer the possibility of osteogenic cell and factor encapsulation. The newly developed "polymer-hydrogel" hybrid system is robust: it not only satisfies mechanical needs but also has the ability to load the cells and factors required for osteogenesis and vasculogenesis [16].

Therefore, there is a clear need to develop biodegradable hybrid scaffold systems for effective bone tissue engineering.

Shortly, the overall aim of the present study is to develop a biodegradable hybrid scaffold system (similar to natural cortical bone shown in figure 1.2) that is weight bearing and osteoinductive for effective bone regeneration (Figure 1.3). We will address the most critical challenges separately to design an optimized hybrid structure with the final goal of improving the bone healing process.

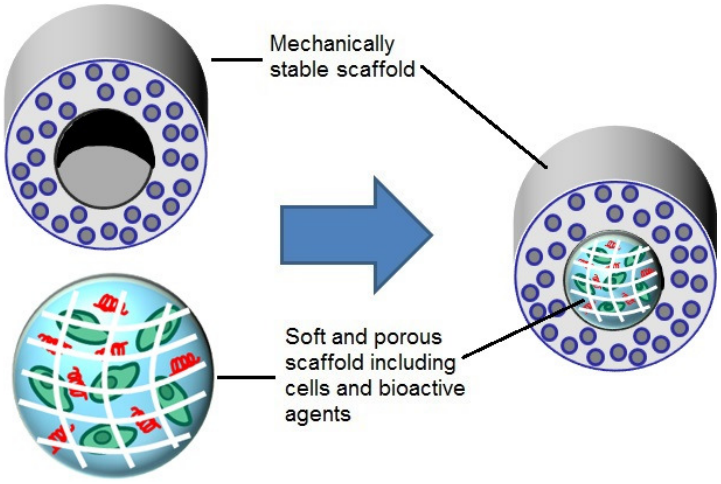

Figure 1.3. Engineered cortical bone-mimetic scaffold

The first major challenge in designing scaffolds for reconstruction of large bone defects is the graft's mechanical stability and toughness. The engineered graft should be sufficiently rigid for closure of the skeletal gap to maintain homeostasis [17]. Further, the engineered graft should be osteo-conductive/inductive and ultimately be replaced by the natural bone. The second major challenge in reconstruction of large bone defects is insufficient vascularization. Current tissue engineering strategies are extremely limited by

the lack of vascularization, leading to poor graft integration and failure of engineered substitutes in clinical trials [17]. Since diffusion of nutrients and oxygen to the progenitor cells in the graft is limited to a few hundred micrometers, successful regeneration of large bone defects requires early induction of vascularization in the graft [18, 19]. It is notable that the final effective bone regeneration and vessel formation in a critical sized defect are also attributed to the close association and interaction between angiogenesis and osteogenesis [20]. One hand, most osteogenic factors such as Bone Morphogenetic Protein-2 (BMP2) involved in osteogenesis stimulate angiogenesis, if not directly, then indirectly, through production of angiogenic molecules, such as Vascular Endothelial Growth Factor (VEGF) [16, 21]. For example, it has been clarified that during endochondral ossification, there is close correlation between vascularization and bone formation as the maximum extent of bone formation follows maximum levels of VEGF expression [22]. Therefore, the engineered graft should provide a compliant permissive environment such as a hydrogel phase which allows for efficient cell delivery into the defect implantation site, cell niche establishment and promotion of vascularization and osteogenesis [23]. The third challenge is timed-release of growth factors in their respective microenvironments. Interactions between cells play an important role in directing their function and differentiation. In vivo cellular communication is mainly through a cascade of chemical cues, such as protein interactions and growth factor signaling. Growth factors are known to affect cellular proliferation, migration, and differentiation during bone repair [24]. Owing to the critical role of growth factors in controlling basic cellular functions, and their ability to directly elicit and arrange tissue regeneration, a wide range of growth factors has been tested for distinct therapeutic applications, including bone regeneration and

neovascularization of ischaemic tissues. For instance, bone morphogenetic protein-2 (BMP-2), transforming growth factor-β (TGF-β), fibroblast growth factor (FGF), platelet-derived growth factor (PDGF), insulin-like growth factor (IGF), endothelin-1, and vascular endothelial growth factor (VEGF) are involved in bone formation [25]. BMP, PDGF, FGF, and VEGF have been shown to enhance migration of osteoprogenitor cells, while TGF-β, IGFs, and BMPs modulate their proliferation and differentiation [26]. Additionally, VEGF and FGF are involved in initiating vascular growth during bone healing [25]. The cross-talk between osteoblasts and endothelial cells (ECs) is conducted through the release of VEGF by osteoblasts, which act on ECs to promote angiogenesis, and through the release of BMPs by ECs, which act on precursor bone cells to promote osteoblastic differentiation. In addition, FGF has been shown to stimulate proliferation and migration of ECs [27] and also induce osteoblasts differentiation[28]. Therefore, one efficient way to obtain osteoinductivity and enhance repair of the critical sized bone defects is application of growth factors such as of BMP2 and VEGF as it has been largely reported [29]. However, concerns about these bioactive strategies still remain, such as the uncontrollable dose and composition of the delivered growth factors, and a high degradation rate resulting from a high *in vivo* instability of the angiogenic factors [30]. Currently, for the clinical therapy, BMP-2 in a high dosage thereafter a high cost need to be used, which is possibly accompanied by the contingent risk and side effect, such as excessive bone resorption and promotion of tumor angiogenesis [31, 32]. Furthermore, it has been shown that the extent of bone formation *in vivo* depends on the duration of exposure of osteoprogenitor cells and endothelial progenitor cells to BMP2 and VEGF,

respectively [33-35]. Therefore, the controlled delivery system of growth factors becomes increasingly necessary and important.

To address these challenges, the idea is to utilize novel nanomaterials to mimic the shell-core structure of cortical bone which is composed of interconnected network of microcanals, and a compliant, permissive core with timed and localized release of BMP2 and VEGF to form an osteoblastic-vascular niche (Figure 1.3). In nano scale, bone has a nanocomposite structure made of collagen type I nanofibers (~ 30 wt%) and hydroxyapatite nanocrystals (~ 70 wt%) . The superior mechanical stability and osteoinductivity of cortical bone in the natural tissue stem from the presence of high amount of hydroxylapatite nanocrystals on the surface of collagen nanofibers (Figure 1.4a). Therefore, to address the first challenge, aligned polylactide (PLA) nanofibers with a tunable degradation time were mineralized with high quantity of calcium phosphate (CaP) nanocrystals by incubation in simulated body fluid (SBF) supplemented with bone-derived organic acids (Ami 1, Figure 1.4b).

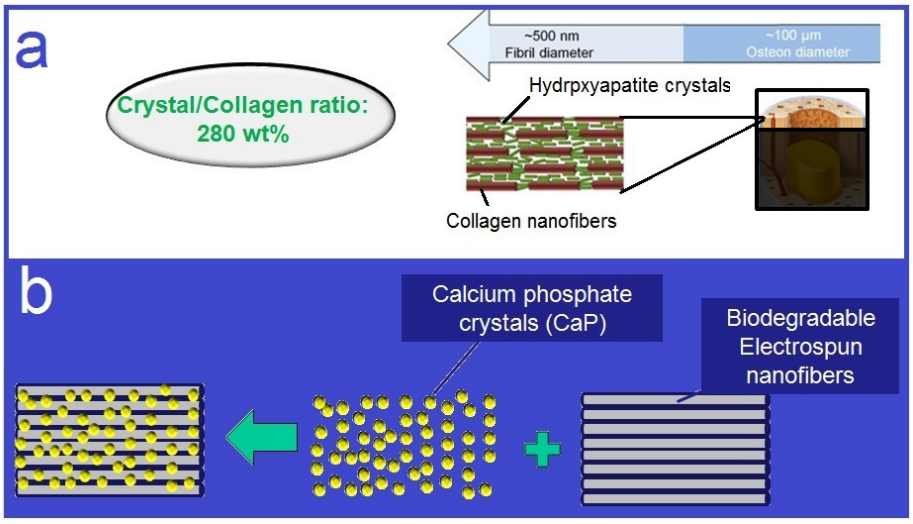

Figure 1.4. a) Aim 1: Nanostrucuture of natural cortical bone. b) Engineering approach to mimic the nanostructure of cortical bone

Then, the CaP-nucleated nanofiber microsheets will be wrapped into microtubes and a set of microtubes will be assembled around a cylindrical mold and allowed to fuse by annealing above the glass transition temperature (Tg) of PLA nanofibers to form a rigid, tough, osteoconductive, cylindrical shell.

As it was mentioned earlier, the main source of blood cells and vascular structures in bone is a soft, gelatinous and highly porous structure called bone marrow which is placed in the core of cortical bone and empty spaces in cancellous bone. Hence, to address the second challenge, a compliant hydrogel loaded with required cells and growth factors will be designed to form a osteoblastic-vascular niche in the structure of the engineered scaffold.

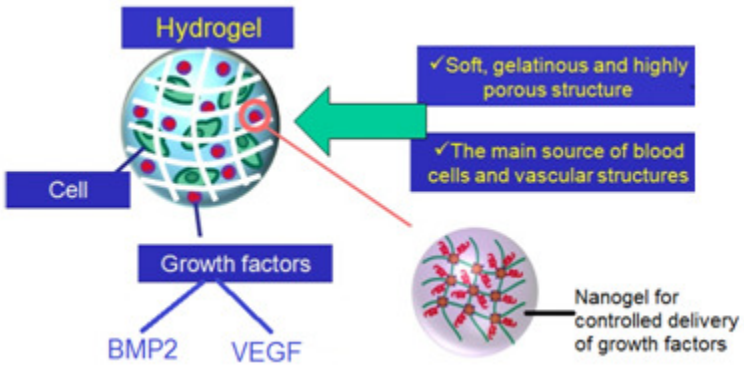

Figure 1.5. Aim 2 and 3: Compliant hydrogel loaded with required cells and growth factors to mimic soft structure of bone marrow

It should be also emphasized that osteogenesis and vascularization processes are coupled during the bone formation and regeneration as maximum extent of osteogenesis follows maximum level of vascularization and vice-versa. Therefore, in this work, a patterned hydrogel were designed to facilitate controlling both osteogenesis and vasculogenesis processes in the scaffold and consequently increase the extent of bone

formation. Moreover, to address the third challenge, a set of nanogels (NGs) were engineered to control the release rate of growth factors in patterned hydrogel. To do this, polyethylene glycol (PEG) chain-extended with short lactide (L) and glycolide (G) segments were used to form self-assembled NGs and facilitate a wide range of timed-release for different types of growth factors such as BMP2 and VEGF.

Accordingly, the following aims are considered to test the hypothesis toward the objectives.

Aim 1. To engineer a cortical-bone-mimetic nanostructured shell by fabricating mineralized nanofibers and evaluate with respect to mechanical strength. osteoconductivity, and degradability.

Ami 2. To synthesize resorbable, self-assembled, polyethylene glycol based nanogels and evaluate with respect to size, degardation rate and the release kinetics of BMP2- and VEGE-grafted nanogels.

Ami 3. To evaluate the extent of vasculogenesis and osteogenesis of human mesenchymal stem cells (hMSCs) and human colony-forming endothelial cells (ECFCs) encapsulated in a patterned hydrogel with spatiotemporal release of BMP2 and VEGF.

CHAPTER 2: FABRICATION AND CHARACTERIZATION OF MINERALIZED NANOFIBERS USING SIMULATED BODY FLUID SUPPLEMENTED WITH BONE-DERIVED ORGANIC ACID [1]

1. Introduction

Reconstruction of large incomplete bone segments remains a significant clinical problem [36, 37]. Frozen allogeneic bone graft is used but the long-term failure rate of allografts in reconstruction of large segmental defects mainly due to infection and non-union is 25%.[37, 38] Demineralized bone matrix provides a supportive matrix for differentiation and maturation of osteoprogenitor cells but it fails to provide rigidity for segmental defects.[39] Ceramics and polymers and their composites have been used to generate constructs matrices for regeneration of load-bearing bone defects.[40] In particular, calcium phosphate (CaP) ceramics have attracted much attention as a bone substitute due to their osteoconductivity and osteointegrative properties[41, 42] but they are brittle in tension and shear.[43, 44]

[1] Barati, D., et al., Effect of Organic Acids on Calcium Phosphate Nucleation and Osteogenic Differentiation of Human Mesenchymal Stem Cells on Peptide Functionalized Nanofibers. Langmuir, 2015. 31(18): p. 5130-5140.

Fiber-reinforced composites composed of calcium phosphates and degradable polymers can potentially have superior properties than their individual components but their properties are limited by the amount of CaP crystals that can be incorporated in the composite matrix.[45-49] There is a need for composite biomaterials that can stabilize the regenerating volume, have tunable resorption, and support differentiation and maturation of osteoprogenitor cells.

Mineralization in bone is mediated by extracellular matrix (ECM) proteins rich in glutamic acid sequence.[50, 51] In previous studies, we demonstrated that CaP contents as high as 200% (based on fiber weight) can be achieved on nanofiber microsheets by combining surface functionalization of the nanofibers with glutamic acid peptides and using a layer-by-layer CaP deposition approach to overcome the limited penetration of calcium and phosphate ions in the microsheets. The CaP content achieved in our previous study was higher than that of cancellous bone (190%)[52] but lower than the compact bone (>250%).[10] Carboxylate-rich organic acids account for 5.5% of the organic matter in bone and citric acid plays a significant role in controlling crystallite size, growth and the extent of mineralization in the natural bone.[53] Recently, it was reported that the spacing between the carboxylate groups in citric acid matches the spacing between calcium ions in the growing CaP nanocrystals.[53-57] Citrate ions in the CaP nucleation solution inhibit the formation of large and stable crystals in solution[58] and catalyze CaP nucleation on surfaces.[59]

The objectives of this work was to investigate the effect of supplementing the nucleation medium with organic acids on the extent of CaP nucleation on the surface of

functionalized nanofiber microsheets and osteogenic differentiation of human mesenchymal stem cells (hMSCs) seeded on the surface of functionalized nanofiber microsheets through the following approach. The CaP nucleating peptide Glu-Glu-Gly-Gly-Cys (EEGGC) was conjugated to relatively low molecular weight poly(DL-lactide) to produce a LMPLA-GLU conjugate. LMPLA-GLU conjugate was mixed with high molecular weight PLA and electrospun to generate aligned GLU-functionalized PLA nanofiber microsheets. The microsheets were incubated in concentrated simulated body fluid (SBF) supplemented with an organic acid to nucleate and grow CaP crystals on the surface of nanofibers. Citric acid (CA), hydroxycitric acid (HCA), tartaric acid (TART), malic acid (MA), salicylic acid (SalA) and ascorbic acid (AsA) were selected to tested organic acids with a range of carboxylic acid and hydroxyl groups.

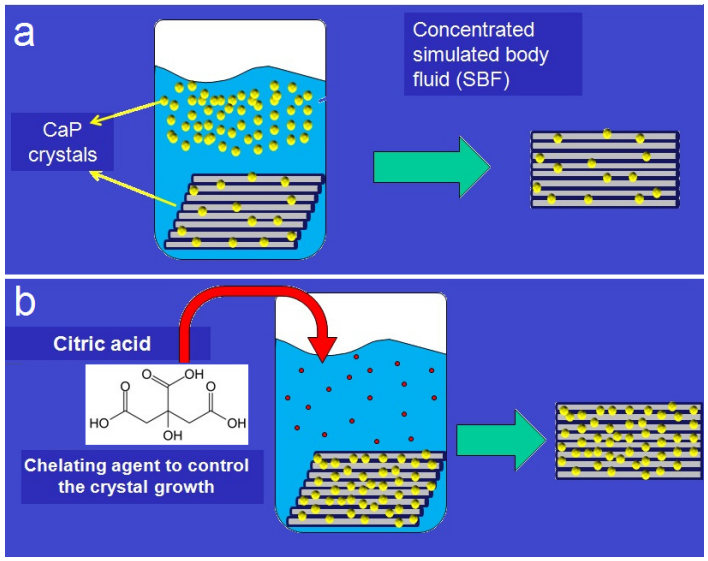

Figure 2.1. Nucleation of CaP crystals on the surface of nanofibers a. without addition of chealting agent, b. with addition of chelating agent such as citric acid

Carboxylic acid-rich organic acids like citric and malic acids account for 5.5% of the organic matter in natural bone.[53] All tested organic acids are naturally present in fruit and vegetables. CA is the dominant organic acid in citrus fruits while MA is found in apple and pear.[60] Tomato contains 9% CA, 4% MA, and 0.5% AsA based on dry mass.[61] Rice and soybean contain SalA[62] while grapes and grapefruit are a major source of TART and HCA.[63, 64] The CaP nucleated microsheets were characterized with respect to particle size, crystallite size, percent crystallinity, calcium to phosphate ratio, CaP content, and compressive modulus. Next, CaP nucleated microsheets were seeded with hMSCs and cultivated in osteogenic medium. The cell-seeded microsheets were characterized by cell number, alkaline phosphatase (ALP) activity, and calcium content with incubation time. Results show that the addition of HCA, CA, and TART to the nucleation solution significantly increased the CaP content of the microsheets whereas only the addition of CA and AsA to the nucleation solution significantly increased osteogenic differentiation of hMSCs seeded on the microsheets.

2. Experimental

2.1. Nanofiber Electrospinning

The solution for electrospinning was prepared by dissolving 8 wt% PLA and 1.5 wt% LMPLA-GLU in HFIP (there was no LMPLA-GLU in "without GLU" samples") as we previously described.[42] The electrospinning solution loaded in a 1 mL syringe was injected through a 21-gauge needle (PrecisionGlide, 0.7 mm I.D., Becton-Dickinson, Franklin, NJ) via a KDS100 syringe pump. The positive and ground electrodes of the high-voltage power source were connected to the needle and the custom-built rotating

wheel, respectively.[42] The aligned nanofibers were electrospun using a 0.8 mL/h injection rate, 20 kV electric potential, 7.5 cm needle-to-needle distance, and wheel diameter and rotation speed of 20 cm and 1800 rpm, respectively, as we previously optimized.[65-67] The collected aligned nanofiber microsheet from a 0.8 mL solution had a thickness of 6 μm. The average size of the aligned fibers was 200 ±60 nm.[42] The electrospun PLA/LMPLA-GLU nanofibers are hereafter denoted by NF.

2.2. . Mineralization of NF in Modified Simulated Body Fluid

A stock solution of 10-fold concentrated SBF (10xSBF) was prepared by dissolving NaCl, KCl, $CaCl_2•H_2O$, $MgCl_2•6H_2O$, NaH_2PO_4 in distilled deionized (DI) water as described.[42] Next, one of the organic acids was added to the solution in concentrations ranging from zero to 15 mM. Molecular structure and pKa value of the organic acids are given in Table 1. Then, the pH of the solution was adjusted to 7.4 by addition of sodium bicarbonate ($NaHCO_3$) to the mineralization solution. The solution was maintained at ambient conditions for 15-45 min to equilibrate and solution-nucleated CaP crystal was removed by filtration with a 220 nm pore-size filter. Next, the nanofiber microsheets were submerged in the organic acid-supplemented 10xSBF with agitation on an orbital shaker for 12 h. The containers were sealed with Parafilm to prevent diffusion of CO_2 from the atmosphere and maintain a constant solution pH. The nucleation solution was changed every 6 h to maintain a constant concentration of calcium and phosphate ions in solution with incubation time. The NF microsheets mineralized in 10xSBF solution supplemented with TART, HCA, CA, MA, AsA and SalA are hereafter denoted by TART, HCA, CA, MA, AsA and SalA, respectively.

2.3. Characterization of CaP-Nucleated Nanofiber Microsheets

The extent of CaP nucleation and growth on NF microsheets was measured using a QuantiChrom calcium assay (Bioassay Systems, Hayward, CA) according the manufacturer's instructions.[42]

Table 2.1. Molecular structure and pKa of the organic acids.

Organic acid	Molecular structure	pK
Hydroxycitirc acid (HCA)	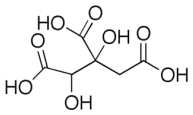	pK_1 =3.2 pK_2 =4.51 pK_3 =6.1
Citric acid (CA)	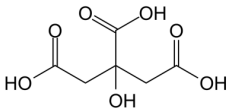	pK_1 =3.13 pK_2 =4.78 pK_3 =6.4
Tartaric acid (TART)	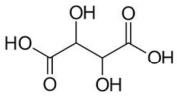	pK_1 =3.04 pK_2 =4.36
Malic acid (MA)	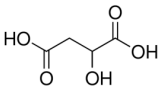	pK_1 =3.4 pK_2 =5.2
Salicylic acid (SalA)	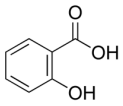	pK_1 =2.98 pK_2 =13.82
Ascorboc acid (AsA)	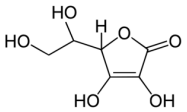	pK_1 =4.17 pK_2 =11.6

Briefly, the calcium content of 1 mg NF microsheet was dissolved in 0.4 mL of 1M HCl. Next, 5 µL aliquot of the suspension was added to 200 µL of the kit working

solution. After 3 min incubation at 37°C, absorbance was measured on a Synergy HT plate reader at a wavelength of 612 nm and correlated to the equivalent amount of Ca^{2+} using a calibration curve constructed from reference solutions with known Ca^{2+} concentrations. The total CaP content was determined from the measured Ca^{2+} content and calcium to phosphate (Ca/P) ratio obtained from energy-dispersive X-ray spectrum (EDS) of the sample. The measured CaP content was divided by the weight of NF sheet to determine CaP weight percent in each sample with incubation time in nucleation solution. The CaP-nucleated nanofiber microsheets were imaged with a VEGA3 SBU variable pressure scanning electron microscope (SEM; Tescan, Kotoutovice, Czech Republic) at an accelerating voltage of 8 KeV. Samples were coated with gold using a Denton Desk II sputter coater (Moorestown, NJ) at 20 mA current for 75 sec. The average fiber size of the microsheets and CaP particle size were determined from the analysis of SEM images using the ImageJ software (National Institutes of Health, Bethesda, MD) as described previously.[42] An EDS system (Tescan) connected to the SEM was used to analyze the samples for elemental composition and Ca/P ratio of the samples as described.[68]

Crystallinity and crystallite size of the nucleated CaP on microsheets were measured by wide-angle X-ray diffraction (XRD) using a Philips 405S5 diffractometer (Eindhoven, Netherlands) as we previously described.[68] The diffraction spectrum was collected with a CuKα radiation source (λ=1.54059 Å) at 30 KeV over Bragg angles (2Θ) ranging from 10 to 50 degrees with a step size of 3 degrees/min^{-1}. Average crystallite size (L) of CaP particles nucleated on the microsheets was calculated from the XRD spectrum using Scherrer equation [69, 70]

$$L = \frac{K\lambda}{\beta \cos \theta} \quad (1)$$

where K is a shape factor with a value close to unity, λ is the X-ray wavelength, β is full width at half maximum (FWHM) of the peak at the diffraction angle θ. The (002) reflection peak (2Θ=25.8) in the XRD spectrum was used to calculate crystallite size of the CaP particles as described. [71, 72] The fraction of crystalline phase in the CaP nanoparticles (X_C) was calculated using the following equation developed for calcium phosphate crystals[73]

$$X_C \approx 1 - \frac{\nu_{112/300}}{I_{300}} \quad (2)$$

where I_{300} is intensity of the (300) diffraction peak and $\nu_{112/300}$ is intensity of the hollow region between (112) and (300) diffraction peaks in the XRD spectrum of the samples.

For determination of compressive modulus, a 10 layered nanofibrous microsheets with the overall thickness of 60 μm was loaded on the Peltier plate of an AR2000 rheometer (TA Instruments, New Castle, DE) and subjected to a uniaxial compressive force at a displacement rate of 7.5 mm/s. The slope of the linear fit to the stress–strain curve for 5–10% strain was taken as the elastic modulus (E) of the mineralized matrix as we previously described.[74] For determination of mass loss, the annealed samples were incubated in simulated body fluid (SBF) at 37ºC and under mild agitation. At each time point, samples were removed from SBF, washed three times with DI water and dried under vacuum. The dry sample weight was measured and compared with the initial dry weight to determine the fractional mass remaining as described [75].

2.4. Cell Seeding on Mineralized Microsheets

hMSCs were cultivated at 5000 cells/cm^2 in a high glucose DMEM medium supplemented with 10% FBS, 100 units/mL penicillin and 100 µg/mL streptomycin (basal medium) with medium refreshment every three days. After reaching 70% confluency, the cells were detached with 0.1% trypsin- 0.03% EDTA and sub-cultivated at a ratio of 1:3 for <5 passages, according to supplier's instructions. For cell seeding, edges of the microsheets on 12 mm circular glass coverslips were covered with a medical-grade silicone sealant (Dow Corning, MI) to prevent separation of the microsheet from coverslip in the cell culture medium. The microsheets were sterilized by ultraviolet (UV) radiation for 1 h followed by immersion in 70% ethanol for 30 min and washing three times with sterile PBS. We have previously shown that fiber alignment and size, or attachment of CaP nanoparticles nucleated on the fibers are not affected by the sterilization procedure.[42] After incubation in basal medium for 1 h, each microsheet sample was seeded with 60 µL hMSC cell suspension ($1.7x10^6$ cells/mL in basal medium) at a surface density of $1x10^5$ cells/cm^2. After incubation for 24 h for cell attachment, the medium was replaced with osteogenic medium (basal medium plus 100 nM dexamethasone, 50 µg/mL ascorbic acid, 10 mM ß-glycerophosphate). CA microsheets seeded with hMSCs and incubated in basal medium was used as the control group. The hMSC-seeded microsheets were incubated in a humidified 5% CO_2 incubator for 21 days.

2.5. Osteogenic Differentiation of Cell-Seeded Mineralized Microsheets

At each time point (0, 7, 14 and 21 days), cell-seeded microsheet samples were washed with serum-free DMEM for 8 h to remove serum proteins followed by washing

with PBS. Next, samples were lysed with 10 mM Tris supplemented with 0.2% triton in PBS and the lysed samples were used for measurement of DNA content, ALP activity, and calcium content. Double-stranded DNA content, ALP activity and calcium content of the samples were measured with Quant-it PicoGreen, QuantiChrom ALP and QuantiChrom Calcium Assays, respectively, as we previously described. [42, 75] To determine the extent of mineralization of the samples by the seeded hMSCs at each time point, the measured calcium intensities at time zero was used a baseline to subtract the calcium contribution from the CaP-nucleated fibers prior to cell seeding. The measured ALP activities and calcium contents were normalized to cell number by dividing to DNA content at each time point. For imaging the extent of hMSC-induced mineral deposition, the microsheets were stained with Alizarin red using the following procedure. The cells on the microsheets were fixed with 10% paraformaldehyde. Next, the fixed samples were covered with a solution of Alizarin red, prepared according to the manufacturer's instructions, and incubated in the dark at ambient conditions for 20 min. Then, a Nikon Optiphot epifluorescence microscope was used to image the samples for extent of nodule formation and the images were analyzed for average size of the nodules by the ImageJ software as we previously described [42].

2.6. Statistical analysis.

Data are expressed as means ± standard deviation. All experiments were done in triplicate. Significant differences between groups were evaluated using a two-tailed Student's t-test. A value of $p<0.05$ was considered statistically significant.

3. Results

3.1. CaP nucleation on the mineralized microsheets

Figure 2.2a and 10b show the percent CaP nucleated on the microsheets with GLU (1a) or without GLU (1b) as a function of organic acid concentration in 10xSBF. CaP content of the GLU incorporated microsheets incubated for 12 h in 10xSBF without the addition of organic acids was 160±20%. That was significantly higher than the CaP content of the "without GLU" microsheets incubated for 12 h in 10xSBF (40%, see Figure 2.2b). SalA and AsA did not significantly affect CaP content of "with GLU" microsheets at concentrations <4mM. CaP content of the "with GLU" microsheets increased to 170±10% and 175±5%, respectively, as SalA and AsA concentrations increased to 10 mM and CaP content remained unchanged with further increase in SalA or AsA concentration. CaP content of the "with GLU" microsheets peaked at 200%±20 as MA concentration increased to 8 mM and then decreased to 185%±15 at MA concentration of 15 mM. CaP content of the "with GLU" microsheets incubated with CA, TART, and HCA increased with organic acid concentration, peaked at 6 mM concentration, and then decreased with increasing organic acid concentration. CaP content of the "with GLU" microsheets incubated with 6mM concentration of CA, TART, and HCA was 225±30%, 225±20% and 240±25%, respectively, but CaP content decreased to 200±20%, 205±15% and 215±20% at 15 mM organic acid concentration. The CaP content of "without GLU" microsheets increased from 40 wt% to a maximum of 103, 114, 133, 155, 160 and 175 wt% when the nucleation medium was supplemented with SalA, AsA, MA, CA, TART and HCA, respectively. The peak CaP content of the "with GLU" microsheets incubated with 6 mM HCA was comparable with CaP content

of the natural compact bone.[10] Figure 2.3 shows CaP content of the "with GLU" microsheets as a function of incubation time in 10xSBF supplemented with one of the organic acids at a concentration corresponding to the peak CaP content in Figure 2.2. In Figure 2.3, "None" represents the group without addition organic acids and Ctrl represents the group without addition of neither organic acid nor GLU. CaP content of the microsheets monotonically increased with incubation time in the first 16 h and reached a plateau at longer times. CaP content did not change significantly when incubation time was increased from 16 to 24 h for all organic acids and the plateau CaP content was highest for HCA supplemented 10xSBF at 244±10% and lowest for SalA at 174±8%. Results in Figures 2.2-2.3 show that the addition of HCA to 10xSBF had the greatest effect on CaP content of the microsheets followed by TART, CA, and MA. Further, the optimum concentration and optimum incubation time was 6 mM and 12 h, respectively.

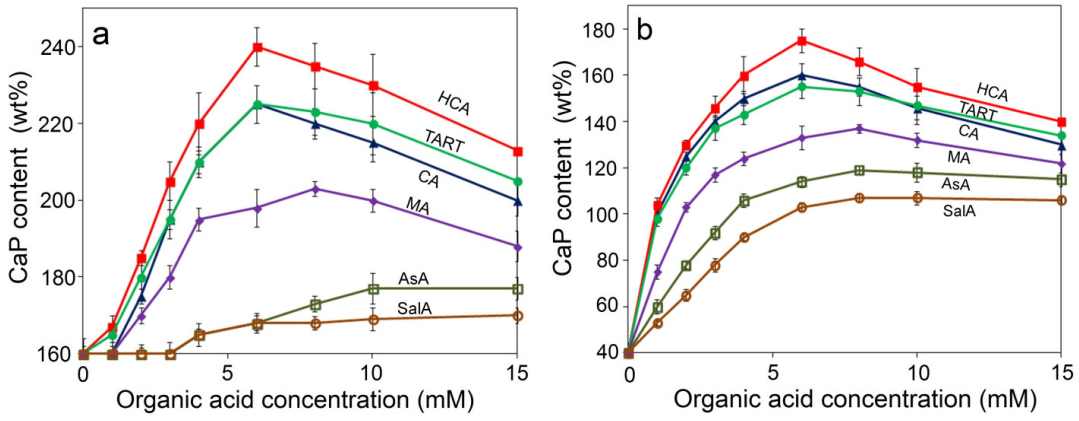

Figure 2.2. Effect of organic acid concentration added to the concentrated SBF on CaP content of DL-PLA nanofiber microsheets (a) with and (b) without GLU for different organic acids after 16 h incubation.

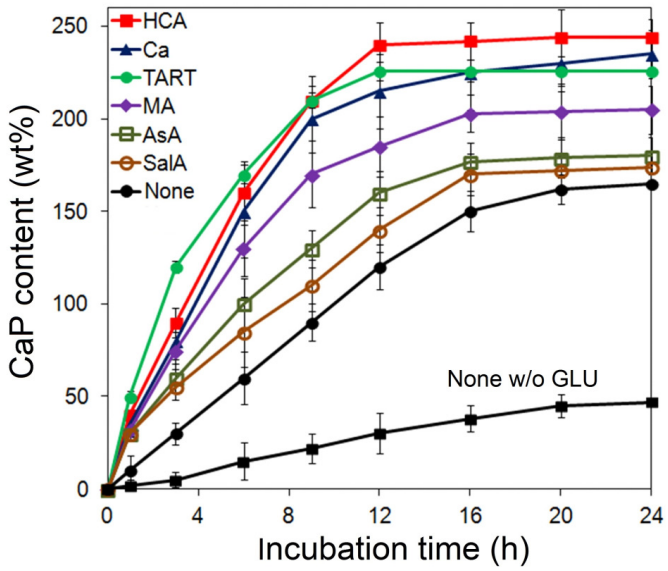

Figure 2.3. Effect of incubation time in the concentrated SBF supplemented with different organic acids on CaP content of DL-PLA nanofiber microsheets at organic acid concentration corresponding to maximum CaP content in Figure 2.2.

Figure 2.4 shows XRD spectra of the mineralized "with GLU" microsheets after incubation for 12 h in 10xSBF supplemented with optimum concentration of the organic acid (Figure 2.2a). The XRD spectra of pristine nanofiber microsheet without CaP nucleation (PLA) and pure hydroxyapatite (HA) are also included in Figure 2.4. The broad diffraction peak in the spectrum of pristine PLA microsheet centered at $2\Theta = 16°$ is characteristic of the amorphous poly(DL-lactide).[76] Calcium phosphates that mineralize from solution at ambient conditions are HA, amorphous calcium phosphate (ACP), dicalcium phosphate dihydrate (DCPD), and octacalcium phosphate (OCP). [77, 78] The relatively sharp diffraction peaks in the spectra of HA and mineralized microsheets centered at $2\Theta = 25.8°$, 31.8°, 32°, 33°, and 46° corresponded to (002), (211), (112), (300) and (222) planes of HA, respectively. [72, 76-78] The relatively broad diffraction peak overlapping the HA peaks at $2\Theta = 31.8°$, 32°, and 33°, which was absent in the spectrum

of HA, was due to the formation of ACP in the mineralized microsheets.[70, 77] The characteristic diffraction peaks for crystalline OCP (2Θ = 16° and 24°) and DCPD (2Θ = 29.2°, 34.4°, and 11.4°) were absent in the spectra of mineralized microsheets[72, 77, 78].

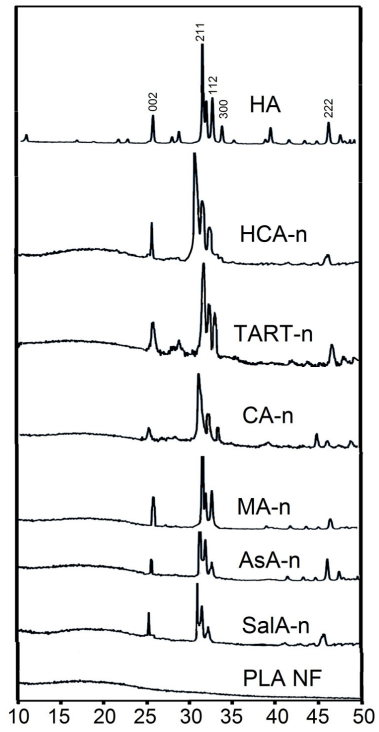

Figure 2.4. X-ray diffraction spectra of DL-PLA nanofiber microsheets with GLU incubated in the concentrated SBF supplemented with HCA, TART, CA, MA, AsA, and SalA organic acids for 16 h at the concentration corresponding to the maximum CaP content in Figure 2.3.

The EDS spectra of the mineralized "with GLU" microsheets incubated in 10xSBF for 12 h with optimum concentration (Figure 2.2) of HCA, TART, CA, MA, AsA, and SalA are shown in Figures 2.5a through f. The elemental Ca/P ratio calculated from the calcium and phosphorous peaks in Figure 2.5 and EDS data for "without GLU" microsheets (data not shown) are presented in Table 3 together with crystallinity and size of the crystallites (XRD images) and size of the CaP particles nucleated on nanofibers of

the microsheets (SEM images). Crystallinity of "with GLU" microsheets incubated in 10xSBF without organic acids was 21±2%. TART and AsA incubated microsheets (TART and AsA) had the highest and lowest percent crystallinity, respectively, among all organic acids with 39±2% and 20±2%. SalA, HCA, CA, and MA incubated microsheets (SalA, HCA, CA, and MA) had percent crystallinity of 23±1%, 31±1%, 30±1%, and 35%±3, respectively, which was in the range of crystallinity of cortical and cancellous bone (33-37%).[79] The size of crystallites ranged between 31±2 and 62±4 nm with TART and Sal having the lowest and highest crystallite size, respectively. In comparison, the crystallite size for the "with GLU" microsheets mineralized in the absence of organic acids was 60±5 nm. Ca/P ratio of the microsheets ranged between 1.68±0.03 for TART and 1.91±0.05 for AsA with the microsheets mineralized in the absence of organic acids having a Ca/P ratio of 1.88±0.1. TART incubated "with GLU" microsheets had Ca/P ratio of 1.68 which was closest to that of natural bone at 1.67 [79] followed by HCA and CA with Ca/P ratio of 1.71 and 1.77, respectively. Crystals formed on "without GLU" microsheets had lower crystallinity, higher Ca/P ratio and larger crystallite size compared to the ones formed on "with GLU" microsheets.

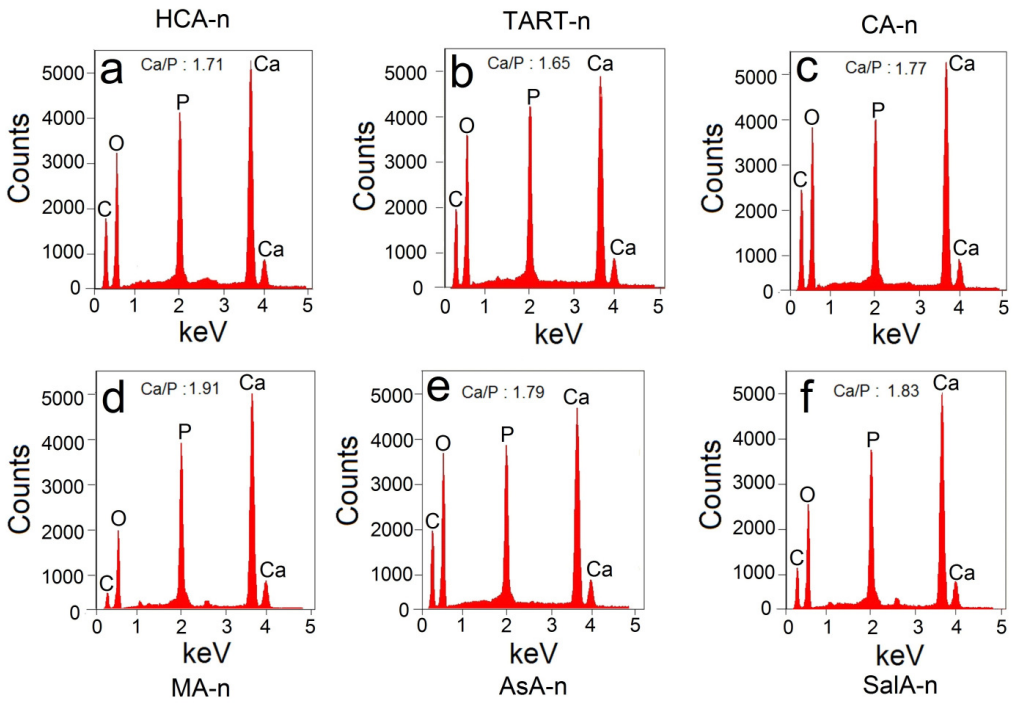

Figure 2.5. EDS spectra of DL-PLA nanofiber microsheets incubated in the concentrated SBF supplemented with HCA, TART, CA, MA, AsA, and SalA organic acids for 16 h at the concentration corresponding to the maximum CaP content in Figure 2.2.

Figure 2.6a-b shows the mass loss of the mineralized "with GLU" microsheets with incubation time in SBF at 37°C. The mass remaining of pristine PLGA and PLA NFs was 0 % and 68%±5, respectively, whereas the mass remaining of mineralized NFs ranged between 85 %±2 and 93 %±1 after 35 days of incubation in SBF.

Table 2.2. Percent crystallinity, calcium to phosphate (Ca/P) ratio, crystallite size, and particle size of calcium phosphates particles nucleated on DL-PLA nanofiber microsheets (a) with and (b) without GLU.

a With GLU

Groups	Crystallinity(%)	Ca/P ratio	Crystallite size(nm)	Particle size(nm)
None	21±2	1.88±0.1	60±5	210±15
HCA	31±1	1.71±0.05	33±1	110±10
TART	39±2	1.68±0.03	31±2	95±8
CA	25±1	1.79±0.02	36±2	118±12
MA	35±3	1.77±0.04	33±3	104±5
AsA	20±2	1.91±0.05	55±3	156±15
SalA	23±1	1.83±0.04	62±4	180±9

b Without GLU

Groups	Crystallinity(%)	Ca/P ratio	Crystallite size(nm)	Particle size(nm)
None	13±2	2.0±0.1	76±6	270±33
HCA	26±3	1.81±0.06	38±2	123±12
TART	30±3	1.78±0.04	35±3	110±9
CA	20±4	1.9±0.03	41±1	139±15
MA	26±5	1.87±0.05	36±2	115±5
AsA	15±6	1.97±0.03	68±3	196±19
SalA	17±7	1.94±0.06	73±5	220±25

The mass losses are magnified in Figure 2.6b to show the effect of organic acid added to 10xSBF on mass loss of the mineralized microsheets. HCA with 12 %±2 mass loss had the slowest degradation while SalA with 19 %±3 mass loss had the fastest degradation among mineralized NFs after 42 days.

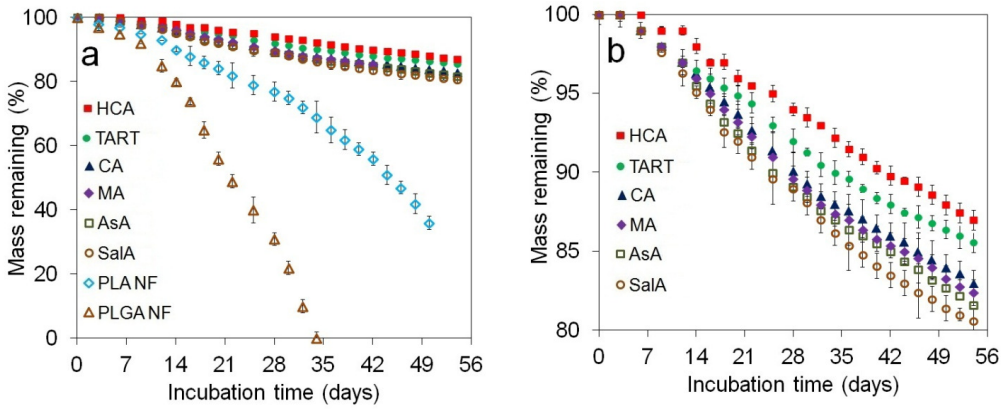

Figure 2.6. (a) Mass loss of DL-PLA nanofiber microsheets incubated in the concentrated SBF supplemented with HCA, TART, CA, MA, AsA, and SalA organic acids for 16 h at the concentration corresponding to the maximum CaP content in Figure 2.2. In (b) the y-axis is expanded (100-95% mass remaining) to show mass remaining for the mineralized microsheets. PLGA NF and PLA NF are PLGA and DL-PLA nanofiber microsheets with GLU and without incubation in SBF. There was not a significant pair-wise difference between the mass loss of CA and MA, CA and TART, and TART and MA groups by ANOVA test. There was a significant pair-wise difference between the mass remaining of other groups. Error bars correspond to means±1 SD for n=3.

SEM images in Figure 2.7 and Figure 2.8 show the effect of organic acid added to 10xSBF on size and distribution of the CaP nanoparticles nucleated on nanofibers of the "with GLU" and "without GLU" microsheets respectively. The average size of the nucleated CaP nanoparticles determined from the SEM images is presented in Table 3. The average particle size on "with GLU" microsheets ranged from 95±8 nm for TART to 180±9 nm for SalA whereas the average particle size on "without GLU" microsheets ranged from 110±9 nm for TART to 270±33 nm for SalA. The size of the CaP crystals formed on both "with GLU" and "without GLU" microsheets in the organic acid incorporated solutions were significantly lower than the size of the ones formed in the absence of organic acids (None groups in Figure 2.7 and Figure 2.8). The number density

of CaP nanoparticles in AsA and SalA samples was lower than that of the other organic acid incorporated samples, consistent with the lower CaP content of AsA and SalA microsheets (see Table 4). The effect of organic acid in CaP nucleation medium on compressive modulus of the microsheets is presented in Table 4. Modulus of the "with GLU" and "without GLU" microsheets increased by 2.9 and 10.0 folds with CaP nucleation in the absence of organic acids in the nucleation solution (None group in Table 3). The modulus of both "with GLU" and "without GLU" microsheets significantly increased with incorporation of organic acids within the nucleation solution. Furthermore, the modulus of "with GLU" microsheet was significantly higher than the one for "without GLU" microsheet in the presence or absence of organic acids. HCA "with GLU" microsheets with CaP content of 240±10 wt% had the highest modulus of 260±40 MPa compared to other mineralized microsheets which was 21.7-fold higher than the modulus of pristine DL-PLA microsheets

Table 2.3. Maximum CaP content and compressive modulus of DL-PLA nanofiber microsheets with and without GLU incubated in the concentrated SBF supplemented with different organic acids.

	With GLU		Without GLU	
Group	CaP content(wt%)	Elastic modulus (MPa)	CaP content(wt%)	Elastic modulus (MPa)
NF	0	12±3	0	12±3
None	160±12	120±20	40±6	35±5
HCA	240±10	260±40	175±25	150±30
TART	225±8	242±20	155±16	125±15
CA	225±10	210±30	160±18	130±40
MA	203±12	199±10	133±12	109±20
AsA	177±15	161±20	114±10	91±10
SalA	170±7	147±10	103±12	80±10

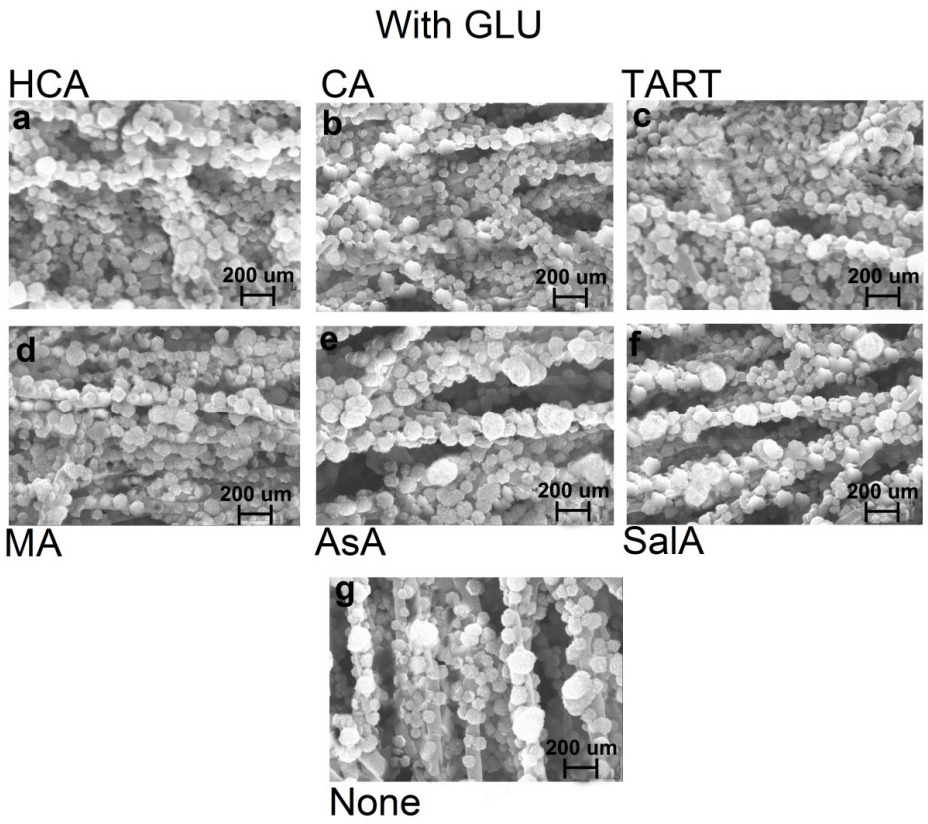

Figure 2.7. SEM images of DL-PLA nanofiber microsheets with GLU incubated in the concentrated SBF supplemented with HCA (a), TART (b), CA (c), MA (d), AsA (e), and (f) SalA for 16 h at the concentration corresponding to the maximum CaP content in Figure 2.2. None SEM image is DL-PLA nanofiber microsheets with GLU incubated in the concentrated SBF without the addition of organic acids for 16 h at the concentration corresponding to the maximum CaP in Figure 2.2.

3.2. Osteogenic differentiation of hMSCs on nanofiber microsheets

hMSCs were seeded on mineralized microsheets and cultured in complete osteogenic medium (basal medium plus dexamethasone, ascorbic acid (0.3 mM), ß-glycerophosphate).

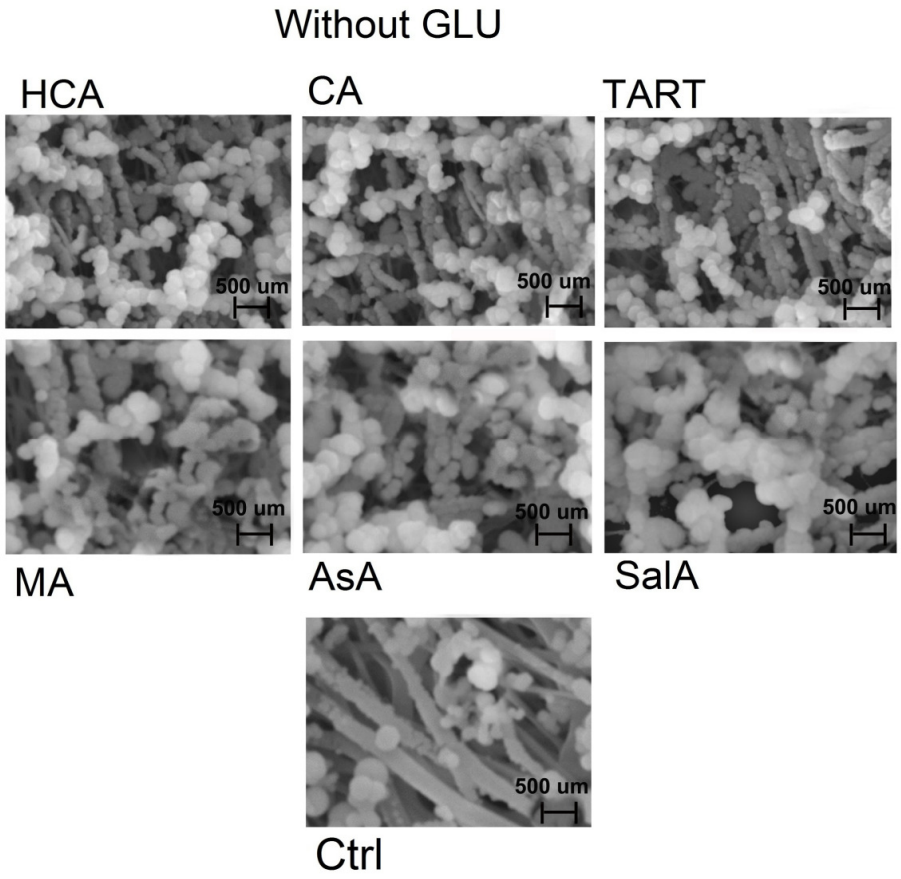

Figure 2.8. SEM images of DL-PLA nanofiber microsheets without GLU incubated in the concentrated SBF supplemented with HCA (a), TART (b), CA (c), MA (d), AsA (e), and (f) SalA for 16 h at the concentration corresponding to the maximum CaP content in Figure 2.2. None SEM image is DL-PLA nanofiber microsheets without GLU incubated in the concentrated SBF without the addition of organic acids for 16 h at the concentration corresponding to the maximum CaP in Figure 2.2.

Experimental groups were hMSCs seeded on "with GLU" microsheets mineralized in the absence of organic acids (None) or presence of CA, AsA, SalA, HCA, MA and TART organic acids within the nucleation solution. hMSCs seeded on CA group and cultured in basal medium (CA-BM) was used as a control. DNA content of hMSCs cultured on the NF microsheets is shown in Figure 2.9. DNA content of the hMSCs in the control CA-BM group (black diamond) increased slightly with incubation time while the

DNA content of groups incubated in osteogenic medium decreased slightly with time. We have previously shown that at high initial cell seeding density used in our experiments, cell content of the microsheets decreases with incubation time as the cells undergo osteogenic differentiation.[42] DNA content of hMSCs seeded on CA, AsA, SalA, HCA, MA and TART with a seeding density of 10^5 cells/ cm^2 and incubated in osteogenic medium decreased slightly over 7 days of culture (Figure 2.9a) while the DNA content of hMSCs seeded on the same groups with two orders of magnitude lower seeding density (10^3 cells/cm^2) increased significantly after 7 days of culture within the osteogenic medium.

ALPase activity of hMSCs seeded on NF microsheets is shown in Figure 2.9b. ALPase activity of hMSCs seeded on CA-BM group incubated in basal medium did not increase significantly with time (black diamond). ALPase activity of hMSCs in CA, AsA and SalA groups peaked to the value of 5800±300, 5300±250 and 4800±150 IU/mgDNA, respectively at day 14, which was higher than that of None group with 4500±300 IU/mgDNA at day 14. The peak value of ALPase activity for hMSCs seeded on HCA, MA and TART microsheets was 3800±200, 3200±100 and 3000±150 IU/mgDNA, respectively, after 14 days which was lower than that for None group. Calcium content of hMSCs seeded on mineralized NFs and cultured in osteogenic medium (basal medium for CA-BM) group is shown in Figure 2.9c. All calcium content values were subtracted from the values at day 1 to isloate the Ca deposited by cells from CaP deposited on fibers prior to cell seeding. Calcium content of the hMSCs seeded on CA-BM did not significantly change after 21 days of incubation in basal medium. The calcium content of all other groups increased slightly from day 4 to 7 and then increased monotonically over 21 days.

The calcium content of CA, AsA was 1200±100 and 1100±100 (mg/mg DNA) respectively after 21 days of incubation, higher than calcium content of None group (980±85 mg/ mg DNA). Calcium content of SalA, did not have a significant difference with that of None group at day 21. Calcium content of HCA, MA and TART groups was 750±60, 610±50 and 550±55 mg/mgDNA, respectively, after 21 days of incubation which was lower than the calcium content of None group.

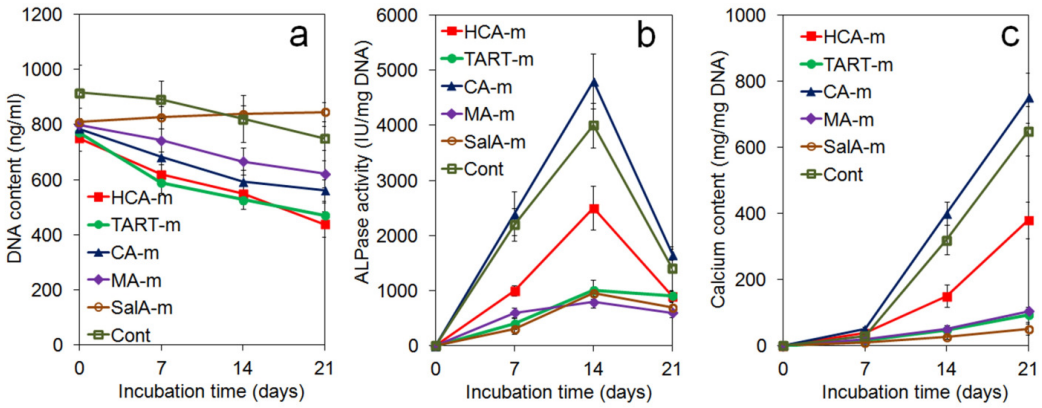

Figure 2.9. DNA content (a) ALP activity (b) and calcium content (c) of hMSCs seeded on mineralized DL-PLA nanofiber microsheets with GLU as a function of incubation in osteogenic medium. CA-BM group (black diamond) is CA group incubated in basal medium, group incubated in osteogenic medium. Error bars correspond to means±1 SD for n=3.

Image in Figure 2.10 show Alizarin Red Staining of hMSCs seeded on "with GLU" mineralized NF microsheets and cultured in osteogenic medium for 21 days. Controls included NF microsheets without CaP deposition and without hMSCs seeding (NF, 11i), NF microsheets with CaP deposition and without hMSCs seeding (NF+CaP, 11h) and NF microsheets with CaP deposition in the absence of organic acids within the nucleation solution and seeded with hMSCs (None, 11g). The presence of dark red areas in Figure

2.10a-g as opposed to Figure 2.9h and 2.10i showed the contributing effect of hMSCs to mineralization. A relatively high density of orange-red areas on the CA, AsA, SalA and None groups qualitatively confirmed a higher Calcium content (See Figure 2.10c) of the aforementioned groups compared with that of MA, TART and HCA groups. Formation of bone nodules, three dimensional specifically mineralized and organized structures with proliferation, differentiation and mineralization stages of hMSCs simultaneously [80], was observed as large dark spots only on the CA group (see Figure 2.10b). The number density and total area of bone nodules on the CA group was 86 counts/cm^2 and 1.8 ± 0.2 mm^2/cm^2. Dark spots on the AsA and None groups (see Figure 2.10e and 2.10g) were smaller (<35 μm) to be considered as bone nodules based on the previous reports [80, 81] .

4. Discussion

In this work, we investigated the effect of organic acids with different number of hydroxyl and carboxylic acid groups (see Table 1) in the simulated body fluid on the extent of CaP nucleation on nanofiber microsheets . An attractive approach to retard CaP crystal nucleation in solution and enhance nucleation on the fiber surface is to increase the solubility of calcium and phosphate ions in the nucleation solution.[78] Carboxylate-rich organic acids like citric acid which account for 5.5% of the organic matter in the natural bone,[53] inhibits CaP crystal nucleation in solution.[58, 59] Citric acid ($C_6H_8O_7$) with three carboxylate groups is ionized to citrate ion ($C_6H_5O_7^{3-}$) (hereafter referred as Cit) in 10xSBF nucleation medium.

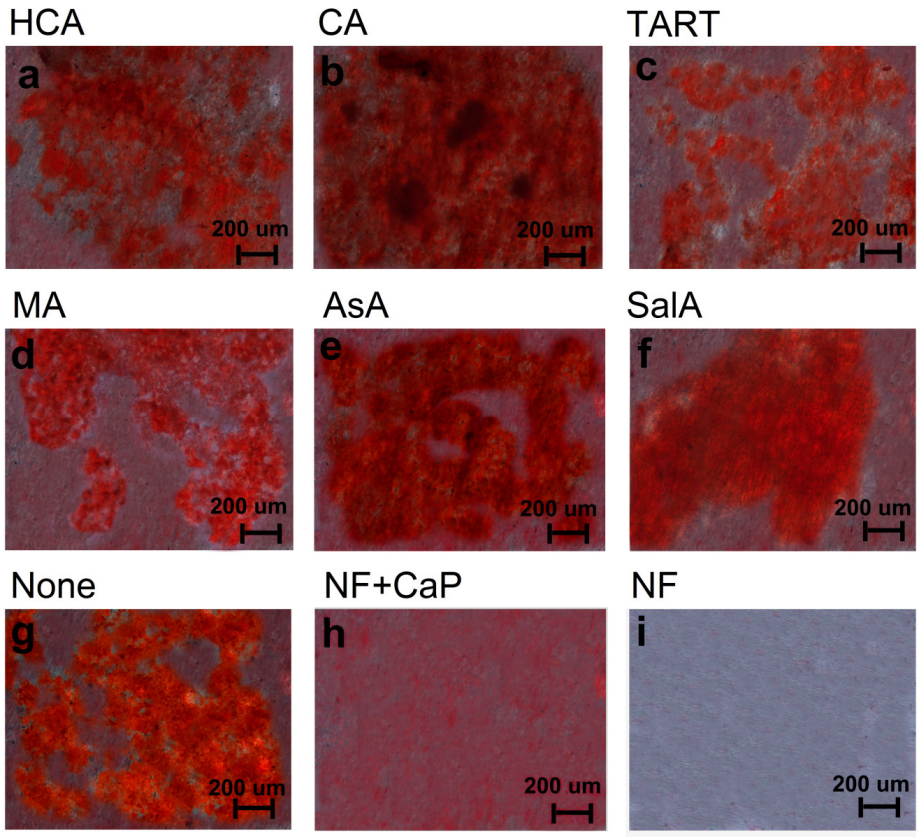

Figure 2.10. Alizarin red staining of hMSCs seeded on mineralized DL-PLA with GLU and incubated in osteogenic medium for 21 days. NF+CaP and NF groups are mineralized and pristine nanofiber microsheets, respectively.

Subsequently, the citrate ions are adsorbed on the surface of positively charged calcium ions to form a Ca-Cit complex. The negatively charged Ca-Cit complex is electrostatically repelled by the phosphate ions (PO_4^{3-}) [53, 58, 82]. The stability of Ca-Cit complex in solution depends on Cit concentration with the chelated $Ca(Cit)^-$ complex formed at low Cit concentrations[72] and the stable $[Ca(Cit)_2]^{-4}$ complex formed at high Cit concentrations.[59] Therefore, the presence of Cit ions at low concentration inhibits the formation of CaP crystals in the nucleation solution, effectively increasing the probability

of CaP nucleation on GLU sites on the surface of nanofibers. Consequently, CaP content of the NF microsheets increased with increasing CA concentration from zero to 6 mM in the presence of Ca(Cit)- complex. As the CA concentration was increased to values >6 mM, the stable [Ca(Cit)2]-4 formed at high concentrations inhibited CaP nucleation on the fiber surface.[59] HCA, TART, MA, SalA, and AsA organic acids form complexes with Ca ions in the nucleation solution through their carboxylate groups similar to that of citric acid.[83] Therefore, the biphasic trend of CaP content of the NF microsheets observed in Figure 2.2 can be attributed to a change in the stability of organic acid-calcium complex with organic acid concentration in the nucleation solution.

The maximum CaP content of "with GLU" NF microsheets after 12 h incubation in 10xSBF supplemented with HCA, TART, CA, MA, AsA, and SalA was 240±10%, 225±8%, 225±10%, 177±15%, 203±12%, and 170±6=7%, respectively, compared to 160±12% without organic acid. The difference in peak CaP contents can be attributed to the different number of carboxylic acid and hydroxyl groups in the organic acids. Higher number of carboxylate groups in the organic acid increased chelation between calcium ions and organic acid molecules in the nucleation solution[83] whereas higher number of hydroxyl groups in the organic acid enhanced hydrogen bonding interaction between the Calcium-organic acid complex and the carboxylic acid groups and electronegative groups present on GLU as well as fiber surface. [59] According to Figure 2.2a and 1.1b, the CaP content of both "with GLU" and "without GLU" NF microsheets increased significantly with addition of organic acids to the nucleation solution. However, the peak values for calcium content were higher in "with GLU" microsheets. Therefore, while Calcium-

organic acid complex can bind to the fiber surface in the absence of GLU, the presence of GLU contributed to the CaP nucleation significantly.

CaP content of the NF microsheets decreased as the organic acid in the nucleation medium was changed from HCA with three carboxylic acids to TART and MA with two carboxylic acids and SalA with one carboxylic acid group (see Tables 2 and 4). Further, HCA with two hydroxyl groups resulted in higher CaP of the microsheets when added to the nucleation medium compared to CA with a single hydroxyl group although both organic acids had three carboxylic acid groups. Similarly, CaP content of the microsheets incubated in SBF supplemented with TART (two hydroxyl groups) was higher than MA with one hydroxyl group while both organic acids had the same number of carboxylic acids. The higher CaP content of the microsheets incubated in SBF supplemented with AsA compared with MA was attributed to the higher number of hydroxyl groups in AsA (three for AsA versus one for MA). CaP content of the microsheets was 240% after 12 h incubation in HCA-supplemented 10xSBF which was higher than the CaP content of natural cancellous bone (190%)[52] and cortical bone (230%).[10] The incubation time to reach 95% of the plateau CaP content was 10 h which was significantly lower than the reported 4 days of incubation for CaP nucleation on the collagen nanofibers in 1.5xSBF supplemented with CA.[59]

XRD results demonstrated that the CaP nucleated on the NF microsheets was a mixture of HA and ACP. Further, the deviation of Ca/P ratio from that of pure HA (1.67, see Table 3) increased with decreasing crystallinity of the nucleated CaP on the microsheets. Therefore, the deviation of Ca/P ratio from that of HA was related to the changes in the amorphous phase of the CaP particles with a Ca/P ratio in the 1.2-2.2

range). [72, 77, 78, 84] The crystallinity of CaP particles on NF microsheets was highest when the nucleation medium was supplemented with TART or MA having two carboxylic acid groups which can be attributed to an optimal spacing of Ca ions on the surface of the growing crystals. The relatively large CaP particle size and crystallite size in microsheets incubated in AsA and SalA supplemented SBF (Table 3) can be attributed to the lower inhibitory effect of those organic acids on crystal growth. Since AsA and SalA had only one carboxylic acid group with a net negative charge of one, the propensity for complex formation with Ca ions on the fiber surface for AsA and SalA was lower than other organic acids with two or more carboxylic acid groups (see Table 3). The number of crystallites per CaP particle on the microsheets was calculated from the particle size, crystallite size, and crystallinity data in Table 3. The number of crystallites per particle on the microsheets incubated in SBF supplemented with HCA, TART, CA, and MA was 11, 11, 10 and 11, respectively, whereas that number was 4 and 5 for AsA and SalA. Therefore, the number of growing crystals on the surface of NF microsheets decreased and the size increased for those organic acids with lower inhibitory effect toward crystal growth (see Table 2.3 and Figure 2.7). Since the number of crystallites per particle was greater than unity for all organic acids, the nucleated particles had a polycrystalline structure interconnected by an amorphous phase.[72]

For equal CaP content, TART incubated microsheets with higher crystallinity had higher compressive modulus than CA incubated microsheets (see Table 4). The slower degradation of mineralized microsheets indicated that the CaP nanoparticles had slower degradation than the DL-PLA nanofibers.[43] The difference in degradation of the mineralized microsheets (Figure 2.6b) was related to differences in crystallinity and CaP

content. For example, microsheets incubated with AsA supplemented SBF with lowest crystallinity but higher CaP content than SalA and MA incubated microsheets had fastest mass loss among all microsheets. Conversely, microsheets incubated with HCA supplemented SBF with highest CaP content but lower crystallinity than TART and MA incubated microsheets had slowest mass loss among all microsheets.

The difference between DNA content of hMSCs seeded on the surface of mineralized fibers 1 day after culture could be related to the differences between the surface properties of mineralized fibers. It has been reported elsewhere that the surface adhesion of human gingival fibroblasts cells on an amorphous HA (~25% crystallinity) coating surface was higher than that of surfaces coated with higher crystalline HA (~ 63% and 97% crystallinity) [85]. Therefore, a higher DNA content of AsA, Ca and SalA groups compared with those of MA, TART and HCA groups could be due to a lower crystallinity of CaP particles hence higher adhesion of cells to the surface of former groups. Based on ALPase and calcium measurements, the presence of CA or AsA in the nucleation solution of microsheets had a positive effect on osteogenic differentiation of hMSCs while the presence of SalA did not have a significant effect and the presence of HCA, MA and TART within the nucleation solution was counterproductive in osteogenic differentiation of hMSCs. The contributing effect of CA to osteogenic differentiation of hMSCs was consistent with a reported contributing effect of calcium citrate in bone healing [86]. Further, it was shown elsewhere that an incorporation of CA into a cellulose based hydrogel improved osteogenic differentiation of hMSCs [87]. In addition, It is well established that the presence of AsA stimulates the osteogenesis through integrin-mediated intracellular signaling [88]. Addition of CA to the nucleation solution also

stimulated the formation of nodules >100 μm in size (Figure 2.10). Schecroun et al. reported that dexamethasone in the osteogenic medium inhibited nodule formation by hMSCs in 2D culture.[80] Our results indicate that the addition of CA to the nucleation solution hence the presence of citrate ion on the fiber surface stimulates nodule formation by hMSCs even in the presence of dexamethasone within the culture medium.

5. Conclusion

In this work, the effect of organic acids added to the simulated body fluid on CaP nucleation and osteogenic differentiation of human MSCs on nanofiber microsheets functionalized with a CaP nucleating glutamic acid peptide. Glutamic acid-functionalized aligned DL-PLA nanofiber microsheets were electrospun by blending high molecular weight DL-PLA with low molecular weight PLA conjugated with EEGGC peptide. The nanofiber microsheets were incubated in concentrated SBF supplemented with different organic acids for nucleation and growth of CaP nanoparticles on the surface of nanofibers. Organic acids included citric acid (CA), hydroxycitric acid (HCA), tartaric acid (TART), malic acid (MA), ascorbic acid (AsA), and salicylic acid (SalA). Addition of organic acids to SBF significantly increased CaP nucleation on the fiber microsheets and the extent of CaP nucleation depended on the number of carboxylic acid and hydroxyl groups in the organic acid. HCA-supplemented group had the highest CaP content at 240±10% followed by TART and CA with 225±8% and 225±10%, respectively. CaP nanoparticles nucleated on the fiber surface in TART-supplemented group had Ca/P ratio (1.68) and crystallinity (39%) closet to that of natural bone. Microsheets in HCA-supplemented group had the highest compressive modulus of 260±40 MPa followed by TART and CA with 225±8 and 225±10 MPa, respectively. The

presence of CA or AsA in the nucleation solution of microsheets had a positive effect on osteogenic differentiation of hMSCs while the presence of SalA did not have a significant effect and the presence of HCA, MA and TART within the nucleation solution was counterproductive in osteogenic differentiation of hMSCs. CA group also stimulated the formation of bone nodules on the microsheets.

CHAPTER 3: ENGINEERING A CORTICAL-BONE-MIMETIC NANOSTRUCTURED SHELL WITH INTERCONNECTED MICROCANALS

1. Introduction

Biodegradable scaffolds, as key artificial devices widely used in tissue engineering, aim to provide a desirable micro-environment that allows neo-tissue to be generated properly for repairing and replacing damaged tissues or organs. To improve the performance of tissue scaffolds, various material parameters, e.g. stiffness, porosity and permeability, have proven particularly crucial to determine the biomechanical environments within scaffold micro-architectures. The scaffold material and porous architecture design (here architecture refers to features 10 to 1,000 micrometres in size) play a significant role in tissue regeneration by preserving tissue volume, providing temporary mechanical function, and delivering biofactors. Intuitively, the best scaffold for an engineered tissue should be the ECM of the target tissue in its native state. One of the crucial characterizations of a tissue engineering scaffold is possessing sufficient mechanical properties to fill up the void space of the defect and simulating that of the native tissue. Therefore, scaffolds should provide mechanical and shape stability to the tissue defect. The intrinsic mechanical properties of the biomaterials used for scaffolding or their post-processing properties should match that of the host tissue. Recent studies on mechanobiology have highlighted the importance of mechanical properties of a scaffold

on the seeded cells. Additionally, a tissue engineering scaffold should provide void volume for vascularization, new tissue formation and remodeling so as to facilitate host tissue integration upon implantation. The biomaterials should be processed to give a porous enough structure for efficient nutrient and metabolite transport without significantly compromising the mechanical stability of the scaffold. On the one hand, increasing scaffold stiffness could lead to a potential decrease in porosity and permeability, which prevents the neo-tissue from proper ingrowth to the bulk of scaffolds. On the other hand, increasing scaffold porosity might lead to a higher permeability but the effective stiffness would be sacrificed. Moreover, the biomaterials should also be degradable upon implantation (with a temporary resistance to biodegradation upon implantation) at a rate matching that of the new matrix production by the developing tissue.

Bone is a natural complex porous composite with unique properties of remodelling to adapt its microstructure to external mechanical stress. Bone is also one of the tissues with the highest demand for tissue reconstruction or replacement. Cranial, maxillofacial, oral fractures and large bone defects are currently being treated by using auto- and allografts. These techniques have limitations in the clinical usage such as immune response, donor-site morbidity, and lack of availability[89-91]. Therefore, the interest on artificial tissue grafts were recently considered in order to overcome limitations of traditional allo- or autografts, such as risk of immune rejection and pathogen transfer, pain and infection, or limited availability [7, 92]. The overall aim of this study is to develop a much-needed autograft-bone-mimetic engineered graft as a substitute for allograft bone in reconstruction of large bone defects. Bioresorbable scaffolds, i.e. porous constructs,

seeded with the appropriate type of cells, should provide a template for tissue regeneration, while slowly resorbing, to finally leaving no foreign substances in the body, thus reducing the risk of inflammation. A three-dimensional (3D) internal geometry, similar to bone morphology, and the retention of mechanical properties after implantation are required for scaffolds in order to maintain a tissue space of prescribed size and shape for tissue formation.

The cortical bone is a hollow center dens shell composed of smaller units called osteons that have microtube like structures with a central vascular channel inside for ensuring suitable nutrient/waste transport to the bone tissue [93]. Laminated multilayers of CaP deposited collagen fibers forms the osteon microtubes. The extracellular matrix (ECM) of bone is a composite that primarily comprises hydroxyapatite (HA) (biological ceramics) embedded within a collagen matrix (biological polymers) and water (Figure 3.1 a). Carbonated HA Ca10(PO4)6(OH)2 accounts for approximately 70 % of the weight of bone. The inorganic component provides compressive stiffness to bone. Roughly one-third of the weight of bone is composed of the organic matter, which is primarily type I collagen and ground substance. Type I collagen fibres are elastic and flexible, and thus tolerate stretching, twisting, and bending. Therefore, biocompatible and biodegradable engineered scaffolds which can mimic both nano and microstructure of osteons in cortical bone tissue would be strong candidates for bone tissue engineering applications. Numerous methods have been developed and employed to fabricate 3D scaffolds for tissue engineering applications. Although the conventional fabrication techniques such as solvent casting, Freeze-drying and Gas foaming/supercritical fluid processinghave produced scaffolds used in tissue engineering of various types, most of them are

incapable of producing fully continuous interconnectivity and uniform pore morphology within a scaffold. Additionally, the pore size, pore geometry and spatial distribution cannot be precisely controlled in these conventional processes. One of the main limitations of most conventional fabrication methods is the need of an organic solvent to dissolve polymers and other chemicals, as well as the use of porogens to create pore structures. Most solvents and porogens are toxic, and their residues in the scaffold may cause severe inflammatory responses. Also, the physical configuration of the scaffolds, which mediate the cell-cell and cell-scaffold interactions, exerts strong influence on the success of osteogenesis processes in vitro [94, 95]. The success of engineered scaffold mostly depends on how closely the cell-scaffold interaction mimics that natural tissue *in vivo*. Both *in vitro* and *in vivo* studies have demonstrated that organic/inorganic composite fibrous scaffolds which can mimic nanostructure of natural bone, support attachment, differentiation, and proliferation of osteoblasts or mesenchymal stem cells (MSCs) and facilitate bone healing [96]. However, investigations regarding the effect of fibrous composite scaffolds such as osteon-mimetic tubular scaffolds with 3D morphology on osteogenic differentiation of MSCs are still limited. To this end, we hypothesized that three dimensional structure of microtubes with well-defined pores could potentially mimic the microstructure of osteons in cortical bone and induce osteogenesis of MSCs. In order to test this hypothesis, we investigated the osteogenic differentiation potential of MSCs when seeded into microtubes engineered from CaP deposited aligned nanofiber microsheets that have an array of macropores to enhance diffusion of nutrients. The microtube structure fabricated by wrapping CaP deposited nanofiber layers around the stainless steel needles upon annealing wrapped nanofiber

microsheets above glass transation temperature (T_g). The effect of tubular formation of CaP deposited microsheets on osteogenic differentiation of rat MSCs was investigated by cytochemical, and mRNA expression. Our results indicate that the 3D microtubes provide a promising microenvironment that enhances osteogenesis when compared to microsheet scaffolds.

2. Experimental

2.1. Fabrication of cortical-bone-mimetic scaffolds

CaP-nucleated microsheets (discussed in Chapter 2) were wrapped tightly around a 25 G needle between 10-30 times for form a microtube (Figure 3.1 b). Next, a set of the microtubes was packed around a stainless steel rod and the assembly was heated to a temperature above the T_g PLA (85°C) nanofibers to form a rigid, tough, osleoconduetive, cylindrical shell by fuse the microtubes. After cooling, the rod and microneedles (in the mierotubes) were removed to obtain a nanostructred cylindrical shell with Haversian-like microcanals (Figure 3.1 b). Then, an array of circular microholes was drilled by a scanning deep-ultraviolet laser micro-drilling system (Precision MicroFab) on the outside surface of the shell (500-1000 μm apart) traversing the shell thickness to generate Volkmann like microcanals. Microdrilling resulted in the formation of a shell with an interconnected network of microcanals to stimulate cell migration, vascularization, and bone formation within the shell wall after implantation.

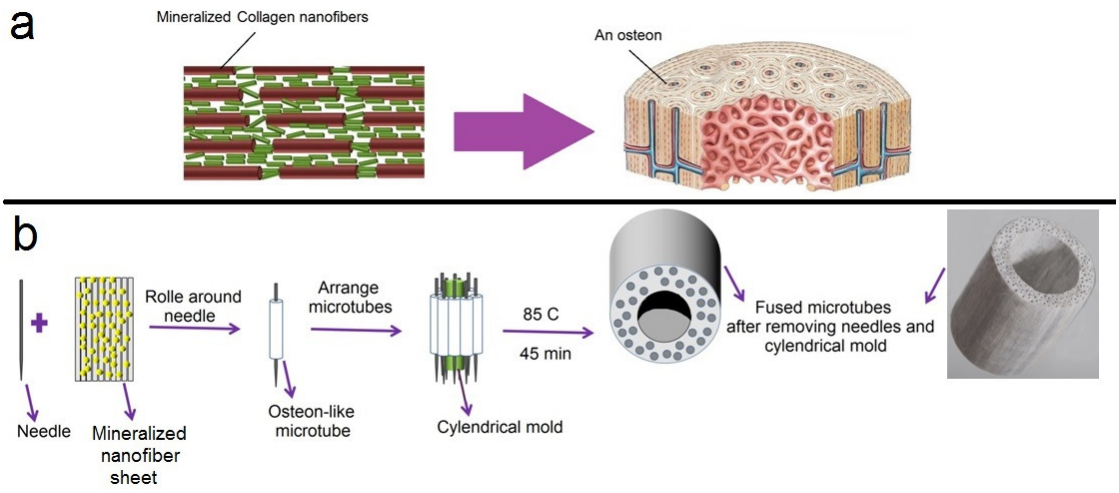

Figure 3.1. (a) Natural structure of bone tissue from micron to nano scale. (b) Steps for fabricating biodegradable, rigid, osteoinductive and osteoconductive shell.

2.2. Characterization of cortical-bone-mimetic scaffolds

The porosity and density of the CaP nucleated NF microsheets before and after heat treatment were calculated using Eq. (1) and Eq. (2). The thickness and size of the microsheets were measured using a micrometer caliper (VWR, Atlanta, GA).

$$\text{Apparent density (mg/mm}^3\text{)} = \frac{\text{microsheet mass (mg)}}{\text{thickness}\times\text{surface area (mm}^3\text{)}} \quad (1)$$

$$\text{Porosity (\%)} = 1 - \frac{\text{density of microsheet (mg/mm}^3\text{)}}{\text{density of PLA (mg/mm}^3\text{)}} \quad (2)$$

For determination of compressive modulus, the scaffolds were prepared with the overall thickness of 1 mm and diameter of 1 cm, was loaded on the Peltier plate of an AR2000 rheometer (TA Instruments, New Castle, DE) and subjected to a uniaxial compressive force at a displacement rate of 7.5 mm/s. The slope of the linear fit to the stress–strain curve for 5–10% strain was taken as the elastic modulus (E) of the mineralized matrix as we previously described [74]. For determination of mass loss, the

scaffolds were incubated in simulated body fluid (SBF) at 37ºC and under mild agitation. At each time point, samples were removed from SBF, washed three times with DI water and dried under vacuum. The dry sample weight was measured and compared with the initial dry weight to determine the fractional mass remaining as described [75].

3. Results and Discussion

Mineralization in osteons occurs under the function of glutamic-acid rich residues of bone sialoprotein and osteonectinon on hydroxyapatite nucleation [97, 98]. Therefore, peptides including polyglutamic acid sequences have been widely investigated to determine the interaction with nHA crystals. For example, Itoh et al. coated HA with the synthetic peptide (E_7PRGDT), and seeded osteoblastic cells onto the surface. They demonstrated that the amount of E_7PRGDT peptide containing polyglutamic acid sequence bound to HA was higher than passively adsorbed RGD at all coating concentrations due to high affinity of polyglutamic acid peptide to nHA crystals [99]. In addition, Sarvestani et al. treated the surface of nHA particles with glutamic acid peptide (Ac-Glu6). It was indicated that the average density of elastically active chains in the PLEOF network increased significantly when nHA in the network were treated with the osteonectin-derived Ac-Glu6 [100]. Similar to others, in our previous study, conjugation of glutamic acid template peptide on NF significantly increased the CaP nucleation (Karaman et al. in press). Thus, in this study we used the glutamic acid conjugated NF to nucleate the CaP crystals. 50 wt% CaP to fiber ratio (GLU-NF/CaP50) was used to fabricate the osteon-mimetic microtubes. The micro-tubuler structure of the biofabricated scaffolds ideally mimics the osteons structures of bone tissue [101].

The effects of the heat treatment on nanofiber microsheets based on CaP to NF weight ratio porosity and density are shown in Figure 3.2 a and b, respectively. The results indicated that the porosity of the CaP nucleated microsheets after heating decreased significantly for all the test groups. In addition, the appeareant density of different CaP containing GLU-NF microsheets was increased significantly for each test group after heat treatment.

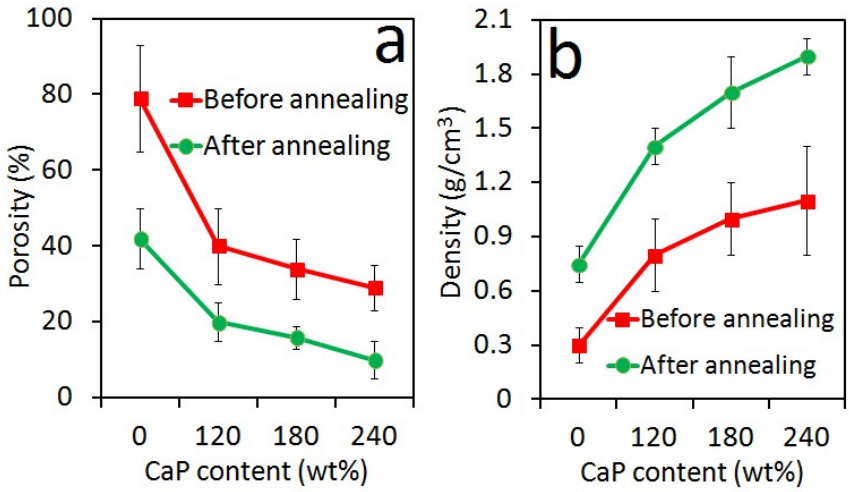

Figure 3.2. The effect of heat treatment on porosity(a) and density(b) of microsheets

The compressive modulus and strength of the shell was a strong function of the CaP content of the microsheels (Figures 3.3 a and b). The compressive modulus and strength of the shell with 240% CaP content were 2.5 GPa and 150 MPa (Figure 3.3 a and b), respectively, which was in the range of natural compact bone [102, 103]. The degradation of the engineered shell was inversely related to CaP content (Figure 3.3 c). The shell with 240% CaP content had <5% mass loss after 120 days of incubation in SBF, thus the shell can potentially provide rigidity during the callus formation stage of bone formation [104].

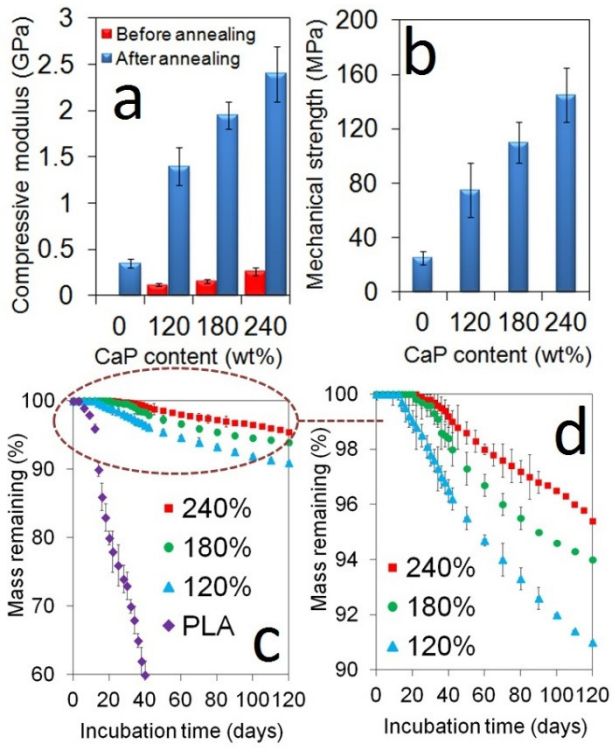

Figure 3.3. Compressive modulus (a) and strength (b) of the shell as a function of CaP content, (c) Mass loss of the shell with incubation time in SBF for CaP contents of 0, 120, 180 and 240%. (d) Magnification of mass remaining results for 120, 180 and 240%.

Also, the compressive modulus of microsheets before and after heat treatment is compared in Figure 3.3 a. The heat treatment significantly increased the compressive modulus of the CaP nucleated NF microsheets. For example, the compressive modulus of 120 wt% CaP microsheets increased from 0.12±0.02 GPa to 1.4±0.2 GPa. And that of 240 wt% increased from 0.26±0.04 GPa to 2.4±0.3 GPa after heat treatment. These results indicated that the stiffness of microsheets was increased by heat-shrinking the microsheets. Similar with our results, it has been reported that with the increasing of apatite amount in nanofibrous microsheets, the tensile modulus of the microsheets increases significantly [105]. In addition, incorporation of nHA crystals in polycaprolactone fibers increases the tensile modulus of fabricated electrospun NF [106]. Overall, nCaP deposited NFs have the potential to provide higher structural support to progenitor cells

compared to NF with no CaP content. It has been observed that increasing mineral content on NF significantly enhanced MSCs adhesion and differentiation[107].

The limitation of nanofibers fabrication with electrospinning is that it produces a relatively two dimensional fibrous scaffolds. In addition, the pore sizes are relatively smaller which does not allow cells to penetrate into the scaffold [108]. Therefore, a rigid, resorbable, and osteoconductive shell with similar microstructure to cortical bone including interconnected network of microcanals to provide the mechanical stability needed for large bone fracture was designed in this study. Figure 3.4 shows the SEM images of different inner diameter microtubes made by 240 wt% CaP coated NF sheets.

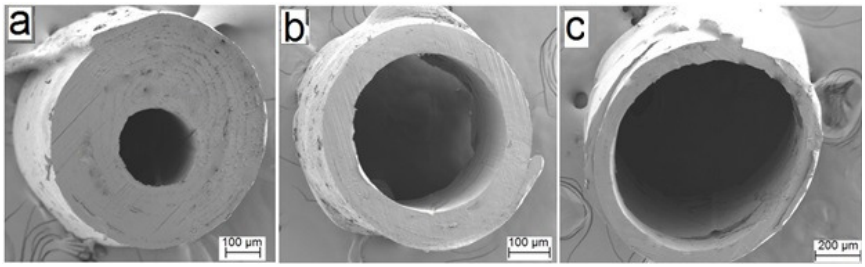

Figure 3.4. SEM images of different inner diameter microtubes 250 µm (a), 450 µm (b), and 800 µm (c).

Figure 3.5 shows a hollow center annealed scaffold containg 180 nucleated microtubes with 240 wt% CaP content. It can be observed in figures 3.5 a and b that this biofabrication technique results in formation of dens shell-like structure including several microchannels which mimics that of natural cortical bone (see natural cortical bone structure in figures 1.2 and 3.1). Additionally, the microholes on the surface of scaffold can eb clearly seen in figure 3.5 c. The presence of these microholes can be resulted in

the formation of a shell with an interconnected network of microcanals to stimulate cell migration, vascularization, and bone formation within the shell wall alter implantation.

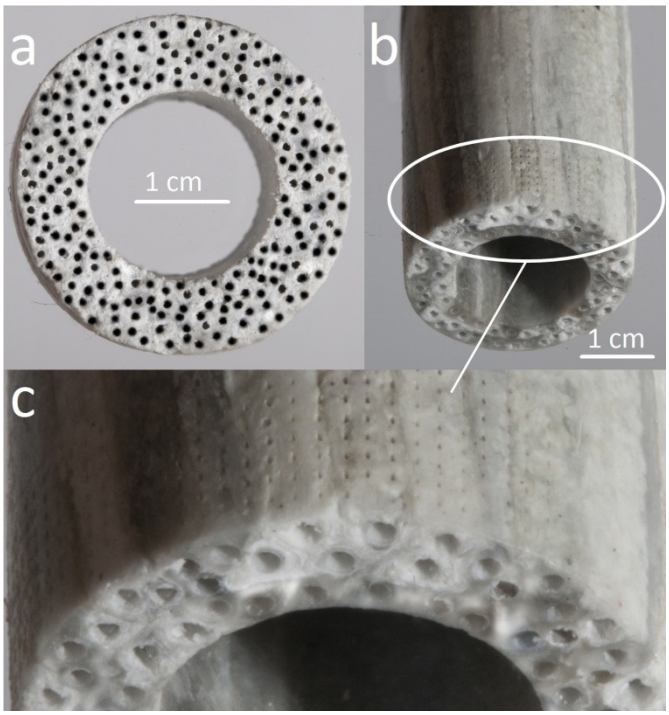

Figure 3.5. A cortical bone-mimetic scaffold made by 180 microtubes. (a) Top view of the cross section of scaffold. (b) Side view of scaffold including the microholes. (c) Magnification of microholes in the scaffold.

It has been reported that it takes 12 weeks for newly formed callus to become load-bearing as patients [104] undergoing alveolar bone reconstruction wait minimum of 12 weeks for bone to form on the regenerating membrane prior to tooth implantation [109]. The engineered shell should resorb and transfer load to the newly formed bone to reduce stress-shielding after 24 weeks [110]. The natural dense bone has <15% porosity [111]), CaP to collagen fiber ratio of 200- 300% [52], compressive modulus and strength of 5 GPa and 90- 170 MPa, respectively [102, 103]. Therefore, success is defined by <5% resorption of the engineered shell after 12 weeks, >75% resorption after 24 weeks, with initial and 12-

weeks compressive strength of 150 MPa and 100 MPa, respectively. The product is an engineered, rigid, and resorbable shell with interconnected canals to allow vascularization and bone formation from within the shell wall.

4. Conclusion

In this study, our objective was to investigate the fabrication a 3D formation of microtubes acffold. The novel aspect of this work is the synthesis of a cortical-bone-mimetic shell with Haversian-/Volkmann-like canals for nutrient and oxygen supply to the migrating cells inside the shell. In this aim, aligned, functionalized. nanotmermicrosheets were nucleated with CaP naocrystals. Then the sheets were wrapped into microtubes, a set of mierotubes were fused to from a shell. Microhdles were drilled on the shell surface to form an interconnected network of canals for nutrient and oxygen supply. The shells will be evaluated with respect tq strength, resorption, and osteogenesis. The target compressive strength is 150 MPa, mass loss of <5% after 12 weeks and >75% after 24 weeks. Present findings demonstrate that the 3D structure of microrubular scaffolds provide a promising microenvironment that enhances osteogenesis compared to 2D microsheet scaffolds.

CHAPTER 4: FABRICATION OF RESORBABLE, SELF-ASSEMBLED, POLYETHYLENE GLYCOL BASED NANOGELS FOR CONTROLLED RELEASE OF GROWTH FACTORS [1]

1. Introduction

Bone morphogenetic proteins (BMPs) are the most abundant osteoinductive proteins which regulate the differentiation and function of cells involved in osteogenesis [112]. Specifically, it has been proved that BMP-2 is present in different steps of bone healing, from the initial stages of bone regeneration as well as during later phases including osteogenesis and chondrogenesis [113, 114]. Vascular endothelial growth factor (VEGF) as a widely used angiogenic growth factor in regenerative medicine plays a key regulatory role in up-regulation of angiogenesis by signaling vascular endothelial cells to undergo proliferation, migration, and differentiation into new blood vessels [115]. VEGF's normal function is to create new blood vessels during embryonic development, new blood vessels after injury, muscle following exercise, and new vessels (collateral circulation) to bypass blocked vessels.

---

[1] Barati, D., et al., Spatiotemporal release of BMP-2 and VEGF enhances osteogenic and vasculogenic differentiation of human mesenchymal stem cells and endothelial colony-forming cells co-encapsulated in a patterned hydrogel. Controlled Release, 2016. 223: p. 126-136.

Therefore, an alternative approach like developing biocompatible carriers is necessary to control both the location and rate of growth factors delivery at the defect site. PLGA micro- and nanoparticles due to their wide range of degradation times are used for immobilization and timed-release of BMP2 and VEGF [118-121]. However, protein denaturation by surface adsorption and acidic degradation products of PLGA can significantly reduce protein bioactivity [122, 123]. Due to the hydrophilicity and chain flexibility of polyethylene glycol (PEG), PEGylation is used to increase stability of PLGA nanoparticles in aqueous suspensions, enhance stability of the grafted protein, and reduce particle phagocytosis [118, 120, 124-126]. In this work, PEG macromers chain-extended with short lactide (L) and glycolide (G) segments were used to form nanogels (NGs) for grafting and timed-release of BMP2 and VEGF proteins. In the chain-extended macromer, the PEG block imparted stability to NGs in aqueous solution, L segment led to self-assembly and NG formation, and G segment controlled NG degradation and protein release. We have previously shown that PEG macromers chain-extended with short L/G segments form micellar structures in aqueous solution [127]. Here, the effect of PEG molecular weight (MW) and L/G segment length on degradation and protein release kinetics of the NGs have been investigated.

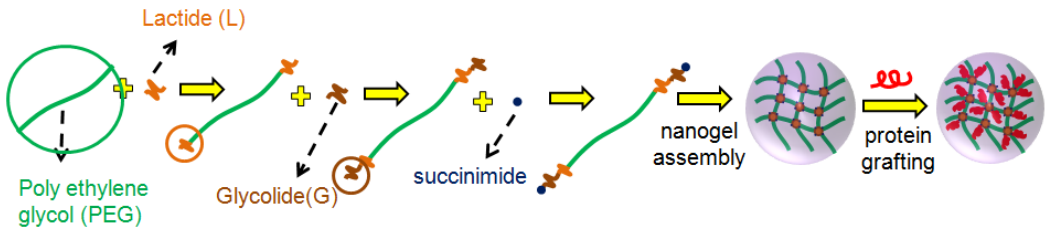

Figure 4.1. Synthesis of PEG macromers chain-extended with short lactide (L) and glycolide (G) segments to form nanogels (NGs) for grafting and timed-release of BMP2 and VEGF proteins

2. Experimental

2.1. Synthesis and functionalization of PEG-LG block copolymer

The PEG-LG block copolymers were synthesized by melt ring-opening polymerization with successive addition of L and G monomers to the reaction using PEG as the initiator and TOC as the catalyst. PEG and lactide were added to a reaction flask equipped with a stirrer and immersed in an oil bath in a molar ratio based on the desired L segment length (Table 4). Next, the flask was heated to 120°C under nitrogen flow and maintained at that temperature for 1 h to remove residual moisture. Then, TOC catalyst was added to the mixture at 120°C and the reaction was allowed to proceed for 6 h at 140°C. The lactide chain-extended PEG macromer was used as an initiator for chain extension with G monomer with a predetermined L to G ratio (Table 1). The reaction was allowed to proceed for 6 h at 140°C and the product was precipitated in ice-cold hexane to remove the unreacted monomers. The synthesized copolymer was functionalized with succinimide groups by reacting hydroxyl end-groups of the copolymer with DSC as we described previously [128]. The product was purified by dialysis against DI water and lyophilized. The chemical structure of the synthesized copolymer was characterized by a

Varian Mercury-300 ^{1}H-NMR (Varian, Palo Alto, CA) as we previously described [129]. The synthesized macromers are hereafter referred to as PaLGb-Lc (Tables 1 and 2) where the lowercase letter "a" is the PEG MW in kDa, "b" is LG to PEG molar ratio, and "c" is the mole fraction of lactide in LG segments. The shorter abbreviations P4-I,II,III, P8-I,II,III, and P12-I,II,III stand for those macromers based on 4, 8, and 12 kDa PEG MW, respectively.

2.2. Nanogel formation and protein grafting

PaLGb-Lc macromer was dissolved in DMSO and self-assembled to form NGs by dialysis (3.5 kDa MW cutoff) against PBS for 8 h as we previously described [118]. For BMP2 or VEGF grafting, 10 mg NGs was suspended in 0.5 mL PBS by sonication for 1 min. Next, 0.5 mL of the protein in PBS (20 mg/mL for BSA, 800 ng/mL for BMP2 and VEGF) was added to the NG suspension. The amine group of the protein was allowed to react with succinimide end-groups of PaLGb-Lc in NGs under ambient conditions for 12 h as we previously described (Figure 4.1) [119]. The protein grafted NGs were freeze-dried to obtain a free flowing powder. To determine grafting efficiency, the protein grafted NGs were resuspended in PBS and centrifuged at 18,000 rcf for 10 min and the supernatant was analyzed for total protein content with the ninhydrin reagent as we described previously [130]. Grafting efficiency was determined by dividing the amount of attached protein (total - free protein) by the initial amount in the grafting reaction.

Size distribution of the NGs was measured by dynamic light scattering with a Submicron Particle Sizer (Model 370, NICOMP, Santa Barbara, CA) as we described previously [119]. Polydispersity (PD) of the NGs was determined using the equation PD = $\Delta d / \langle d \rangle$ where Δd and $\langle d \rangle$ are the standard deviation and mean size of the NGs,

respectively [131, 132]. Zeta potential of the NGs was measured with a ZetaPlus analyzer (Brookhaven Instruments, Holtsville, NY) with a particle concentration of 2.5 mg/mL at 25°C in PBS [133]. NGs degradation kinetic was measured by incubation in PBS at 37°C as we described previously [118]. The fractional mass remaining was determined by dividing the dried mass at time t by the initial mass. For measurement of release kinetic, 1 mg protein grafted NGs were incubated in 1 mL PBS at 37°C as we previously described [118]. At each time point, the suspension was centrifuged at 18350 rcf for 10 min, the supernatant was removed, the NGs were resuspended in 1 mL fresh PBS and incubated until the next time point. The amount of BSA in the supernatant was measured with the ninhydrin reagent as described [130]. In the case of BMP2 and VEGF-grafted NGs, the protein concentration in the supernatant was measured by ELISA as we described previously [118].

3. Results

3.1. Macromer characterization

The average number of L/G units per PaLGb-Lc was calculated from ^{1}H-NMR spectra of the macromer. Two chemical shifts with peak positions at 1.6 and 5.2 ppm, two at 3.6 and 4.2 ppm and one at 4.8 ppm were attributed to the methyl and methine hydrogens of lactide, the methylene hydrogens of PEG and the methylene hydrogens of glycolide, respectively [128, 134]. The chemical shift with peak position at 2.77 ppm was related to the methylene hydrogens of succinimide end-groups. The average segment length of L and G units per macromer and the number-average MW ($\overline{M_n}$) of the

macromers are shown in Table 4. The number of L and G units per macromer ranged 2.3-8.9 and 0.9-5.7, respectively.

3.2. Characterization of nanogels

Size distribution of P4, P8, and P12 NGs and their corresponding SEM images are shown in Figures 4.3a to c, respectively. In general, mean size of the NGs was <200 nm. Mean size, PD, and zeta potential of the NGs are given in Table 5. Mean size ranged from 120±6 to 140±13 nm for P4 NGs, 150±11 to 160±17 nm for P8 NGs, and 170±12 to 190±15 nm for P12 NGs, respectively.

Table 4.1. Number average molecular weight (M_n), LG to PEG feed ratio, average number of L and G segments per macromer for PaLGb-Lc macromers.

Group	Macromer type	M_n (±100)	LG/PEG(L/G) feed molar ratio	L/end group (±0.1)	G/end group (±0.1)
P4-I	P_4LG8-L75	5100	12 (75/25)	3.1	0.9
P4-II	P_4LG8-L60	5100	12 (60/40)	2.5	1.5
P4-III	P_4LG8-L50	5200	12 (50/50)	2.2	2.1
P8-I	P_8LG16-L75	10300	20 (75/25)	6.4	2.0
P8-II	P_8LG16-L60	10100	20 (60/40)	4.6	3.1
P8-III	P_8LG16-L50	10000	20 (50/50)	3.8	4.0
P12-I	P_{12}LG24-L75	15200	30 (75/25)	8.9	2.6
P12-II	P_{12}LG24-L60	15000	30 (60/40)	6.7	4.4
P12-III	P_{12}LG24-L50	14900	30 (50/50)	5.3	5.7

The NGs were relatively monodisperse with PD<0.2 and the mean NG size increased with decreasing lactide fraction. All NGs were negatively charged with zeta potential between -23 and -15 mV. The absolute value of the zeta potential increased with increasing PEG molecular weight while the lactide fraction did not significantly affect zeta potential.

Degradation of the NGs with incubation time was biphasic with an initial fast rate followed by a slow rate (Figure 4.2 a-c). Degradation rate increased with decreasing L:G ratio for all NGs. Mass loss of P4 and P8 NGs after 24 days incubation increased from 50±5 to 65±3% and 60±8 to 85±2%, respectively, as the L:G ratio decreased from 75:25 to 50:50. P12-I, P12-II and P12-III NGs degraded after 12, 16, and 18 days, respectively.

Table 4.2. Mean size, polydispersity (PD) and zeta potential of NGs formed by PaLGb-Lc macromers. Error bars correspond to means ± 1 SD for n=3.

Group	NP type	Mean size(nm)	PD	Zeta potential (mv)
P4-I	P_4LG8-L75	118±6	0.17±0.04	–15.9±1.9
P4-II	P_4LG8-L60	127±10	0.15±0.03	–15.3±1.9
P4-III	P_4LG8-L50	140±13	0.08±0.01	–14.8±1.3
P8-I	P_8LG16-L75	141±11	0.15±0.04	–18.6±1.3
P8-II	P_8LG16-L60	158±13	0.08±0.01	–17.7±1.7
P8-III	P_8LG16-L50	167±17	0.07±0.02	–18.5±1.8
P12-I	P_{12}LG24-L75	165±12	0.07±0.01	–22.9±1.7
P12-II	P_{12}LG24-L60	178±15	0.10±0.02	–22.3±2.0
P12-III	P_{12}LG24-L50	190±15	0.11±0.01	–21.8±1.5

P4-I NGs had the slowest degradation with 50±5% mass loss after 30 days and P12-III NGs had the fastest degradation with >95% mass loss after 12 days. The release kinetic of BSA from the NGs in PBS was biphasic with an initial fast rate followed by a slow rate (Figure 4.3 d-f), consistent with NGs degradation. The release of BSA increased with decreasing L:G ratio for all NGs. The average BSA release rate of P4, P8, and P12 NGs increased from 2 to 4.2%/day, 4 to 6.3%/day, and 5.7 to 9.7%/day, respectively, as L:G ratio decreased from 75:25 to 50:50. P4-I had the slowest BSA release with 45±8% in 24 days and P12-III had the fastest with >95% released in 12 days.

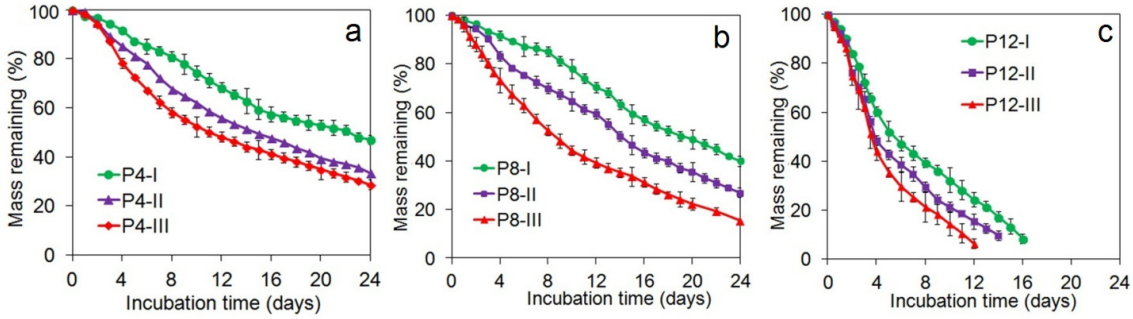

Figure 4.2. Effect of PEG MW, LG segment length, and L/G ratio in PaLGb-Lc macromer on NG mass loss in PBS with incubation time. The abbreviations P4, P8, and P12 represent NGs made from macromers with PEG MW=4, 8, and 12 kDa and average LG segment length of 8. The

The extent of bone formation *in vivo* depends on the duration of BMP2 exposure to MSCs in the first four weeks [135, 136] whereas vascularization depends on VEGF exposure to endothelial progenitor cells within the first week [137]. Figure 4.3 g represents the release rate of BMP2 and VEGF encapsulated inside SPELA and GelMA hydrogels, respectively, compared to BMP2 and VEGF grafted to NGs(21) and NG(10), respectively. It can be observed that the encapsulated BMP2 and VEGF were completely released from hydrogels in less than 40 hours while the ones attached to NG(21) and NG(10) were released steadily after 3 weeks and 7 days, respectively. Therefore, NGs with steady release for 3 weeks and 71±3 wt% bioactivity (P8-1 NGs) were used for BMP2 grafting; NGs with steady release for 7 days with 80±5 wt% bioactivity (P12-II NGs) were used for VEGF (Figure 4.3 g).

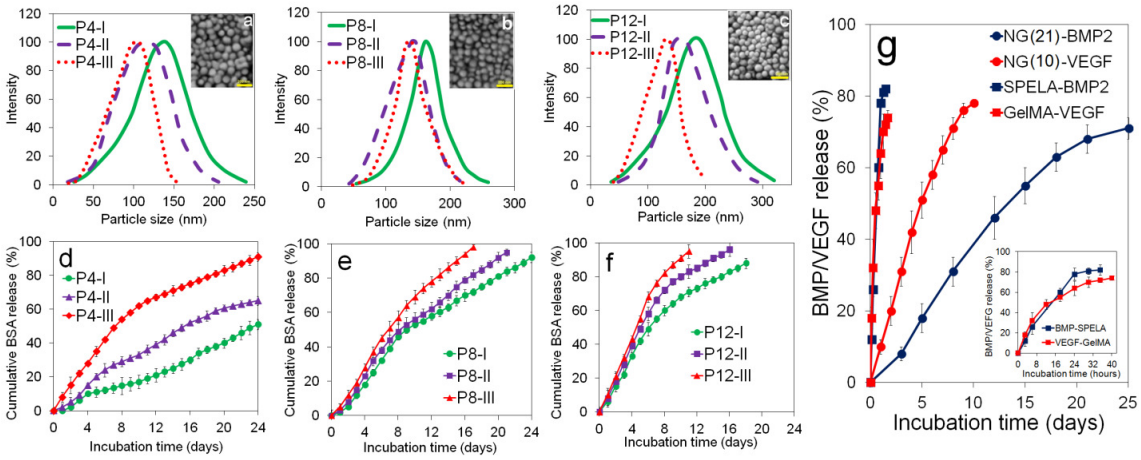

Figure 4.3. Effect of PEG MW, LG segment length, and L/G ratio in PaLGb-Lc macromer on NG size distribution (a-c), and cumulative BSA release (d-f) in PBS with incubation time. Release kinetic of BMP2 encapsulated in SEPLA and VEGF encapsulated in GelMA hydrogel compared to release kinetic of BMP2 grafted to NGs and VEGF grafted to NGs. The abbreviations P4, P8, and P12 represent NGs made from macromers with PEG MW=4, 8, and 12 kDa and average LG segment length of 8. The abbreviations P4-I, P4-II, and P4-III represent NGs made from 4 kDa MW PEG macromers with 75%, 60%, and 50% lactide in the LG segments, respectively. The numbers in abbreviations NG(21) and NG(10) represent the release time of grafted proteins on each type of NG. Morphology of the dried NGs is shown in the inset SEM images in (a-c). Error bars correspond to means ± 1 SD for n=3.

4. Discussion

Size distribution of nanoparticles self-assembled from PEG-LG macromers depends on the rate of particle assembly which in turn is related to the length of hydrophobic LG segments [138]. We previously generated nanoparticles (NPs) by self-assembly of ultra-low molecular weight ULMW-PLGA (1-2 kDa MW) with amphiphilic copolymers of PEG (3.4 kDa) and ULMW-PLA (PLEOF). The resulting NPs had mean sizes in the 200-300 nm range and relatively wide size distributions from 100 to 600 nm [118]. In this work, we used a different approach to generate PEG-LG macromers by extension of PEG chain-ends with a short L segment followed with a short G segment. The average length of the L segments was 5-10 (Table 4, note two ends per chain) while it was 15-30 in the

previous approach with ULMW-PLAF/PLEOF [118]. The relatively shorter hydrophobic segments in PaLGb-Lc led to the formation of hydrophilic NGs with mean sizes as low as 120 nm and size distributions as narrow as 25-150 nm. The more hydrophobic L segment in PaLGb-Lc controlled NGs assembly whereas the less hydrophobic G segment controlled NGs degradation.

As the PEG MW was increased from 4 to 8 and 12 kDa in P4-I, P8-I and P12-I, the L segment length had to be increased from 2.3 to 3.8 and 5.4, respectively, to induce self-assembly for the macromer with 50/50 L/G ratio (Table 4). As the L segment length in P4-I, P8-I and P12-I increased, mean NG size increased from 118±6 nm to 141±11 and 165±12 nm (Table 3), respectively. Length of the PEG block regulated the extent of association between the macromers by balancing van der Waals and dipolar interactions to prevent aggregation of hydrophobic LG segments [139]. The measured NG sizes in Table 5 are consistent with the previously reported increase in the average diameter of PLA-PEG nanoparticles from 30 to 60 nm with increasing PLA block MW from 3 to 30 kDa [140]. The measured zeta potentials of the NGs (-15 to -22 mv) was significantly less than the reported values for PLA or PLGA nanoparticles (~ -50 mv) [141] which was attributed to the negatively-charged carboxyl end-groups of PEG and their higher fraction in the NGs corona at higher PEG MWs [139].

It has been shown by us and others that the degradation kinetic of PEG-LG based micelles depends on the proximity of water molecules to L and G ester groups [127, 142], which is dependent on PEG MW and hydrophobicity of the degradable units [143, 144]. Consequently, PEG MW had the greatest effect on NGs degradation followed by the fraction of less hydrophobic G in LG segments (Figure 4.3 d-f). Release kinetic of BSA

grafted to the NGs followed the degradation of NGs (Figure 4.3 g-i). P4-III, P8-III, and P12-III NGs (50% G) with PEG MW of 4, 8, and 12 kDa lost 52, 61, and 94% mass after 12 days, respectively; those NGs released 67, 78, and 95% of the grafted BSA after 12 days. P8-I, P8-II, and P8-III NGs ((PEG MW 8kDa) with 25, 40, and 50% G in LG segments lost 30, 41, and 61% mass after 12 days incubation, respectively, those NGs released 58%, 62%, and 78% of the grafted BSA after 12 days.

5. Conclusion

Fabrication and characterization of resorbable NGs based on self-assembly of PEG macromers chain-extended with short L and G segments were investigated. It was shown that the NGs properties can be controlled by changing the molecular weight of PEG and ratio of L to G. For example, it was observed that degradation rate and protein release of the NGs increased with decreasing L to G ratio for the same PEG molecular weight. Therefore, these NGs can be potentially used as a carrier for temporal controlled release of different types of growth factors for different purposes.

CHAPTER 5: EVALUATING THE EXTENT OF VASCULOGENESIS AND OSTEOGENESIS STEM CELLS ENCAPSULATED IN A PATTERNED HYDROGEL WITH SPATIOTEMPORAL RELEASE OF BMP2 AND VEGF.

1. Introduction

The reconstruction of large bone defects with implanted scaffolds due to resection of tumors, skeletal trauma, or infection remains a significant clinical problem [145]. The high clinical failure rates with allografts and implanted scaffolds are attributed to insufficient vascularization and slow bone regeneration [146]. Engineered matrices that can guide concerted differentiation of multiple cell types to both vasculogenic and osteogenic lineages are promising for the treatment of large bone defects. In that regard, natural and synthetic matrices loaded with bone morphogenetic proteins (BMPs), with or without mesenchymal stem cells (MSCs), have been used extensively as a graft to accelerate bone repair and healing [147]. Among BMPs, *recombinant human* BMP-2 (hereafter referred to as BMP2) is used as a potent osteogenic factor in certain clinical applications including spine fusion and alveolar ridge augmentation [148]. Similarly, the widely used vascular endothelial growth factor (VEGF) is not only involved in angiogenesis, but also implicated in maturation of osteoblasts, ossification, and bone turnover [115, 149]. As the bioactivity of BMP2 and VEGF is concentration and time-dependent [135-137], their sustained delivery from biodegradable particulate systems has been investigated [118, 120 .

Osteogenesis and vascularization during bone development and growth are coupled processes [149, 153]. VEGF plays a key role in blood vessel invasion into hypertrophic cartilage as the endothelial cells in the invading vessels secrete growth factors that stimulate osteogenesis [149, 154]. There is a close correlation between vascularization and bone formation in endochondral ossification as maximum extent of bone formation follows maximum levels of VEGF expression [155]. In the bone marrow, endothelial progenitor cells form an osteoblast-vascular niche by close proximity to osteoprogenitor cells in the endosteum [156]. Hence, several studies have investigated the combined effect of BMP2 and VEGF on osteogenic and vasculogenic differentiation of MSCs and endothelial progenitor cells (EPCs).

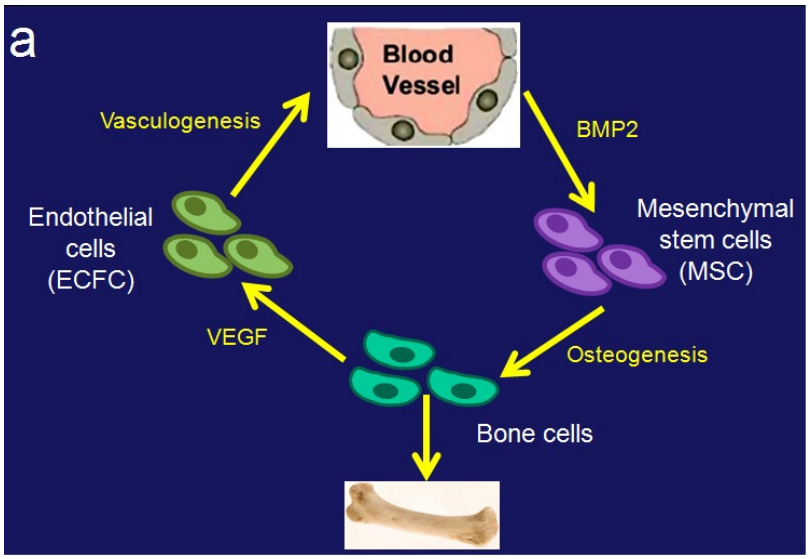

Figure 5.1. Vasculogenesis and osteogenesis are tightly coupled processes during bone formation

In one study [157], the extent of osteogenic differentiation of rat MSCs co-expressing BMP2 and VEGF in 2D culture was lower than MSCs expressing only BMP2. In another

study [158], in which MSCs in combination with EPCs were seeded in a calcium sulfate/alginate scaffold, the extent of osteogenic and vasculogenic differentiation of MSC+EPC group *in vitro* and *in vivo* (bone formation and blood vessel density) was significantly higher than the groups with only MSCs or EPCs. Furthermore in that study, the MSC+EPC group had higher extent of mineralization and vascularization than the group with BMP2-expressing MSCs. These previous studies indicate that EPCs not only take part in vascularization but they also enhance osteogenesis in combination with MSCs [159].

There is conflicting reports on the effect of VEGF and its combination with BMP2 on the extent of bone formation *in vivo* [160-162]. In an *in vivo* study [161], BMP2-expressing MSCs in combination with VEGF-expressing EPCs encapsulated in an alginate gel showed higher extent of bone formation after intramuscular implantation compared to the alginate gel with MSCs and VEGF-expressing EPCs. Further, VEGF-expressing EPCs hindered terminal differentiation of MSCs in co-cultures of EPCs+MSCs [161]. In an *in vivo* study in rat cranium [162], dual delivery of BMP2 and VEGF from gelatin nanoparticles embedded in a porous scaffold increased bone formation after 4 weeks implantation, but not after 12 weeks, compared to the delivery of BMP2 only. In addition, in an *in vivo* study in canine ulna [160], the extent of bone formation in a calcium phosphate scaffold, embedded with BMP2 and VEGF in poly(lactide-co-glycolide) (PLGA) nanoparticles, was independent of VEGF. Also, in an *in vivo* study in rat, dual delivery of VEGF from a gelatin hydrogel surrounding a solid matrix embedded with BMP2-encapsulated PLGA microspheres had no effect on bone formation in an orthotopic site compared to BMP2 alone [163]. However, dual and sustained delivery of BMP2 and VEGF enhanced bone

formation in an ectopic site [163] where MSCs and EPCs can potentially migrate from the surrounding tissue to the site of regeneration.

The previous studies suggest that dual BMP2 and VEGF delivery is effective in the presence of both MSCs and EPCs. Further, the addition of VEGF seems to retard maturation of MSCs to osteoblasts. This suggests that osteogenesis and vascularization may be coupled by spatiotemporal regulation of paracrine signaling in which the invading vascular endothelial cells secrete osteogenic morphogens to stimulate MSC differentiation and bone formation [164].

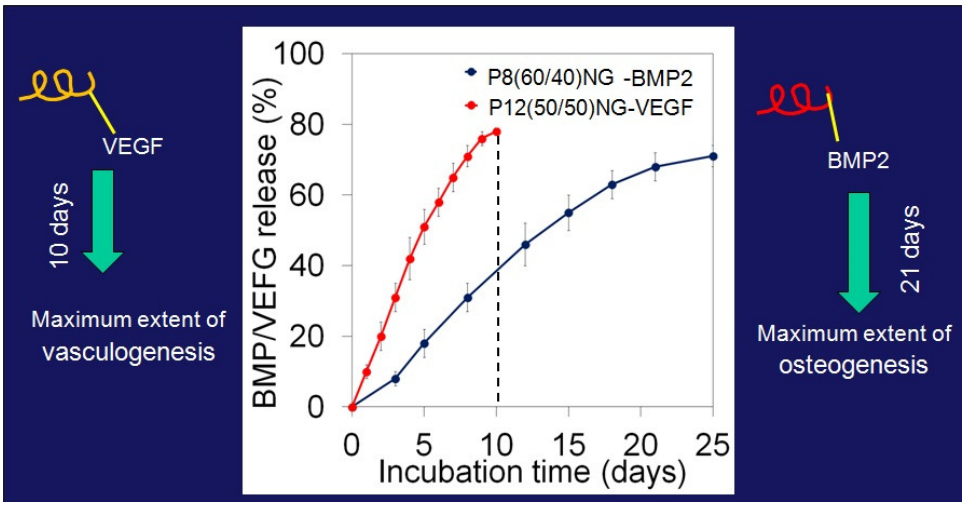

Figure 5.2. Dual delivery of BMP2 and VEGF in 21 and 10 days, respectively.

We hypothesized that osteogenesis and vascularization are coupled by the spatial and temporal expression of morphogens secreted by the differentiating MSCs and invading vascular endothelial cells. In this work, we test the hypothesis in vitro with human MSCs (hMSCs) and human colony-forming endothelial cells (ECFCs) encapsulated in a patterned hydrogel with spatiotemporal release of BMP2 and VEGF. Microchannels were generated in lactide-chain-extended star polyethylene glycol (SPELA) hydrogel. hMSCs

and BMP2-grafted NGs (BMP2-NGs) were encapsulated in the SPELA hydrogel. The microchannels were injected with a suspension of ECFCs+hMSCs and VEGF-grafted NGs (VEGF-NGs) in gelatin methacryloyl (GelMA) and crosslinked. The hydrogel constructs were cultured in vasculogenic/osteogenic medium (without VEGF or BMP2) and characterized with respect to the extent of osteogenic/vasculogenic differentiation of hMSCs and ECFCs.

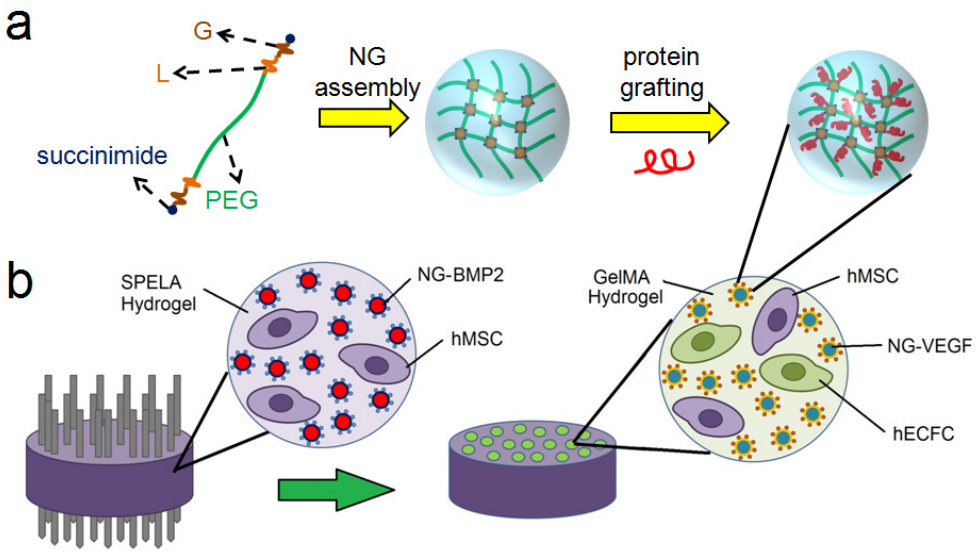

Figure 5.3. (a) Schematic diagram for NG assembly and protein grafting. The diagram is for illustration of protein grafting to NGS and is not intended to show the actual nanostructure of the NGs. (b) Schematic diagram of vasculogenic GelMA microchannels in osteogenic SPELA gel for patterned constructs. The SPELA precursor solution loaded with hMSCs and NG-BMP2 was injected inside a Teflon cylinder (5 mm diameter and 3 mm height) fitted with 12 needles spaced 500 µm apart. After gelation, the needles were removed and the GelMA precursor solution loaded with ECFCs+hMSCs and NG-VEGF was injected in the microchannels and UV crosslinked. After gelation, the cell-encapsulated construct was incubated in vasculogenic medium (without VEGF) for the first week, 50:50 mixture of vasculogenic and osteogenic medium (without VEGF, BMP2, and DEX) for three days (days 8-10), and finally in osteogenic medium (without DEX and BMP2, days 11-21).

2. Experimental

2.1. Encapsulation and differentiation of hMSCs and ECFCs in the un-patterned constructs

For the un-pattarned osteogenic constructs, hMSCs and BMP2-NGs were encapsulated in SPELA hydrogel and cultured in osteogenic medium without DEX and BMP2 (basal medium plus 50 μg/mL AA and 10 mM βGP). Osteogenic constructs included hMSCs in SPELA gel without BMP2, with dissolved BMP2, and BMP2-NGs. Briefly, 20 mg of BMP2-NGs (1.2 μg BMP2) were suspended in 1 mL of SPELA gel precursor solution [200 mg SEPLA macromer, 4 mg Ac-GRGD (2 wt% of macromer) for cell adhesion, and 7.5 mg (0.75 wt%) photo-initiator (Irgacure-2959, CIBA)] and the suspension was sterilized by filtration. Next, hMSCs at a density of $2x10^6$ cells/mL were suspended in the sterile SPELA precursor solution, injected between two sterile glass slides, and crosslinked by exposure to UV irradiation as we previously described [134]. For the un-patterned vasculogenic constructs, a 50:50 mixture of hMSCs+ECFCs [134] plus VEGF-NGs was encapsulated in GelMA hydrogel and cultured in EMB-2 BulletKit medium (Lonza) without the addition of VEGF. Vasculogenic constructs included hMSCs+ECFCs in GelMA hydrogel without VEGF, with dissolved VEGF, and VEGF-NGs. Briefly, 2 mg VEGF-NGs (120 ng VEGF) was suspended in 1 mL of GelMA precursor solution (50 mg GelMA and 7.5 mg photo-initiator) and sterilized. Next, 50:50 mixture of hMSCs+ECFCs at a total density of $2x10^6$ cells/mL was suspended in the sterile GelMA precursor solution, injected between glass slides, and crosslinked by UV irradiation as described [134]. After gelation, disk-shape gels (7 mm diameter and 0.5 mm thickness) were cut and incubated in PBS for 1 h with two PBS changes. Next, the media

was replaced with osteogenic (without DEX and BMP2) or vasculogenic (without VEGF) medium and incubated for 21 and 10 days, respectively.

2.2. Encapsulation and differentiation of hMSCs and ECFCs in the patterned constructs

Patterned hydrogels with GelMA micro-channels in a SPELA matrix were generated for osteogenic-vasculogenic co-culture experiments. Twelve 900-µm diameter needles (G-20) were inserted through the end-caps of a Teflon cylinder with diameter and height of 5 and 3 mm, respectively. The distance between the needles was 500 µm. Next, the sterile SPELA precursor solution (200 mg SPELA macromer, 4 mg Ac-GRGD, 7.5 mg photo-initiator, 20 mg BMP2-NGs, and $2x10^6$ hMSCs in 1 mL PBS) was injected between the needles and crosslinked with UV as described (Figure 5.3 b) [134]. Then, the needles were removed and the GelMA precursor solution (50 mg GelMA, 7.5 mg photo-initiator, 2 mg VEGF-NGs, and $2x10^6$ hMSCs/ECFCs in 1 mL PBS) were injected in the channels and crosslinked with UV as described (Figure 5.3 b) [134]. After gelation, the patterned constructs were washed with PBS and incubated in vasculogenic medium (without VEGF) for the first week, 50:50 mixture of vasculogenic and osteogenic medium (without VEGF, BMP2, and DEX) for the next three days (days 8 -10), and finally in osteogenic medium (without DEX and BMP2) for 11 days (days 11-21). Experimental groups included patterned constructs without BMP2/VEGF, BMP2 dissolved in SPELA gel plus VEGF in GelMA, and BMP2-NGs in SPELA gel plus VEGF-NGs in GelMA.

2.3. Characterization of cells behavior encapsulated in patterned and un-patterned hydrogels

Biochemical, mRNA, and protein analysis, alizarin red and Immunofluorescent staining techniques were used to characterized the extent of osteogenesis and vasculogenesis of cells in hydrogels.

3. Results

3.1. Osteogenic differentiation of hMSCs and ECFCs encapsulated in patterned hydrogels with BMP2 and VEGF NGs

DNA content, ALP activity, calcium content, and mRNA expression of osteogenic markers for ECFCs+hMSCs/NG-VEGF encapsulated in GelMA channels and hMSCs/NG-BMP2 encapsulated in SPELA matrix in the patterned constructs are shown in Figure 5.4 (blue curve). Controls included ECFCs+hMSCs in the channels and hMSCs in the matrix with (red curve, without NG grafting) and without (green curve) VEGF and BMP2 in the channels and matrix, respectively. Other controls included hMSCs/BMP2 (dashed pink) and hMSCs/NG-BMP2 (dashed light blue) in SPELA gel (no GelMA channels) and cultured in osteogenic medium (without DEX and BMP2) for 21 days. DNA content of the groups with BMP2/VEGF (with or without NG grafting) decreased significantly with time which was related to the differentiation of encapsulated cells, as we previously described [165] (Figure 5.4 a). ALP activity of hMSCs in un-patterned osteogenic constructs with BMP2 or BMP2-NGs (dashed curves) increased significantly from day 7 to 14, reached a maximum after 14 days and decreased from day 14 to 21 (Figure 5.4 b). The peak ALP activity of hMSCs in the patterned constructs with

BMP2/VEGF (with or without grafting) was delayed to day 18 because the constructs were cultured in vasculogenic medium in the first 7 days (Figure 5.4 b). The patterned constructs (solid lines) had higher ALP activity than their corresponding un-patterned osteogenic constructs (dashed lines). The patterned constructs with NG-BMP2/NG-VEGF (blue curve) and without BMP2/VEGF (green curve) had the highest and lowest ALP activity with 6100±500 and 2000±300 IU/mg DNA, respectively. Calcium content as a measure of the extent of mineralization for all groups steadily increased with incubation time (Figure 5.4 c). After 21 days incubation, the patterned constructs (solid lines) had higher calcium content than their corresponding un-patterned osteogenic constructs (dashed lines). The patterned constructs with NG-BMP2/NG-VEGF (blue curve) and without BMP2/VEGF (green curve) had the highest and lowest calcium content after 21 days with 710±50 and 220±30 mg/mg DNA, respectively (Figure 5.4 c).

mRNA expression of RUNX2 transcription factor initially increased with incubation time for all groups, peaked at day 14, and then decreased. The un-patterned osteogenic construct with NG-BMP2 and the patterned construct with NG-BMP2/NG-VEGF had the highest RUNX2 expression while the patterned construct without BMP2/VEGF had the lowest RUNX2 expression (Figure 5.4 d). Interestingly, RUNX2 expression of the patterned construct with NG-BMP2/NG-VEGF decreased slightly with incubation after day 14 (Figure 5.4 d). mRNA expression of ALP (Figure 5.4 e) followed a trend similar to that of ALP activity shown in Figure 5.4 b.

The patterned construct with NG-BMP2/NG-VEGF (blue curve) had highest ALP expression at day 14. mRNA expression for Col I for all groups increased steadily with incubation time (Figure 5.4 f). The un-patterned osteogenic construct with NG-BMP2

and the patterned construct with NG-BMP2/NG-VEGF had the highest Col I expression after 21 days incubation.

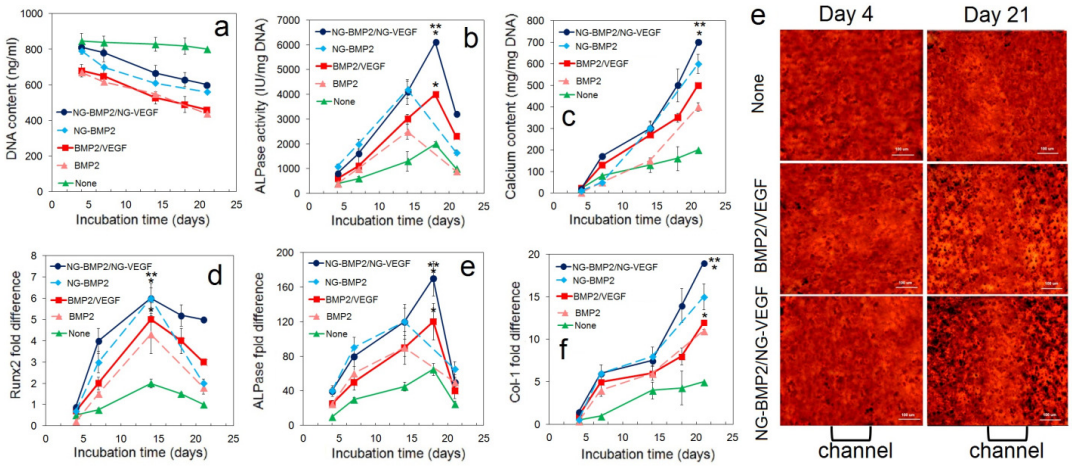

Figure 5.4. DNA content (a), ALP activity (b), calcium content (c), and mRNA expression of osteogenic markers Runx2 (d), ALP (e), and Col I (f) for hMSCs and ECFCs in the patterned constructs. Groups included patterned constructs without VEGF/BMP2 (green), with VEGF/BMP2 (red), and with NG-VEGF/NG-BMP2 (blue); un-patterned constructs with NG-BMP2 (dashed light blue) and with BMP2 (dashed pink). Patterned constructs were incubated in vasculogenic medium for 7 days, vasculogenic/osteogenic medium for 3 days, and osteogenic medium for 11 days (without VEGF, BMP2, and DEX). Un-patterned constructs were incubated in osteogenic medium without DEX and BMP2 for 21 days. (e) Alizarin red stained (dark red) images of the patterned constructs along the length of a microchannel with none, dissolved, and NG-grafted BMP2/VEGF after 4 and 21 days of incubation. BMP2 and VEGF in NG-VEGF/NG-BMP2 group have 21 days and 10 days release, respectively.One star indicates statistically significant difference (s.d.; $p<0.05$) between the test group and None (green); two stars between the test group and BMP2/VEGF (red). Error bars correspond to means ± 1 SD for n=3.

The images in Figure 5.4g show Alizarin red staining along the length of a microchannel for the patterned constructs with none, dissolved, and NG-grafted BMP2/VEGF after 4 and 21 days of incubation. The image for patterned construct with NG-grafted BMP2/VEGF after 21 days (bottom right image) showed significantly higher staining in the matrix (dark red) and lower staining in the channels compared to the other groups.

3.2. Vasculogenic differentiation of hMSCs and ECFCs encapsulated in patterned hydrogels with BMP2 and VEGF NGs

DNA content, CD31 protein, and mRNA expression of vasculogenic markers for ECFCs+hMSCs/NG-VEGF encapsulated in GelMA channels and hMSCs/NG-BMP2 encapsulated in SPELA matrix in the patterned constructs are shown in Figure 5.5 (blue curve). Controls included ECFCs+hMSCs in the channels and hMSCs in the matrix with (red curve, without NG grafting) and without (green curve) VEGF and BMP2 in the channels and matrix, respectively. Other controls included ECFCs+hMSCs/VEGF (dashed pink) and ECFCs+hMSCs/NG-VEGF (dashed light blue) in GelMA (no SPELA) and cultured in vasculogenic medium (without VEGF) for 21 days. DNA content of the groups with BMP2/VEGF (with or without NG grafting) decreased with time with differentiation of the encapsulated cells [134] (Figure 5.5 a). CD31 protein expression for the patterned construct without BMP2/VEGF (green curve) did not increase significantly with time (Figure 5.5 b,c). CD31 expression of the un-patterned vasculogenic constructs with VEGF (dashed pink) or NG-VEGF (dashed light blue) increased with time but the CD31 expression for the NG-VEGF construct was significantly higher than that of VEGF (Figure 5.5 b,c). The patterned constructs (solid lines) had higher CD31 expression than the un-patterned vasculogenic constructs (dashed lines) for all incubation times. For example after 10 days of incubation, CD31 expressions for patterned constructs with NG-BMP2/NG-VEGF and BMP2/VEGF were 0.91±0.08 and 0.75±0.12, respectively; the expressions for the un-patterned vasculogenic constructs were 0.78±0.12 and 0.52±0.07. For all time points, CD31 expression of patterned construct with NG-BMP2/NG-VEGF

was higher than the other groups. mRNA expressions of vWF, CD31, and VE-cadherin (Figure 5.5 d-f) with incubation time were consistent with the CD31 protein expression in Figure 5.5 b. The patterned construct with NG-BMP2/NG-VEGF (blue curve) had higher expression of vWF, CD31, and VE-cadherin than the other groups for all time points.

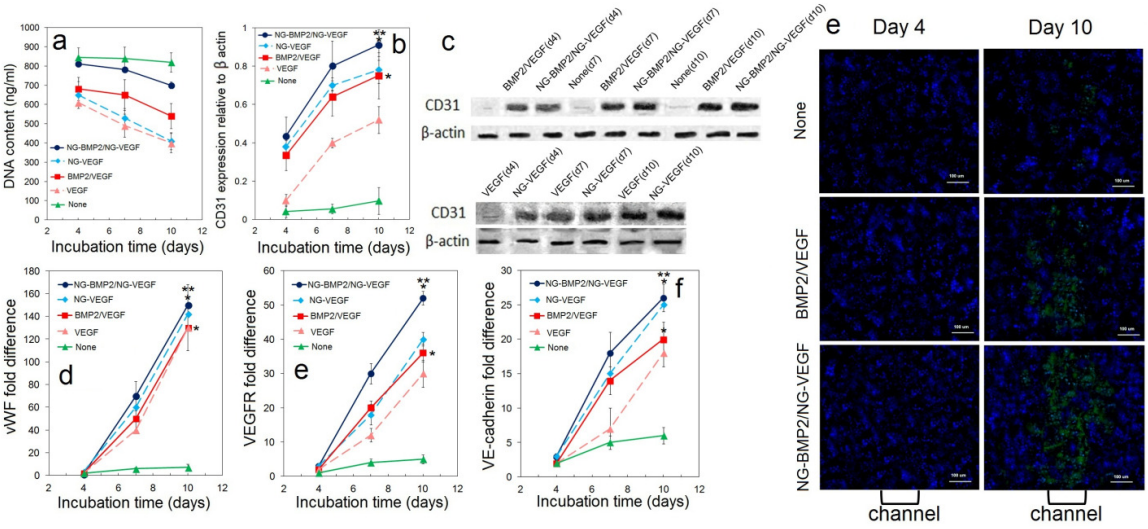

Figure 5.5. DNA content (a), CD31protein expression (b), representative western blot bands (c), and mRNA expression of vasculogenic markers vWF (d), CD31 (e), and VE-cadherin (f) for hMSCs and ECFCs in the patterned constructs (see Figure 5.4 for the groups). (e) CD31 stained (green) images of the patterned constructs along the length of a microchannel with none, dissolved, and NG-grafted BMP2/VEGF after 4 and 10 days of incubation. BMP2 and VEGF in NG-VEGF/NG-BMP2 group have 21 days and 10 days release, respectively. One star indicates statistically significant difference (s.d.; $p<0.05$) between the test group and None (green); two stars between the test group and BMP2/VEGF (red). Error bars correspond to means ± 1 SD for n=3.

The images in Figure 5.5 g show CD31 staining (green) along the length of a microchannel for the patterned constructs with none, dissolved, and NG-grafted BMP2/VEGF after 4 and 10 days of incubation. The image for patterned construct with NG-grafted BMP2/VEGF after 10 days (bottom right image) showed significantly higher CD31 expression in the channel compared to the other groups.

bFGF protein expression of the un-patterned osteogenic, patterned, and un-patterned vasculogenic constructs are shown in Figures 5.6 a-c, respectively. For a given time

point, patterned constructs and the un-patterned osteogenic constructs had highest and lowest expression of bFGF, respectively, with or without protein grafting. For a given culture system, the groups with grafted proteins had the highest expression of bFGF after 14 and 21 days of incubation. Overall, the patterned construct with NG-BMP2/NG-VEGF had highest expression of bFGF after 14 and 21 days among all groups (Figure 5.6 b). For example, bFGF expression of the patterned construct with none, dissolved, and NG-grafted BMP2/VEGF after 21 days incubation was 160±7, 54±4, and 23±1 ng/mL, respectively (Figure 5.6 b); those of the un-patterned vasculogenic constructs was 110±12, 48±4, and 19±5 ng/mL (Figure 5.6 c); and those of the un-patterned osteogenic constructs was 49±7, 14±4, and zero ng/mL (Figure 5.6 a). In addition, the effect BMP2 and VEGF release rate in patterned constructs on bFGF protein expression has been shown in figure 5.6.

The groups with 21 days release of BMP2 and 10 days release of VEGF (dashed blue curve) had the highest bFGF expression compared to the other two groups with 10 days or 21 days release for both BMP2 and VEGF (dashed green and red curves) with 149±9 and 120±6 ng/ml bFGF expression, respectively, after 21 days.It should be mentioned that there was no significant difference between the bFGF expression of NG(21)-BMP2/NG(10)-VEGF and NG(10)-BMP2/NG(10)-VEGF groups.

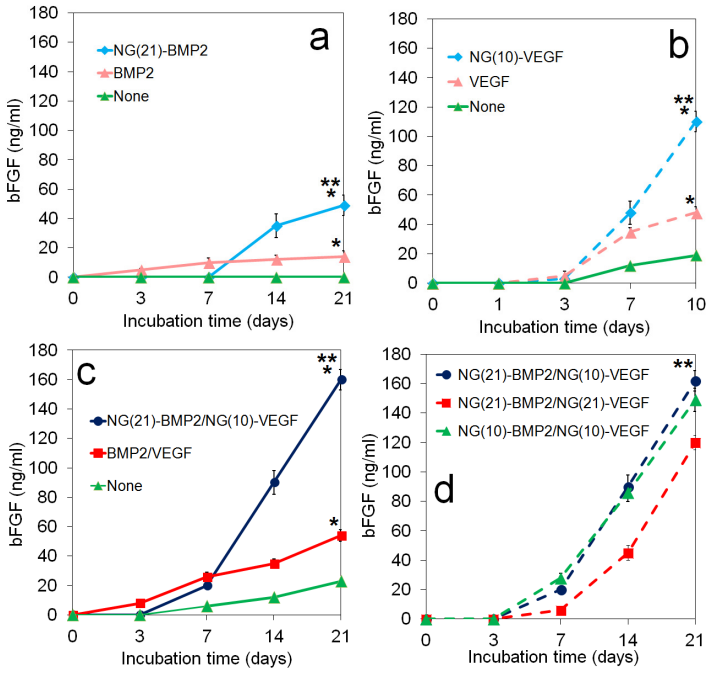

Figure 5.6. bFGF protein expression of the un-patterned osteogenic (a), patterned (b), and un-patterned vasculogenic (c) constructs with incubation time for the groups with none, VEGF/BMP2, and NG(21)-BMP2/NG(10)-VEGF. (d) Effect of BMP2 and VEGF release rate on bFGF protein expression of patterned construct. Groups included patterned constructs without VEGF/BMP2 (green, c), with VEGF/BMP2 (red, c), and with NG(21)-BMP2/NG(10)-VEGF (blue, b); un-patterned osteogenic constructs with NG(21)-BMP2 (light blue, a) and with BMP2 (pink, a); and un-patterned vasculogenic constructs with NG(10)-VEGF (dashed light blue in b) and with VEGF (dashed pink in b). Groups with NG(21)-BMP2/NG(10)-VEGF (dashed blue in d), NG(21)-BMP2/NG(21)-VEGF (dashed red in d) and NG(10)-BMP2/NG(10)-VEGF (dashed green in d) shows patterned construct with different protein release rate. The numbers in abbreviations NG(21) and NG(10) represent the release time of grafted proteins on each type of NG. One star indicates statistically significant difference (s.d.; $p<0.05$) between the test group and None (green); two stars between the test group and BMP2 (pink in a) or VEGF (dashed pink in b) or BMP2/VEGF (red in c) or NG(21)-BMP2/NG(21)-VEGF (dashed red in d). Error bars correspond to means ± 1 SD for n=3.

4. Discussion

It has been reported that the extent of bone formation *in vivo* depends on the duration of BMP2 exposure to MSCs in the first four weeks [135, 136] whereas vascularization depends on VEGF exposure to endothelial progenitor cells within the first week [137]. Therefore, P8-I NGs with 90% BSA release in 24 days and P12-II NGs with 70% BSA

release in 7 days were used for timed release of BMP2 and VEGF in the osteogenic SPELA matrix and vasculogenic GelMA channels, respectively. 78% and 71% of the grafted VEGF and BMP2 proteins, respectively, were released at a constant rate for 7 and 21 days, without an initial burst release [150], in the enzymatically-active conformation. Comparison of BSA (70 kDa) release curves with those of VEGF (40 kDa) and BMP2 (26 kDa) indicated that the protein release was dominated by the NGs degradation. PLGA and heparin-functionalized PLGA nanoparticles have previously been used for BMP2 delivery and gelatin microparticles have been used for VEGF. Attachment of BMP2 to heparin-functionalized PLGA (90 kDa) nanoparticles and their encapsulation in a fibrin gel prolonged the release to 2 weeks, but the fraction of bioactive BMP2 released was 23% compared to 57% for untreated PLGA nanoparticles [121]. Encapsulation in gelatin microspheres prolonged VEGF release to 2 weeks but <45% of the protein was released from the microparticles [150]. In another study, the fraction of bioactive BSA released from PLGA (45 kDa) nanoparticles increased from 50% to 70% after 1 week incubation by copolymerization of PLGA with PEG (5 kDa) [120]. We previously reported that the release of BMP2 can be extended to 4 weeks by grafting to succinimide-functionalized blend of ULMW-PLA/PLEOF nanoparticles but <50% of the released protein was enzymatically active [118]. Release kinetic of VEGF and BMP2 from PaLGb-Lc NGs (Figure 4.3 g) suggests that hydrophilic NGs are a more efficient platform for grafting and timed-release of proteins than hydrophobic PLGA nanoparticles. The lower bioactivity of BMP2 released from PLGA nanoparticles could be attributed to protein denaturation by acidic degradation products of PLGA and protein adsorption/unfolding [122].

Several recent studies have investigated the combined effect of VEGF and BMP2 on osteogenesis and vascularization [157, 158, 160-162]. Based on previous experimental results, co-expression of BMP2 and VEGF in MSC cultures had no effect on the extent of mineralization *in vitro*. On the other hand, combination of MSCs and EPCs in a calcium sulfate scaffold without over-expression of BMP2 showed higher mineralization *in vitro* compared to BMP2-expressing MSC only group [158]. Dual delivery of VEGF and BMP2 *in vivo* increased bone formation only at early time points but it was relatively independent of VEGF at late time points [160, 162, 163]. In another study, combination of BMP2-expressing MSCs and VEGF-expressing EPCs in a scaffold significantly increased bone formation after intramuscular implantion in rat [161]. The previous results indicate that dual delivery of BMP2 and VEGF increases osteogenesis only in MSC and EPC co-cultures. Our results in Figures 5.4 and 5.5 demonstrate that localized, dual delivery of VEGF to ECFCs+hMSCs in the channels and BMP2 to hMSCs in the matrix significantly increased the extent of mineralization and vascularization. Further, localized timed-release of VEGF in the channels and BMP2 in the matrix by grafting to NGs significantly improved mineralization and vascularization (blue curves in Figures 5.4-5.5) compared to direct addition of growth factors (red curves in Figures 5.4-5.5).

These results suggest that differentiation and maturation of MSCs and ECFCs to osteoblasts and endothelial cells induced by BMP2 and VEGF, respectively, may be indirectly coupled; that is differentiation of ECFCs+hMSCs in the channels by VEGF leads to the release of osteogenic factors that diffuse to the matrix to stimulate osteogenesis. bFGF is shown to mediate vascularization and bone formation in MSC seeded scaffolds [166, 167]. Therefore, we measured the expression of bFGF at the protein

level for the un-patterned and patterned constructs (Figure 5.6). The un-patterned vasculogenic construct without VEGF expressed low levels of bFGF after 7 and 10 days incubation (green in c) whereas the un-patterned osteogenic construct without BMP2 did not express bFGF in 21 days (green in a). The un-patterned vasculogenic construct with VEGF (dashed pink and blue in c) had higher expression of bFGF than the un-patterned osteogenic construct with BMP2 (dashed pink and blue in a). bFGF expression of the patterned construct with direct addition of BMP2/VEGF (red in b) was comparable to those of un-patterned vasculogenic construct with VEGF (dashed pink in c). Overall, timed-release of NG grafted BMP2/VEGF significantly enhanced bFGF expression level in un-patterned (dashed pink in a,c) and patterned (blue in b) constructs. However, timed-release of BMP2/VEGF in the patterned construct sharply increased bFGF expression level after 14 and 21 days (blue in b) compared to direct addition of the growth factors (red in b). The results with NG-BMP2/NG-VEGF support previous reports on the effect of timed-release of VEGF and BMP2 on vascularization and osteogenesis, respectively [168-170].

During endochondral ossification, maximum levels of VEGF precede maximum levels of new bone formation [155]. In the mineralization front, differentiated vascular endothelial cells in the invading vessels secrete growth factors that stimulate differentiation of MSCs to the osteogenic lineage [149]. Consistent with the process of bone development *in vivo*, bFGF expression levels in Figure 5.6 suggests that the differentiated ECFCs+hMSCs in the channels secret bFGF, and possibly other growth factors, that synergistically enhance osteogenic differentiation of hMSCs and mineralization. The data in Figure 5.6 also indicates that timed-release of NG-grafted VEGF in the channels leads

to sustained production of bFGF in the first week of co-culture to stimulate maturation of the differentiated cells to osteoblasts and endothelial cells.

5. Conclusion

We investigated the effect of spatial and temporal release of BMP2 and VEGF on the extent of osteogenic and vasculogenic differentiation of hMSCs and ECFCs encapsulated in a patterned hydrogel. For timed-release, BMP2 and VEGF were grafted to resorbable NGs based on self-assembly of PEG macromers chain-extended with short L and G segments. Degradation rate and protein release of the NGs increased with decreasing L to G ratio. Based on NGs release profile, P12-II NGs with 12 kDa PEG MW, 12 LG segment length, and 60/40 L/G ratio was selected for VEGF grafting and release in 7 days. P8-I NGs with 8 kDa PEG MW, 13 LG segment length, and 60/40 L/G ratio was selected for BMP2 grafting and release in 21 days. Enzymatic activity of the released VEGF and BMP2 after 7 and 21 days was 80% and 71%, respectively. hMSCs and ECFCs were encapsulated in patterned hydrogels with NG-grafted proteins; that is, hMSCs and BMP2-NGs encapsulated in SPELA matrix and hMSCs+ECFCs and VEGF-NGs in GelMA microchannels. Control groups were hMSCs in the un-patterned SPELA and hMSCs/ECFCs in the un-patterned GelMA. Based on the results, the extent of osteogenic and vasculogenic differentiation of hMSCs and ECFCs was higher in patterned constructs compared to un-patterned constructs. The addition of VEGF-NGs in the channels and BMP2-NGs to the matrix significantly increased osteogenic and vasculogenic differentiation of hMSCs and ECFCs compared to the addition of VEGF and BMP2. The patterned constructs with timed-release of NG-grafted VEGF and BMP2 had highest extent of osteogenic and vasculogenic differentiation. Further, timed-release

of NG-grafted VEGF in hMSC+ECFC seeded channels and NG-grafted BMP2 in hMSC-seeded matrix sharply increased bFGF expression after 21 days in the co-cultured constructs. The results suggest that mineralization and vascularization may be coupled by localized secretion of paracrine signaling factors like bFGF by differentiating hMSCs and ECFCs.

CHAPTER 6: FUTURE WORK

Traditional attempts to grow bone grafts in the laboratory were based on culturing cell/scaffold constructs under static conditions in the presence of osteogenesis-inducing factors. However, static cultures are not optimal to grow centimeter-sized bone grafts for clinical translation due to poor nutrient supply and removal of metabolic waste. Under these conditions, in fact, mass transport occurs only via diffusion, which is not sufficient to support cell survival and proliferation inside the core of large cell/scaffold constructs, resulting in necrosis and poor tissue formation. In addition, cell proliferation and matrix synthesis at the construct periphery over the culture period further impede medium diffusion and contribute to the formation of a nutrient gradient that drive cell migration towards the substitute borders [171]. On top of this, culture in static conditions does not allow provision of those biophysical stimuli that are critical for functional regeneration [172, 173]. In fact, bone cells are sensitive to mechanical stimuli, whose integration and conversion into intracellular signals play an important role in driving bone remodeling throughout lifetime and regeneration during fracture healing [174, 175]. Human bone is principally subjected to two types of mechanical stimuli, i.e., strain caused by deformation (bending and compression) resulting from physical activity (estimated values <2000 με), and fluid shear stress resulting from interstitial fluid movement through the lacunae as a consequence of loading (estimated values 0.8–3 Pa) [176].

Conversion of physical stimuli into molecular signals and biological responses is termed mechanotransduction, which principally relies on the regulation of stretch-activated ion channels and integrin-initiated cytoskeleton deformations and organelle displacement [177] that ultimately triggers the initiation of a cascade of events culminating in the activation of genes involved in osteogenic pathways [176]. Based on this knowledge, it is clear that the recapitulation of these mechanisms in vitro is essential for fostering the regenerative properties of human osteocompetent cells seeded onto biomaterial scaffolds, thus enabling the formation of mature tissue substitutes for enhanced skeletal reconstructions. Advances in bioreactor systems over the last two decades have opened new possibilities in the field of bone engineering as they allow to nurture the development of bone tissue by providing an appropriate physiological environment with stimulatory biochemical and biophysical signals [178]. The combination of stem cells, biomaterials, osteogenesis-inducing factors and bioreactor systems has recently been defined as the "Tissue Engineering Quadriad" [179], with the culture under dynamic conditions representing a paradigm shift for the ex vivo construction of viable tissue substitutes for replacement and reconstructive therapies. Not least, the construction of viable bone substitutes using bioreactor systems opens new opportunities for the generation of valid experimental models to study bone development and pathologies, screen new drugs and test biomaterials within a context that better reflects the native tissue environment. Therefore, the first step in the future would be evaluating the extent of osteogenesis and vasculogenesis of stem cells in the engineered shell-core composite with timed and localized delivery of BMP2 and VEGF with respect to mineralization and vascularization *in vitro* in a dynamic direct perfusion bioreactor.

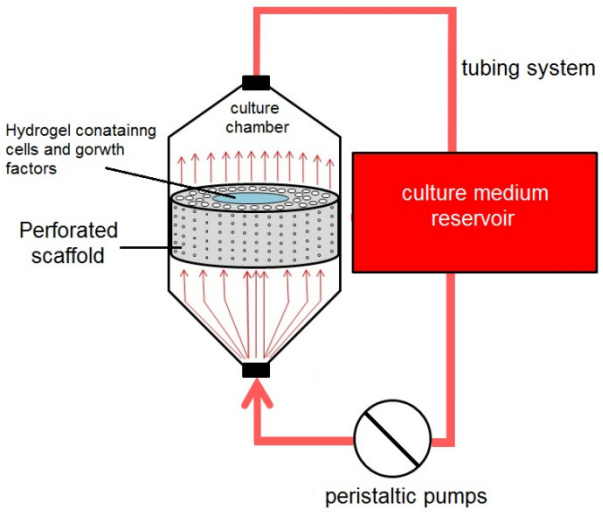

Figure 6.1. Schematic representation of direct perfusion bioreactor. In direct perfusion bioreactors the cell/scaffold constructs are placed in a press-fitted fashion in the culture chamber and the medium is perfused throughout the constructs.

To design the bioreactor system, microtubular shells with 8 mm outer diameter and 3 mm wall thickness will be used to direct the flow of osteogenic medium in the hioreactor of a perfusion cell culture. The interconnected microcanals of the shell will be injected with a mixture of BMP2 (200 ng/mL) and 5xlob hMSCs in collagen type I. The scaffolds will be press-fitted into a silicone tube to yield the bioreactor section of the perfusion system (Figure 6.2 b). The medium will be oxygenated in the reservoir which has one inlet and 16 outlets to allow simultaneous perfusion of 16 shells (Figure 6.2 a).

Factors that affect the transport of nutrients and oxygen in the central part of the engineered shell-core graft are the spacing between the Volkmann canals in the rigid shell and the spacing between the microchannels in the soft core (Figure 1.2).

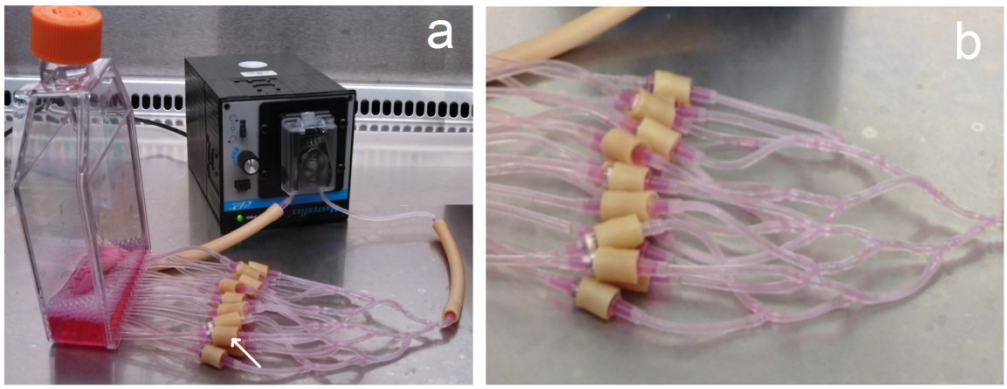

Figure 6.2. 16 perfusion bioreactors in parallel (arrow shows one of the reactors). (b) The perfusion cell culture system.

The average wall thickness of osteons in the native compact bone is 150 µm [180]. Therefore for 5-µm microsheet thickness, microtubes will consist of 30 lamellar layers. The spacing between the Volkmann canals in the natural bone varies between 500-1000 µm [181]. Therefore, microdrilling will be used to vary the spacing between the Volkmann-like canals in the engineered graft from 500 to 750 and 1000 µm. The spacing between the needles in the soft GeIMA gel will also be varied from 500 to 750 and 1000 µm. The rigid shell will be synthesized as described before [181]. An array of circular microholes with intervals of 500, 750, or 1000 µm will be drilled by laser microdrilling on the outside surface of the shell traversing the shell thickness. Next, the shell will be sterilized and all subsequent steps will be done under sterile condition. Then, needles with separation distance of 500-1000 µm will be placed inside the shell through an end-cap. The sterile GeIMA precursor solution, NG-VEGF, and human MSCs+EPCs (50:50, $2xl0^6$ cells/ml of GeLMA) will be injected between the needles and cross-linked with UV as we described previously [182] and needles are removed. Finally, the interconnected microcanals

of the shell wall will be filled with NG-BMP2 and human MSCs ($2x10^6$ cells/ml collagen) in collagen type I solution. The cellular constructs with timed-release of growth factors will be press-fitted into a silicone tube as the bioreactor section of the perfusion system (Figure 6.2 b) and culture medium will pumped through the bioreactors at the rate of 0.5 mL/min for 21 days as described. At each time point (1, 3,7. 10, 14. 21), the middle section of the graft will he characterized with respect to cellularity, extent of mineralization, and extent of vascularization as we previously described [134, 182, 183]. Microvessels will be visualized with Image ProPlus software to determine uniformity and total capillary density as described [35].

REFERENCES

1. Salgado, A.n.J., O.P. Coutinho, and R.L. Reis, *Bone tissue engineering: state of the art and future trends.* Macromolecular bioscience, 2004. **4**(8): p. 743-765.
2. Sikavitsas, V.I., J.S. Temenoff, and A.G. Mikos, *Biomaterials and bone mechanotransduction.* Biomaterials, 2001. **22**(19): p. 2581-2593.
3. Turner, C.H., T. Wang, and D.B. Burr, *Shear strength and fatigue properties of human cortical bone determined from pure shear tests.* Calcified tissue international, 2001. **69**(6): p. 373-378.
4. Rodan, G.A., *Introduction to bone biology.* Bone, 1992. **13**: p. S3-S6.
5. Siemionow, M., et al., *Composite vascularized skin/bone graft model: a viable source for vascularized bone marrow transplantation.* Microsurgery, 2004. **24**(3): p. 200-206.
6. FrÃ¶hlich, M., et al., *Tissue engineered bone grafts: biological requirements, tissue culture and clinical relevance.* Current stem cell research & therapy, 2008. **3**(4): p. 254.
7. Burg, K.J.L., S. Porter, and J.F. Kellam, *Biomaterial developments for bone tissue engineering.* Biomaterials, 2000. **21**(23): p. 2347-2359.
8. Zhang, P., K. Hamamura, and H. Yokota, *A brief review of bone adaptation to unloading.* Genomics, proteomics & bioinformatics, 2008. **6**(1): p. 4-7.
9. Simon, J.A., J.L. Ricci, and P.E. Di Cesare, *Bioresorbable fracture fixation in orthopedics: a comprehensive review. Part I. Basic science and preclinical studies.* American journal of orthopedics (Belle Mead, NJ), 1997. **26**(10): p. 665-671.
10. Porter, J.R., T.T. Ruckh, and K.C. Popat, *Bone Tissue Engineering: A Review in Bone Biomimetics and Drug Delivery Strategies.* Biotechnology Progress, 2009. **25**(6): p. 1539-1560.
11. Sargeant, T.D., et al., *Hybrid bone implants: self-assembly of peptide amphiphile nanofibers within porous titanium.* Biomaterials, 2008. **29**(2): p. 161-171.
12. Nakahara, H., et al., *Bone repair using a hybrid scaffold of self-assembling peptide PuraMatrix and polyetheretherketone cage in rats.* Cell transplantation. **19**(6-7): p. 791-797.

13. Peppas, N.A., et al., *Hydrogels in biology and medicine: from molecular principles to bionanotechnology.* Advanced Materials, 2006. **18**(11): p. 1345-1360.

14. Drury, J.L. and D.J. Mooney, *Hydrogels for tissue engineering: scaffold design variables and applications.* Biomaterials, 2003. **24**(24): p. 4337-4351.

15. Burdick, J.A. and K.S. Anseth, *Photoencapsulation of osteoblasts in injectable RGD-modified PEG hydrogels for bone tissue engineering.* Biomaterials, 2002. **23**(22): p. 4315-4323.

16. Igwe, J.C., P.E. Mikael, and S.P. Nukavarapu, *Design, fabrication and in vitro evaluation of a novel polymerâ€ hydrogel hybrid scaffold for bone tissue engineering.* Journal of tissue engineering and regenerative medicine. **8**(2): p. 131-142.

17. Nguyen, J., et al., *Load regulates bone formation and Sclerostin expression through a TGFbeta-dependent mechanism.* PloS one. **8**(1): p. e53813.

18. Jonitz, A., et al., *Oxygen consumption, acidification and migration capacity of human primary osteoblasts within a three-dimensional tantalum scaffold.* Journal of Materials Science: Materials in Medicine. **22**(9): p. 2089-2095.

19. Levesque, J.P., F.M. Helwani, and I.G. Winkler, *The endosteal â€˜osteoblasticâ€™niche and its role in hematopoietic stem cell homing and mobilization.* Leukemia. **24**(12): p. 1979-1992.

20. Carano, R.A.D. and E.H. Filvaroff, *Angiogenesis and bone repair.* Drug discovery today, 2003. **8**(21): p. 980-989.

21. Kopp, H.G., et al., *Functional heterogeneity of the bone marrow vascular niche.* Annals of the New York Academy of Sciences, 2009. **1176**(1): p. 47-54.

22. Rabie, A.B.M. and U. HÃ¤gg, *Factors regulating mandibular condylar growth.* American Journal of Orthodontics and Dentofacial Orthopedics, 2002. **122**(4): p. 401-409.

23. Amini, A.R., C.T. Laurencin, and S.P. Nukavarapu, *Bone tissue engineering: recent advances and challenges.* Critical Reviewsâ„¢ in Biomedical Engineering. **40**(5).

24. Huang, Z., et al., *The sequential expression profiles of growth factors from osteroprogenitors to osteoblasts in vitro.* Tissue engineering, 2007. **13**(9): p. 2311-2320.

25. Devescovi, V., et al., *Growth factors in bone repair.* La Chirurgia degli organi di movimento, 2008. **92**(3): p. 161-168.

26. Malizos, K.N. and L.K. Papatheodorou, *The healing potential of the periosteum: molecular aspects.* Injury, 2005. **36**(3): p. S13-S19.

27. Collinâ€ Osdoby, P., et al., *Basic fibroblast growth factor stimulates osteoclast recruitment, development, and bone pit resorption in association with angiogenesis in vivo on the chick chorioallantoic membrane and activates isolated avian osteoclast resorption in vitro.* Journal of Bone and Mineral Research, 2002. **17**(10): p. 1859-1871.

28. Kanczler, J.M. and R.O. Oreffo, *Osteogenesis and angiogenesis: the potential for engineering bone.* Eur Cell Mater, 2008. **15**(2): p. 100-114.

29. Matassi, F., et al., *New biomaterials for bone regeneration.* Clinical cases in mineral and bone metabolism. **8**(1): p. 21-24.

30. Takahashi, Y., M. Yamamoto, and Y. Tabata, *Enhanced osteoinduction by controlled release of bone morphogenetic protein-2 from biodegradable sponge composed of gelatin and Î²-tricalcium phosphate.* Biomaterials, 2005. **26**(23): p. 4856-4865.

31. Kaneko, H., et al., *Direct stimulation of osteoclastic bone resorption by bone morphogenetic protein (BMP)-2 and expression of BMP receptors in mature osteoclasts.* Bone, 2000. **27**(4): p. 479-486.

32. Raida, M., et al., *Role of bone morphogenetic protein 2 in the crosstalk between endothelial progenitor cells and mesenchymal stem cells.* International journal of molecular medicine, 2006. **18**(4): p. 735-739.

33. Park, J.C., et al., *Doseâ€ and timeâ€ dependent effects of recombinant human bone morphogenetic proteinâ€ 2 on the osteogenic and adipogenic potentials of alveolar boneâ€ derived stromal cells.* Journal of periodontal research. **47**(5): p. 645-654.

34. Jeon, O., et al., *Long-term delivery enhances in vivo osteogenic efficacy of bone morphogenetic protein-2 compared to short-term delivery.* Biochemical and biophysical research communications, 2008. **369**(2): p. 774-780.

35. Chen, Y.C., et al., *Functional human vascular network generated in photocrosslinkable gelatin methacrylate hydrogels.* Advanced functional materials. **22**(10): p. 2027-2039.

36. Logeart-Avramoglou, D., et al., *Engineering bone: challenges and obstacles.* Journal of Cellular and Molecular Medicine, 2005. **9**(1): p. 72-84.

37. Yasuda, H., et al., *Repair of critical long bone defects using frozen bone allografts coated with an rhBMP-2-retaining paste.* Journal of Orthopaedic Science, 2012. **17**(3): p. 299-307.

38. Wheeler, D.L. and W.F. Enneking, *Allograft bone decreases in strength in vivo over time.* Clinical Orthopaedics and Related Research, 2005(435): p. 36-42.

39. Gruskin, E., et al., *Demineralized bone matrix in bone repair: History and use.* Advanced Drug Delivery Reviews, 2012. **64**(12): p. 1063-1077.

40. Hench, L.L. and J.M. Polak, *Third-generation biomedical materials.* Science, 2002. **295**(5557): p. 1014-+.

41. Causa, F., et al., *Poly-epsilon-caprolactone/hydroxyapatite composites for bone regeneration: in vitro characterization and human osteoblast response.* Journal of Biomedical Materials Research Part A, 2006. **76A**(1): p. 151-162.

42. Karaman, O., *Effect of Surface Modification of Nanofibers with Glutamic Acid Peptide on Calcium Phosphate Nucleation and Osteogenic Differentiation of Marrow Stromal Cells.* Journal of Tissue Engineering and Regenerative Medicine, 2013.

43. Moore, W.R., S.E. Graves, and G.I. Bain, *Synthetic bone graft substitutes.* Australian and New Zealand Journal of Surgery, 2001. **71**(6): p. 354-361.

44. Lindner, M., et al., *Calcium phosphate scaffolds mimicking the gradient architecture of native long bones.* Journal of Biomedical Materials Research Part A, 2014. **102**(10): p. 3677-3684.

45. Shin, Y.M., et al., *Promotion of human mesenchymal stem cell differentiation on bioresorbable polycaprolactone/biphasic calcium phosphate composite scaffolds for bone tissue engineering.* Biotechnology and Bioprocess Engineering, 2014. **19**(2): p. 341-349.

46. Kim, J.W., et al., *Volumetric bone regenerative efficacy of biphasic calcium phosphate-collagen composite block loaded with rhBMP-2 in vertical bone augmentation model of a rabbit calvarium (vol 100, pg 3304, 2012).* Journal of Biomedical Materials Research Part A, 2013. **101**(4): p. 1223-1223.

47. Ma, Z., et al., *Amorphous calcium phosphate/poly(D,L-lactic acid) composite nanofibers: Electrospinning preparation and biomineralization.* Journal of Colloid and Interface Science, 2011. **359**(2): p. 371-379.

48. van de Watering, F.C.J., et al., *Calcium phosphate/poly(D,L-lactic-co-glycolic acid) composite bone substitute materials: evaluation of temporal degradation and bone ingrowth in a rat critical-sized cranial defect.* Clinical Oral Implants Research, 2012. **23**(2): p. 151-159.

49. Hamada, Y., et al., *The preparation of PLLA/calcium phosphate hybrid composite and its evaluation of biocompatibility.* Dental Materials Journal, 2012. **31**(6): p. 1087-1096.

50. Wang, Q., et al., *In situ remineralizaiton of partially demineralized human dentine mediated by a biomimetic non-collagen peptide.* Soft Matter, 2011. **7**(20): p. 9673-9680.

51. Sarvestani, A.S., X. He, and E. Jabbari, *Osteonectin-derived peptide increases the modulus of a bone-mimetic nanocomposite.* European Biophysics Journal with Biophysics Letters, 2008. **37**(2): p. 229-234.

52. Li, B. and R.M. Aspden, *Composition and mechanical properties of cancellous bone from the femoral head of patients with osteoporosis or osteoarthritis.* Journal of Bone and Mineral Research, 1997. **12**(4): p. 641-651.

53. Xie, B.Q. and G.H. Nancollas, *How to control the size and morphology of apatite nanocrystals in bone.* Proceedings of the National Academy of Sciences of the United States of America, 2010. **107**(52): p. 22369-22370.

54. Hu, Y.Y., A. Rawal, and K. Schmidt-Rohr, *Strongly bound citrate stabilizes the apatite nanocrystals in bone.* Proceedings of the National Academy of Sciences of the United States of America, 2010. **107**(52): p. 22425-22429.

55. Brecevic, L. and H. Furedimilhofer, *Precipitation of Calcium Phosphates from Electrolyte-Solutions .5. Influence of Citrate Ions.* Calcified Tissue International, 1979. **28**(2): p. 131-136.

56. Hempel, U., et al., *Proliferation and differentiation of osteoblasts on biocement D modified with collagen type I and citric acid.* Journal of Biomedical Materials Research Part B-Applied Biomaterials, 2004. **71B**(1): p. 130-143.

57. Chung, E.J., M.J. Sugimoto, and G.A. Ameer, *The role of hydroxyapatite in citric acid-based nanocomposites: Surface characteristics, degradation, and osteogenicity in vitro.* Acta Biomaterialia, 2011. **7**(11): p. 4057-4063.

58. Sarda, S., et al., *Kinetic study of citric acid influence on calcium phosphate bone cements as water-reducing agent.* Journal of Biomedical Materials Research, 2002. **61**(4): p. 653-659.

59. Rhee, S.H. and J. Tanaka, *Effect of citric acid on the nucleation of hydroxyapatite in a simulated body fluid.* Biomaterials, 1999. **20**(22): p. 2155-2160.

60. Etienne, A., et al., *What controls fleshy fruit acidity? A review of malate and citrate accumulation in fruit cells.* Journal of Experimental Botany, 2013. **64**(6): p. 1451-1469.

61. Umadevi, M., M.R. Bindhu, and V. Sathe, *A Novel Synthesis of Malic Acid Capped Silver Nanoparticles using Solanum lycopersicums Fruit Extract.* Journal of Materials Science & Technology, 2013. **29**(4): p. 317-322.

62. Duthie, G.G. and A.D. Wood, *Natural salicylates: foods, functions and disease prevention.* Food & Function, 2011. **2**(9): p. 515-520.

63. DeBolt, S., D.R. Cook, and C.M. Ford, *L-Tartaric acid synthesis from vitamin C in higher plants.* Proceedings of the National Academy of Sciences of the United States of America, 2006. **103**(14): p. 5608-5613.

64. Hoffman, J.R., et al., *Thermogenic Effect from Nutritionally Enriched Coffee Consumption.* Journal of the International Society of Sports Nutrition, 2006. **3**.

65. Ma, J., X. He, and E. Jabbari, *Osteogenic Differentiation of Marrow Stromal Cells on Random and Aligned Electrospun Poly(L-lactide) Nanofibers.* Annals of Biomedical Engineering, 2011. **39**(1).

66. Xu, C.Y., et al., *Aligned biodegradable nanofibrous structure: a potential scaffold for blood vessel engineering.* Biomaterials, 2004. **25**(5): p. 877-886.

67. Yang, F., et al., *Electrospinning of nano/micro scale poly(l-lactic acid) aligned fibers and their potential in neural tissue engineering.* Biomaterials, 2005. **26**(15): p. 2603-2610.

68. da Cunha, C.B., et al., *Influence of the stiffness of three-dimensional alginate/collagen-I interpenetrating networks on fibroblast biology.* Biomaterials, 2014. **35**(32): p. 8927-8936.

69. Patterson, A.L., *The Scherrer formula for x-ray particle size determination.* Physical Review, 1939. **56**(10): p. 978-982.

70. Sanosh, K.P., et al., *Preparation and characterization of nano-hydroxyapatite powder using sol-gel technique.* Bulletin of Materials Science, 2009. **32**(5): p. 465-470.

71. Stipniece, L., et al., *The Study of Magnesium Substitution Effect on Physicochemical Properties of Hydroxyapatite.* Material Science and Applied Chemistry. **28**(28): p. 51-57.

72. Martins, M.A., et al., *Hydroxyapatite micro- and nanoparticles: Nucleation and growth mechanisms in the presence of citrate species.* Journal of Colloid and Interface Science, 2008. **318**(2): p. 210-216.

73. Landi, E., et al., *Densification behaviour and mechanisms of synthetic hydroxyapatites.* Journal of the European Ceramic Society, 2000. **20**(14-15): p. 2377-2387.

74. Danial Barati , S.M., Ozan Karaman , Esmaiel Jabbari, *Time Dependence of Material Properties of Polyethylene Glycol Hydrogels Chain Extended with Short Hydroxy Acid Segments.* Polymer, 2014. **S0032-3861(14)00433-9**.

75. Moeinzadeh, S., et al., *Gelation Characteristics and Osteogenic Differentiation of Stromal Cells in Inert Hydrolytically Degradable Micellar Polyethylene Glycol Hydrogels.* Biomacromolecules, 2012. **13**(7): p. 2073-2086.

76. He, C.L., X.B. Jin, and P.X. Ma, *Calcium phosphate deposition rate, structure and osteoconductivity on electrospun poly(L-lactic acid) matrix using electrodeposition or simulated body fluid incubation.* Acta Biomaterialia, 2014. **10**(1): p. 419-427.

77. Boanini, E., M. Gazzano, and A. Bigi, *Ionic substitutions in calcium phosphates synthesized at low temperature.* Acta Biomaterialia, 2010. **6**(6): p. 1882-1894.

78. Meng, Z.X., et al., *Fabrication of mineralized electrospun PLGA and PLGA/gelatin nanofibers and their potential in bone tissue engineering.* Materials Science & Engineering C-Materials for Biological Applications, 2013. **33**(2): p. 699-706.

79. Wang, X.Y., et al., *Comparative Study on Inorganic Composition and Crystallographic Properties of Cortical and Cancellous Bone.* Biomedical and Environmental Sciences, 2010. **23**(6): p. 473-480.

80. Schecroun, N. and C. Delloye, *Bone-like nodules formed by human bone marrow stromal cells: comparative study and characterizationâ˜†.* Bone, 2003. **32**(3): p. 252-260.

81. Tsigkou, O., et al., *Differentiation of fetal osteoblasts and formation of mineralized bone nodules by 45S5 Bioglass (R) conditioned medium in the absence of osteogenic supplements.* Biomaterials, 2009. **30**(21): p. 3542-3550.

82. Barralet, J.E., et al., *Modification of calcium phosphate cement with alpha-hydroxy acids and their salts.* Chemistry of Materials, 2005. **17**(6): p. 1313-1319.

83. Wang, X., *A theory for the mechanism of action of the Î±-hydroxy acids applied to the skin.* Medical hypotheses, 1999. **53**(5): p. 380-382.

84. LeGeros, R.Z., *Formation and transformation of calcium phosphates: relevance to vascular calcification.* Zeitschrift fÃ¼r Kardiologie, 2001. **90**(3): p. 116-124.

85. Chou, L., B. Marek, and W.R. Wagner, *Effects of hydroxylapatite coating crystallinity on biosolubility, cell attachment efficiency and proliferation in vitro.* Biomaterials, 1999. **20**(10): p. 977-985.

86. Zhang, W., et al., *Effect of calcium citrate on bone integration in a rabbit femur defect model.* Asian Pacific Journal of Tropical Medicine, 2012. **5**(4): p. 310-314.

87. Raucci, M.G., et al., *Effect of citric acid crosslinking celluloseâ€ based hydrogels on osteogenic differentiation.* Journal of Biomedical Materials Research Part A.

88. Langenbach, F. and J. Handschel, *Effects of dexamethasone, ascorbic acid and beta-glycerophosphate on the osteogenic differentiation of stem cells in vitro.* Stem Cell Research & Therapy, 2013. **4**.

89. Damien, C.J. and J.R. Parsons, *Bone graft and bone graft substitutes: A review of current technology and applications.* Journal of Applied Biomaterials, 1991. **2**(3): p. 187-208.

90. Scheller, E.L., P.H. Krebsbach, and D.H. Kohn, *Tissue engineering: state of the art in oral rehabilitation.* Journal of Oral Rehabilitation, 2009. **36**(5): p. 368-389.

91. Kretlow, J.D., et al., *Injectable Biomaterials for Regenerating Complex Craniofacial Tissues.* Advanced Materials, 2009. **21**(32-33): p. 3368-3393.

92. Frohlich, M., et al., *Tissue Engineered Bone Grafts: Biological Requirements, Tissue Culture and Clinical Relevance.* Current Stem Cell Research & Therapy, 2008. **3**(4): p. 254-264.

93. van Oers, R.F.M., et al., *Relating osteon diameter to strain.* Bone, 2008. **43**(3): p. 476-482.

94. Even-Ram, S. and K.M. Yamada, *Cell migration in 3D matrix.* Current Opinion in Cell Biology, 2005. **17**(5): p. 524-532.

95. Bartold, P.M., et al., *Tissue engineering: a new paradigm for periodontal regeneration based on molecular and cell biology.* Periodontology 2000, 2000. **24**: p. 253-269.

96. Chen, J.-P. and Y.-S. Chang, *Preparation and characterization of composite nanofibers of polycaprolactone and nanohydroxyapatite for osteogenic differentiation of mesenchymal stem cells.* Colloids and Surfaces B: Biointerfaces, 2011. **86**(1): p. 169-175.

97. Bolander, M.E., et al., *Osteonectin Cdna Sequence Reveals Potential Binding Regions for Calcium and Hydroxyapatite and Shows Homologies with Both a Basement-Membrane Protein (Sparc) and a Serine Proteinase-Inhibitor (Ovomucoid).* Proceedings of the National Academy of Sciences of the United States of America, 1988. **85**(9): p. 2919-2923.

98. Oldberg, A., A. Franzen, and D. Heinegard, *The Primary Structure of a Cell-Binding Bone Sialoprotein.* Journal of Biological Chemistry, 1988. **263**(36): p. 19430-19432.

99. Itoh, D., et al., *Enhancement of osteogenesis on hydroxyapatite surface coated with synthetic peptide (EEEEEEEPRGDT) in vitro.* Journal of Biomedical Materials Research, 2002. **62**(2): p. 292-298.

100. Sarvestani, A., X. He, and E. Jabbari, *Osteonectin-derived peptide increases the modulus of a bone-mimetic nanocomposite.* European Biophysics Journal, 2008. **37**(2): p. 229-234.

101. Schulz, A., *Bone-Structure and Remodeling Dynamics in Osteopathies.* Zeitschrift Fur Rheumatologie, 1988. **47**(4): p. 309-310.

102. Athanasiou, K.A., et al., *Fundamentals of biomechanics in tissue engineering of bone.* Tissue engineering, 2000. **6**(4): p. 361-381.

103. Ascenzi, A. and E. Bonucci, *The compressive properties of single osteons.* The Anatomical Record, 1968. **161**(3): p. 377-391.

104. Miyazaki, T., et al., *Mechanism of bonelike apatite formation on bioactive tantalum metal in a simulated body fluid.* Biomaterials, 2002. **23**(3): p. 827-832.

105. Liu, W., et al., *Enhancing the Stiffness of Electrospun Nanofiber Scaffolds with a Controlled Surface Coating and Mineralization.* Langmuir, 2011. **27**(15): p. 9088-9093.

106. Thomas, V., et al., *Electrospun bioactive nanocomposite scaffolds of polycaprolactone and nanohydroxyapatite for bone tissue engineering.* Journal of Nanoscience and Nanotechnology, 2006. **6**(2): p. 487-493.

107. Li, X., et al., *Nanofiber Scaffolds with Gradations in Mineral Content for Mimicking the Tendon-to-Bone Insertion Site.* Nano Letters, 2009. **9**(7): p. 2763-2768.

108. Holzwarth, J.M. and P.X. Ma, *3D nanofibrous scaffolds for tissue engineering.* Journal of Materials Chemistry, 2011. **21**(28): p. 10243-10251.

109. Gaggl, A., H. Rainer, and F.M. Chiari, *Horizontal distraction of the anterior maxilla in combination with bilateral sinuslift operationâ€"preliminary report.* International journal of oral and maxillofacial surgery, 2005. **34**(1): p. 37-44.

110. Fischgrund, J., D. Paley, and C. Suter, *Variables affecting time to bone healing during limb lengthening.* Clinical orthopaedics and related research, 1994. **301**: p. 31-37.

111. Malo, M.K.H., et al., *Longitudinal elastic properties and porosity of cortical bone tissue vary with age in human proximal femur.* Bone. **53**(2): p. 451-458.

112. Bae, S.E., et al., *Controlled release of bone morphogenetic protein (BMP)-2 from nanocomplex incorporated on hydroxyapatite-formed titanium surface.* Journal of controlled release. **160**(3): p. 676-684.

113. Gerstenfeld, L.C., et al., *Fracture healing as a postâ€ natal developmental process: Molecular, spatial, and temporal aspects of its regulation.* Journal of cellular biochemistry, 2003. **88**(5): p. 873-884.

114. Bostrom, M.P.G., *Expression of bone morphogenetic proteins in fracture healing.* Clinical orthopaedics and related research, 1998. **355**: p. S116-S123.

115. Street, J., et al., *Vascular endothelial growth factor stimulates bone repair by promoting angiogenesis and bone turnover.* Proceedings of the National Academy of Sciences, 2002. **99**(15): p. 9656-9661.

116. Jones, A.L., et al., *Recombinant human BMP-2 and allograft compared with autogenous bone graft for reconstruction of diaphyseal tibial fractures with cortical defectsA randomized, controlled trial.* The Journal of Bone & Joint Surgery, 2006. **88**(7): p. 1431-1441.

117. Eppler, S.M., et al., *A target-mediated model to describe the pharmacokinetics and hemodynamic effects of recombinant human vascular endothelial growth factor in humans.* CLINICAL PHARMACOLOGY AND THERAPEUTICS-ST LOUIS-, 2002. **72**(1): p. 20-32.

118. Mercado, A.E., et al., *Release characteristics and osteogenic activity of recombinant human bone morphogenetic protein-2 grafted to novel self-assembled poly(lactide-co-glycolide fumarate) nanoparticles.* Journal of controlled release, 2009. **140**(2): p. 148-156.

119. Mercado, A.E., et al., *The release characteristics of a model protein from self-assembled succinimide-terminated poly (lactide-co-glycolide ethylene oxide fumarate) nanoparticles.* Nanotechnology, 2008. **19**(32): p. 325609.

120. Li, Y.-P., et al., *PEGylated PLGA nanoparticles as protein carriers: synthesis, preparation and biodistribution in rats.* Journal of controlled release, 2001. **71**(2): p. 203-211.

121. Chung, Y.-I., et al., *Enhanced bone regeneration with BMP-2 loaded functional nanoparticle-hydrogel complex.* Journal of controlled release, 2007. **121**(1): p. 91-99.

122. Zhu, G., S.R. Mallery, and S.P. Schwendeman, *Stabilization of proteins encapsulated in injectable poly (lactide-co-glycolide).* Nature biotechnology, 2000. **18**(1): p. 52-57.

123. Crotts, G., H. Sah, and T.G. Park, *Adsorption determines in-vitro protein release rate from biodegradable microspheres: quantitative analysis of surface area during degradation.* Journal of controlled release, 1997. **47**(1): p. 101-111.

124. Gref, R., et al., *The controlled intravenous delivery of drugs using PEG-coated sterically stabilized nanospheres.* Advanced drug delivery reviews, 1995. **16**(2): p. 215-233.

125. Zhang, S., et al., *Polyethylenimine PEG coated albumin nanoparticles for BMP-2 delivery.* Biomaterials, 2009. **31**(5): p. 952-963.

126. Simon-Yarza, T., et al., *PEGylated-PLGA microparticles containing VEGF for long term drug delivery.* International journal of pharmaceutics, 2013. **440**(1): p. 13-18.

127. Moeinzadeh, S., et al., *Nanostructure Formation and Transition from Surface to Bulk Degradation in Polyethylene Glycol Gels Chain-Extended with Short Hydroxy Acid Segments.* Biomacromolecules, 2013. **14**(8): p. 2917-2928.

128. Mercado, A.E. and E. Jabbari, *Effect of encapsulation or grafting on release kinetics of recombinant human bone morphogenetic protein-2 from self-assembled poly (lactide-co-glycolide ethylene oxide fumarate) nanoparticles.* Microscopy Research and Technique, 2010. **73**(9): p. 824-833.

129. He, X.Z. and E. Jabbari, *Material properties and cytocompatibility of injectable MMP degradable poly(lactide ethylene oxide fumarate) hydrogel as a carrier for marrow stromal cells.* Biomacromolecules, 2007. **8**(3): p. 780-792.

130. He, X., X. Yang, and E. Jabbari, *Combined effect of osteopontin and BMP-2 derived peptides grafted to an adhesive hydrogel on osteogenic and vasculogenic differentiation of marrow stromal cells.* Langmuir, 2012. **28**(12): p. 5387-97.

131. Mirshahghassemi, S., B. Cai, and J.R. Lead, *Evaluation of polymer-coated magnetic nanoparticles for oil separation under environmentally relevant conditions: effect of ionic strength and natural organic macromolecules.* Environmental Science: Nano.

132. Afshinnia, K., et al., *The concentration-dependent aggregation of Ag NPs induced by cystine.* Science of The Total Environment. **557**: p. 395-403.

133. Mirshahghassemi, S. and J.R. Lead, *Oil Recovery from Water under Environmentally Relevant Conditions Using Magnetic Nanoparticles.* Environmental Science & Technology, 2015. **49**(19): p. 11729-11736.

134. Barati, D., et al., *Time dependence of material properties of polyethylene glycol hydrogels chain extended with short hydroxy acid segments.* Polymer, 2014. **55**(16): p. 3894-3904.

135. Park, J.C., et al., *Dose- and time-dependent effects of recombinant human bone morphogenetic protein-2 on the osteogenic and adipogenic potentials of alveolar bone-derived stromal cells.* J Periodontal Res, 2012. **47**(5): p. 645-54.

136. Jeon, O., et al., *Long-term delivery enhances in vivo osteogenic efficacy of bone morphogenetic protein-2 compared to short-term delivery.* Biochemical and biophysical research communications, 2008. **369**(2): p. 774-780.

137. Chen, Y.C., et al., *Functional Human Vascular Network Generated in Photocrosslinkable Gelatin Methacrylate Hydrogels.* Advanced Functional Materials, 2012. **22**(10): p. 2027-2039.

138. Forster, S., et al., *Micellization of strongly segregated block copolymers.* The Journal of chemical physics, 1996. **104**(24): p. 9956-9970.

139. Jokerst, J.V., et al., *Nanoparticle PEGylation for imaging and therapy.* Nanomedicine, 2011. **6**(4): p. 715-728.

140. Riley, T., et al., *Colloidal stability and drug incorporation aspects of micellar-like PLA-PEG nanoparticles.* Colloids and surfaces B: Biointerfaces, 1999. **16**(1): p. 147-159.

141. Beletsi, A., Z. Panagi, and K. Avgoustakis, *Biodistribution properties of nanoparticles based on mixtures of PLGA with PLGA-PEG diblock copolymers.* International journal of pharmaceutics, 2005. **298**(1): p. 233-241.

142. Zweers, M.L.T., et al., *In vitro degradation of nanoparticles prepared from polymers based on DL-lactide, glycolide and poly (ethylene oxide).* Journal of controlled release, 2004. **100**(3): p. 347-356.

143. Avgoustakis, K., et al., *PLGA-mPEG nanoparticles of cisplatin: in vitro nanoparticle degradation, in vitro drug release and in vivo drug residence in blood properties.* Journal of controlled release, 2002. **79**(1): p. 123-135.

144. Youxin, L. and T. Kissel, *Synthesis and properties of biodegradable ABA triblock copolymers consisting of poly (L-lactic acid) or poly (L-lactic-co-glycolic acid) A-blocks attached to central poly (oxyethylene) B-blocks.* Journal of controlled release, 1993. **27**(3): p. 247-257.

145. Molina, C.S., D.J. Stinner, and W.T. Obremskey, *Treatment of traumatic segmental long-bone defects: A critical analysis review.* JBJS Reviews, 2014. **2**(4): p. e1.

146. Yasuda, H., et al., *Repair of critical long bone defects using frozen bone allografts coated with an rhBMP-2-retaining paste.* J Orthop Sci, 2012. **17**(3): p. 299-307.

147. Lissenberg-Thunnissen, S.N., et al., *Use and efficacy of bone morphogenetic proteins in fracture healing.* International Orthopaedics, 2011. **35**(9): p. 1271-1280.

148. Carragee, E.J., E.L. Hurwitz, and B.K. Weiner, *A critical review of recombinant human bone morphogenetic protein-2 trials in spinal surgery: emerging safety concerns and lessons learned.* Spine Journal, 2011. **11**(6): p. 471-491.

149. Yang, Y.Q., et al., *The role of vascular endothelial growth factor in ossification.* International Journal of Oral Science, 2012. **4**(2): p. 64-68.

150. Poldervaart, M.T., et al., *Prolonged presence of VEGF promotes vascularization in 3D bioprinted scaffolds with defined architecture.* Journal of controlled release, 2014. **184**: p. 58-66.

151. Kleinheinz, J., et al., *Release kinetics of VEGF165 from a collagen matrix and structural matrix changes in a circulation model.* Head & Face Medicine, 2010. **6**(1): p. 17.

152. Bae, S.E., et al., *Controlled release of bone morphogenetic protein (BMP)-2 from nanocomplex incorporated on hydroxyapatite-formed titanium surface.* Journal of controlled release, 2012. **160**(3): p. 676-684.

153. Levesque, J.P., F.M. Helwani, and I.G. Winkler, *The endosteal 'osteoblastic' niche and its role in hematopoietic stem cell homing and mobilization.* Leukemia, 2010. **24**(12): p. 1979-1992.

154. Dai, J. and A.B.M. Rabie, *VEGF: an essential mediator of both angiogenesis and endochondral ossification.* Journal of Dental Research, 2007. **86**(10): p. 937-950.

155. Rabie, A.B.M. and U. Hagg, *Factors regulating mandibular condylar growth.* American Journal of Orthodontics and Dentofacial Orthopedics, 2002. **122**(4): p. 401-409.

156. Kopp, H.G., et al., *Functional Heterogeneity of the Bone Marrow Vascular Niche.* Hematopoietic Stem Cells Vii, 2009. **1176**: p. 47-54.

157. Lin, Z.W., et al., *Effects of BMP2 and VEGF165 on the osteogenic differentiation of rat bone marrow-derived mesenchymal stem cells.* Experimental and Therapeutic Medicine, 2014. **7**(3): p. 625-629.

158. He, X.N., et al., *BMP2 Genetically Engineered MSCs and EPCs Promote Vascularized Bone Regeneration in Rat Critical-Sized Calvarial Bone Defects.* Plos One, 2013. **8**(4).

159. Lin, R.Z., et al., *Human endothelial colony-forming cells serve as trophic mediators for mesenchymal stem cell engraftment via paracrine signaling.* Proceedings of the National Academy of Sciences of the United States of America, 2014. **111**(28): p. 10137-10142.

160. Geuze, R.E., et al., *A Differential Effect of Bone Morphogenetic Protein-2 and Vascular Endothelial Growth Factor Release Timing on Osteogenesis at Ectopic and Orthotopic Sites in a Large-Animal Model.* Tissue Engineering Part A, 2012. **18**(19-20): p. 2052-2062.

161. Song, X.B., et al., *BMP2 and VEGF promote angiogenesis but retard terminal differentiation of osteoblasts in bone regeneration by up-regulating Id1.* Acta Biochimica Et Biophysica Sinica, 2011. **43**(10): p. 796-804.

162. Patel, Z.S., et al., *Dual delivery of an angiogenic and an osteogenic growth factor for bone regeneration in a critical size defect model.* Bone, 2008. **43**(5): p. 931-940.

163. Kempen, D.H.R., et al., *Effect of local sequential VEGF and BMP-2 delivery on ectopic and orthotopic bone regeneration.* Biomaterials, 2009. **30**(14): p. 2816-2825.

164. Matsubara, H., et al., *Vascular tissues are a primary source of BMP2 expression during bone formation induced by distraction osteogenesis.* Bone, 2012. **51**(1): p. 168-180.

165. Moeinzadeh, S., et al., *Gelation characteristics and osteogenic differentiation of stromal cells in inert hydrolytically degradable micellar polyethylene glycol hydrogels.* Biomacromolecules, 2012. **13**(7): p. 2073-2086.

166. Kim, J.M., et al., *DJ-1 promotes angiogenesis and osteogenesis by activating FGF receptor-1 signaling.* Nature Communications, 2012. **3**.

167. Qu, D., et al., *Angiogenesis and osteogenesis enhanced by bFGF ex vivo gene therapy for bone tissue engineering in reconstruction of calvarial defects.* Journal of Biomedical Materials Research Part A, 2011. **96A**(3): p. 543-551.

168. des Rieux, A., et al., *3D systems delivering VEGF to promote angiogenesis for tissue engineering.* Journal of controlled release, 2011. **150**(3): p. 272-278.

169. Formiga, F.R., et al., *Sustained release of VEGF through PLGA microparticles improves vasculogenesis and tissue remodeling in an acute myocardial ischemia-reperfusion model.* Journal of controlled release, 2010. **147**(1): p. 30-37.

170. Wang, Z., et al., *BMP-2 encapsulated polysaccharide nanoparticle modified biphasic calcium phosphate scaffolds for bone tissue regeneration.* Journal of Biomedical Materials Research Part A, 2015.

171. Goldstein, A.S., et al., *Effect of convection on osteoblastic cell growth and function in biodegradable polymer foam scaffolds.* Biomaterials, 2001. **22**(11): p. 1279-1288.

172. Yeatts, A.B. and J.P. Fisher, *Bone tissue engineering bioreactors: dynamic culture and the influence of shear stress.* Bone. **48**(2): p. 171-181.

173. Klein-Nulend, J., et al., *Mechanosensation and transduction in osteocytes.* Bone. **54**(2): p. 182-190.

174. Klein-Nulend, J., R.G. Bacabac, and M.G. Mullender, *Mechanobiology of bone tissue.* Pathologie biologie, 2005. **53**(10): p. 576-580.

175. Huang, C. and R. Ogawa, *Mechanotransduction in bone repair and regeneration.* The FASEB Journal. **24**(10): p. 3625-3632.

176. McCoy, R.J. and F.J. O'Brien, *Influence of shear stress in perfusion bioreactor cultures for the development of three-dimensional bone tissue constructs: a review.* Tissue Engineering Part B: Reviews. **16**(6): p. 587-601.

177. Hoffman, B.D. and J.C. Crocker, *Cell mechanics: dissecting the physical responses of cells to force.* Annual review of biomedical engineering, 2009. **11**: p. 259-288.

178. Salter, E., et al., *Bone tissue engineering bioreactors: a role in the clinic?* Tissue Engineering Part B: Reviews. **18**(1): p. 62-75.

179. de Peppo, G.M., et al., *Human progenitor cells for bone engineering applications.* Current molecular medicine. **13**(5): p. 723-734.

180. Skedros, J.G., et al., *Analysis of the effect of osteon diameter on the potential relationship of osteocyte lacuna density and osteon wall thickness.* The Anatomical Record. **294**(9): p. 1472-1485.

181. Ross, M.H. and W. Pawlina, *Histology*. 2006: Lippincott Williams & Wilkins.

182. Barati, D., et al., *Spatiotemporal release of BMP-2 and VEGF enhances osteogenic and vasculogenic differentiation of human mesenchymal stem cells and endothelial colony-forming cells co-encapsulated in a patterned hydrogel.* Journal of Controlled Release. **223**: p. 126-136.

183. Barati, D., et al., *Effect of Organic Acids on Calcium Phosphate Nucleation and Osteogenic Differentiation of Human Mesenchymal Stem Cells on Peptide Functionalized Nanofibers.* Langmuir. **31**(18): p. 5130-5140.

APPENDIX A

COPYRIGHT RELEASE

Chapter 2

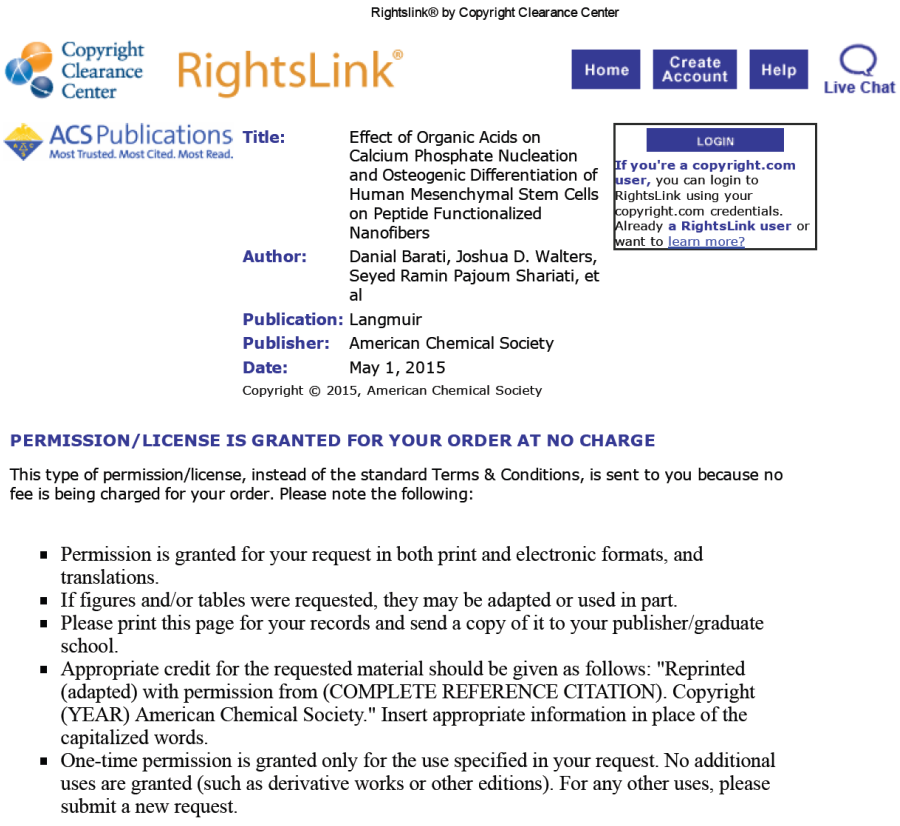

Rightslink® by Copyright Clearance Center

Copyright Clearance Center RightsLink®

Home | Create Account | Help | Live Chat

ACS Publications Most Trusted. Most Cited. Most Read.

Title: Effect of Organic Acids on Calcium Phosphate Nucleation and Osteogenic Differentiation of Human Mesenchymal Stem Cells on Peptide Functionalized Nanofibers

Author: Danial Barati, Joshua D. Walters, Seyed Ramin Pajoum Shariati, et al

Publication: Langmuir

Publisher: American Chemical Society

Date: May 1, 2015

Copyright © 2015, American Chemical Society

LOGIN

If you're a copyright.com user, you can login to RightsLink using your copyright.com credentials. Already a RightsLink user or want to learn more?

PERMISSION/LICENSE IS GRANTED FOR YOUR ORDER AT NO CHARGE

This type of permission/license, instead of the standard Terms & Conditions, is sent to you because no fee is being charged for your order. Please note the following:

- Permission is granted for your request in both print and electronic formats, and translations.
- If figures and/or tables were requested, they may be adapted or used in part.
- Please print this page for your records and send a copy of it to your publisher/graduate school.
- Appropriate credit for the requested material should be given as follows: "Reprinted (adapted) with permission from (COMPLETE REFERENCE CITATION). Copyright (YEAR) American Chemical Society." Insert appropriate information in place of the capitalized words.
- One-time permission is granted only for the use specified in your request. No additional uses are granted (such as derivative works or other editions). For any other uses, please submit a new request.

Chapter 4

RightsLink Printable License

ELSEVIER LICENSE
TERMS AND CONDITIONS

Jun 23, 20

This Agreement between Danial Barati ("You") and Elsevier ("Elsevier") consists of your license details and the terms and conditions provided by Elsevier and Copyright Clearance Center.

License Number	3894871316148
License date	Jun 23, 2016
Licensed Content Publisher	Elsevier
Licensed Content Publication	Journal of Controlled Release
Licensed Content Title	Spatiotemporal release of BMP-2 and VEGF enhances osteogenic an vasculogenic differentiation of human mesenchymal stem cells and endothelial colony-forming cells co-encapsulated in a patterned hydrogel
Licensed Content Author	Danial Barati,Seyed Ramin Pajoum Shariati,Seyedsina Moeinzadeh,Juan M. Melero-Martin,Ali Khademhosseini,Esmaiel Jabbari
Licensed Content Date	10 February 2016
Licensed Content Volume Number	223
Licensed Content Issue Number	n/a
Licensed Content Pages	11
Start Page	126
End Page	136
Type of Use	reuse in a thesis/dissertation
Portion	full article
Format	both print and electronic
Are you the author of this Elsevier article?	Yes
Will you be translating?	No
Order reference number	
Title of your thesis/dissertation	BIODEGRADABLE HYBRID TISSUE ENGINEERING SCAFFOLDS FOR RECONSTRUCTION OF LARGE BONE DEFECTS
Expected completion date	Jun 2016
Estimated size (number of pages)	120
Elsevier VAT number	GB 494 6272 12
Requestor Location	Danial Barati 301 main st, 2C02 COLUMBIA, SC 29208 United States Attn: Danial Barati